Tomographic observations of deep convection and the thermal evolution of the Greenland Sea Gyre 1988-1989

by

Ryszard A. Pawlowicz

B. Sc., Queen's University, Canada
(1987)

Submitted in partial fulfillment
of the requirements for the degree of

Doctor of Philosophy

at the

MASSACHUSETTS INSTITUTE OF TECHNOLOGY

and the

WOODS HOLE OCEANOGRAPHIC INSTITUTION

February 1994

Author .....
MIT-WHOI Joint Program in Oceanographic Engineering
January 7, 1994

Certified by .....
James F. Lynch
Associate Scientist
Thesis Supervisor

Certified by .....
W. Brechner Owens
Senior Scientist
Thesis Supervisor

Accepted by .....
Arthur Baggeroer
Chairman, Joint Committee of Applied Ocean Science and Engineering

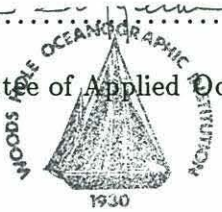

Tomographic observations of deep convection and the thermal evolution of the Greenland Sea Gyre 1988-1989

Ryszard A. Pawlowicz

Shortened abstract for NTIS

Abstract

The Greenland Sea Gyre is studied using results from the 1988-89 Greenland Sea Tomography Experiment. Thermal evolution of the gyre center divides into three periods: a preconditioning phase, a deep mixing phase, and a restratification phase. During preconditioning, ice forms and rejects brine into the surface waters, enabling destabilization of the water column. The onset of the deep mixing phase occurs after ice formation in the gyre center stops, resulting in an area of open water where large heat fluxes can occur. In surrounding regions, including the odden region to the south, ice is still being formed, and the mixed layer does not deepen significantly. The effects of advection are deduced from heat and salt budgets, and appear to be important only during the restratification phase for intermediate depths, and only during the summer for the surface waters. Dynamical processes for bringing the Arctic Intermediate Water (AIW) to the surface in order to form deep water are not needed in this scenario, rather the surface waters are modified until they match the density of the AIW after which surface cooling drives convection.

Tomographic observations of deep convection and the thermal evolution of the Greenland Sea Gyre 1988-1989

by

Ryszard A. Pawlowicz

Submitted in partial fulfillment of the
requirements for the degree of
Doctor of Philosophy
at the
MASSACHUSETTS INSTITUTE OF TECHNOLOGY
and the
WOODS HOLE OCEANOGRAPHIC INSTITUTION
February 1994

Abstract

The thermal evolution of the Greenland Sea Gyre is investigated using both historical data and tomographic results from the 1988-89 Greenland Sea Tomography Experiment. Thermal evolution of the gyre center divides naturally into three periods: a preconditioning phase (November-January), during which surface salinity is increased by brine rejection from ice formation and by entrainment but in which the mixed-layer deepens only slowly to a depth of some 150-200m, a deep mixing phase (February-March) during which the surface mixed-layer deepens rapidly to approximately 1500m in the gyre center purely under the influence of local surface cooling, and a restratification phase during which the products of deep mixing are replaced by inflowing Arctic Intermediate Water (AIW). The onset of the deep mixing phase occurs after ice formation in the gyre center stops, resulting in an area of open water where large heat fluxes can occur. In surrounding regions, including the odden region to the south, ice is still being formed, and the mixed layer does not deepen significantly. To the north and west, closer to the steep topography of the continental shelf, the inverse results show significant variability due to advection, and large temperature and heat content fluctuations with a period of about 50 days are seen. The effects of advection are deduced from heat and salt budgets, and appear to be important only during the restratification phase for intermediate depths, and only during the summer for the surface waters. Comparison of the tomographic results with point measurements indicates that deep mixing occurs in a field of small plumes in which dense water sinks downwards, surrounded by larger regions of upwelling. The plume geometry is consistent with that predicted by numerical and laboratory models. Dynamical processes for bringing the AIW to the surface in order to form deep water are not needed in this scenario, rather the surface waters are modified until they match the density of the AIW after which surface cooling drives convection.

Thesis Supervisor: James F. Lynch (Associate Scientist)

Thesis Supervisor: W. Brechner Owens (Senior Scientist)

Acknowledgements

Hmmm. At this point, it is considered polite for the author (me) to profusely thank a long, long list of people who either a) did essential work without which I wouldn't have had a thesis (the technical staff), b) will provide references letters for me (my thesis committee), and c) put up with my smartass remarks and "provided moral support" (friends and family). And of course I have to make the usual (but true) remarks about how lucky I was and am, etc. etc., plus some gratuitous remarks about my athletic achievements just to show that I'm not shallow. So here goes.

I'd first like to thank a number of people (some of whom I unfortunately never met), without whom the Greenland Sea Tomography Experiment would not have worked as well as it did. These include S. Abbott, J. Bouthillette, P. Boutin, K. Hardy, D. Horwitt, J. Kemp, S. "Fuzzy" Liberatore, D. Peckham, and R. Truesdale. Art Newhall introduced me to Unix and never once called in sick to avoid seeing me. I'd also like to thank my co-advisors, Breck Owens for checking my oceanography and saying *hmmmm* doubtfully and *especially* Jim Lynch for letting me wander into interesting regions and letting me do far far too much of what I wanted instead of what I was paid to do. Interesting and relaxing discussions on acoustics and oceanography with D.J. Tang, Jin Guoliang, and Tim Duda kept me from overloading on the Greenland Sea. And when I needed to relax more, I could always make the Long Drive North to sleep in a nice house or beside a beautiful lake, even if it wasn't a hotel (that's a joke, Dad).

Finally, I'm not sure I would have survived without my friends, especially those with whom I could release aggression through bike racing. To the MIT Geezers now scattered far and wide, as well as the Ta-ster, my thanks for keeping those weekends and roadtrips to exotic industrial parks fun and not stealing my tools.

Final (but still grateful) mentions go to MIT, WHOI, and the Office of Naval Research for letting me study in Cambridge and Woods Hole, and (most especially) for paying me to do so.

Rich "can I quit now?" Pawlowicz
Woods Hole, MA.,
7/Feb/1994.

Contents

List of Figures

Chapter 1

Introduction

1.1 Motivation

The Nordic Seas (including the Greenland, Iceland, and Norwegian Seas) have always been an area of interest to oceanographers. In recent years it has been recognized that this region is a gateway between the Arctic Ocean and the Atlantic Ocean, in fact the only significant channel by which an exchange of water and heat can occur. The Fram Strait, at a depth of 2600m, is 10 times deeper than the next deepest passage, and the annual southward export of ice through this passage is some two orders of magnitude greater than that which passes north through the Bering Straits [*Aagaard and Carmack*, 1989].

It has also long been recognized that the Greenland Sea is different from the Norwegian and Icelandic Seas in that the deep water there is replenished from the near-surface waters. This deep water, the coldest and freshest deep water north of the sill joining Greenland, Iceland, and Scotland, then flows into the surrounding seas. As the accuracy with which water masses can be classified increases, "plumbing diagrams" of the thermohaline circulation have become more complex. Early attempts at classifying water types into a few different classes have become more and more sophisticated as the observational database becomes more comprehensive (for example, the 4 water masses described by *Coachman and Aagaard* [1974] are subdivided into 8 by [*Johannessen*, 1986] and 27 (!) by *Hopkins* [1991]). Above the deep water lies a layer of so-called Arctic Intermediate Water (AIW) which overflows via the Denmark Strait and the Faeroe Bank Channel into the North Atlantic, forming the North Atlantic Deep Water which can be traced into the South Atlantic, Indian, and finally the Pacific Oceans as part of the great thermohaline conveyor [*Broecker*, 1991].

But the process by which the Greenland Sea Deep Water (GSDW) is formed has always been a mystery, since the observed surface waters in the fall are usually too fresh (light) to sink even when cooled to the freezing point. During the 1980s, a number of large field programs were undertaken to better understand this and other problems in this region. As part of the Greenland Sea Project, a multi-year program involving many nations [*GSP Group*, 1990], a tomographic array was moored in the Greenland Sea over the 1988-89 winter. This was one of the first tomographic experiments designed primarily to increase understanding of the ocean (the other being the Gulf Stream Extension Experiment which took place at the same time), rather than an engineering test of equipment and procedure in a purposely chosen quiet and fairly well-understood part of the ocean. Somewhat ironically, much of the previous experience with tomography, both experimental and theoretical, was to some extent irrelevant to this deployment in the arctic environment where the governing processes of ocean dynamics and acoustic propagation were quite different from those previously experienced.

The Greenland Sea Tomography Experiment was designed with two major oceanographic objectives: to better understand deep convection, and to learn more about the dynamics in the Greenland Sea. In this thesis we shall be concerned primarily with the temperature field. It was also assumed that the analysis would provide a better understanding of acoustic propagation in high-latitudes, and indeed a number of interesting acoustic features have been discovered, some of which are discussed here.

1.2 Thesis Outline

This thesis represents a fusion of purely oceanographic and purely acoustic analyses. Each of the early chapters (2-6) are generally focused on a single aspect of the analysis, and are somewhat independent of one another. The final chapters (7-8) bring together all of the information. In particular, the material is arranged as follows: Chapter 2 will briefly describe the hydrography of this region, summarizing previous work relevant to this thesis. Particular emphasis will be placed on observations and theoretical ideas concerning the mechanisms of deep convection. Some of the difficulty in understanding the governing processes is due to an inadequate knowledge of the seasonal cycles of temperature and salinity in this region, and so in chapter 3 historical data is analyzed to determine a monthly

climatology. As well as being of interest for its own sake, this climatology also forms the basis for later comparisons with the more detailed observations available from the Greenland Sea Tomography Experiment. Chapter 4 describes the tomography experiment itself, and the observed characteristics of acoustic propagation, some aspects of which are novel. Chapter 5 details the procedure used to produce and validate inverses for range-average temperature profiles and heat content along all paths in the tomography array. In Chapter 6, we consider the errors and uncertainties in surface flux estimates obtained from the United Kingdom Meteorological Office, and in sea ice concentration estimates derived from satellite passive microwave measurements. The flux estimates in particular are highly sensitive to details of the ice cover, and as originally obtained were inadequate for our purposes. Chapter 7 combines the various observations to describe the thermal evolution of the Greenland Sea Gyre and to identify the large-scale mechanisms involved in deep convection. Finally, we draw some conclusions from this work relevant to future investigations of deep convection, and future tomographic experiments in the Arctic.

Chapter 2

Historical Background

In this chapter we will briefly describe the hydrography of the Greenland Sea and the currently accepted view of the thermohaline circulation in this region. We then focus on deep convection, presenting a historical perspective of the research in this area, before finishing with an outline of recent numerical and laboratory experiments that have some relevance to our analysis. References to the literature are by no means exhaustive, but should provide a good starting point for further inquiries. Nomenclature in this region is sometimes confusing; where alternative names exist the definitions in *Hurdle* [1986] are used.

2.1 Major Features and Surface Circulation

The Greenland Sea is one of the so-called "Nordic" Seas (also referred to somewhat inelegantly by the acronym "GIN" Seas referring to the Greenland, Icelandic , and Norwegian Seas) that form a channel between the North Atlantic and the Arctic Oceans (see figure 2-1). This region is divided into a number of basins up to 4000m deep, separated by sills of approximately 2500m in depth, and bounded to the south by the shallow Denmark Strait and Faeroes Bank Channel spanning the Greenland - Iceland - Scotland gap (no deeper than 1200m) and to the north by the Fram Strait (depth 2600m) which provides the only deep-water passage to the Arctic Ocean, being about 10 times deeper than the next deepest passage. To the west lies Greenland, and to the east are Norway, Svalbard, and the shallow waters of the Barents Sea.

In describing the surface circulation, one finds that available numerical estimates of the

transport span a wide range, and it is unclear to what extent these numbers are affected by assumptions made in the calculations and to what extent they reflect seasonal and interannual variability. The values quoted here are taken from the review by *Hopkins* [1991]. The surface circulation is dominated on the eastern side by the northward flow of the warm, saline Norwegian Atlantic Current (with estimated transports of order 3-8 Sv[1]) and the West Spitzbergen current (with a transport of a similar magnitude), and on the western side by the southward flow of the colder, fresher, buoyancy-driven East Greenland Current (EGC) along the wide continental shelf (see figure 2-2). The Fram Strait is the major passage through which ice is exported from the Arctic, and the EGC carries on the order of 0.1 Sv of ice (3000 km^3/yr) as well as roughly balancing the northward transport of the West Spitzbergen Current. South of the Fram Strait part of the West Spitzbergen Current turns west and south. In this recirculation warm saline surface waters of Atlantic origin are converted into southward flowing Arctic Intermediate Waters (AIW) which lie below the surface. North of Jan Mayen Island an eastward protruberence of the EGC called the Jan Mayen Current apparently completes the cyclonic circulation pattern in the Greenland Sea called the Greenland Sea Gyre. The Jan Mayen Current is a partly a meander of the EGC - the surface flow tends to turn south and westwards, returning to the EGC, while only the deeper flow continues eastwards [*Bourke et al.*, 1992].

The confluence of these currents with differing temperatures and salinities results in the formation of a number of fronts, the most important of which (for the purposes of this thesis) are the Polar Ocean Front which extends north-eastwards from Jan Mayen along the Mohns Ridge, and the East Greenland Front which follows the edge of the continental shelf. These fronts separate the Greenland Sea Gyre from neighbouring regions, and apparently impede the exchange of water between the EGC and the gyre. *Aagaard and Carmack* [1989] estimate that only about 3% of the fresh water transport of the EGC enters the gyre, and *Foldvik et al.* [1988] found that cross-front turbulent fluxes were insignificant at 79°N.

The gyre's cyclonic circulation implies an upward doming of isopycnals in the center of the gyre, weakening the background stratification and making deep convection more likely. However, the reason for the existence of this gyre is unknown. Although *Aagaard* [1970] (and more recently *Jónsson* [1991]) found that a flat-bottom Sverdrup balance driven by the annual mean wind stress curl in the Nordic Seas would result in a gyre of approximately the

[1] 1 Sv or Sverdrup is 10^6 m^3/sec

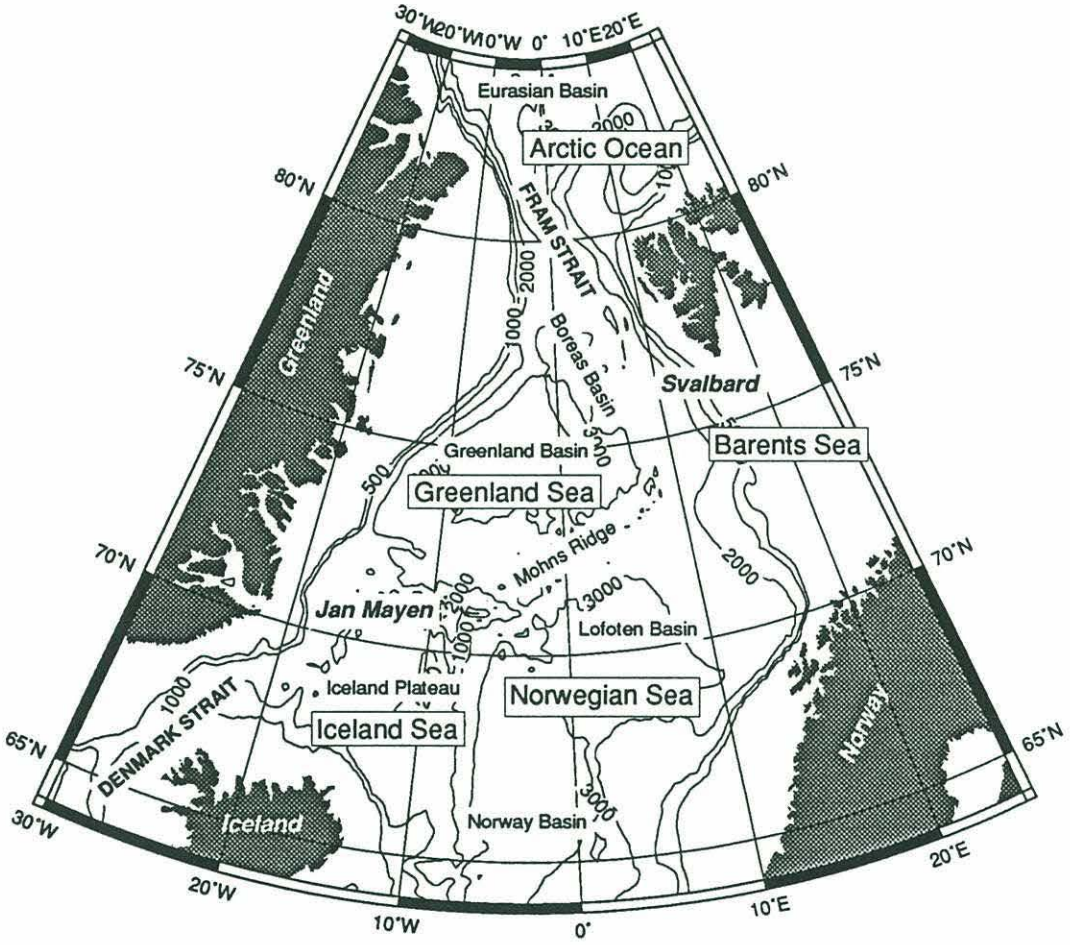

Figure 2-1: Major Geographic Features in the Nordic Seas

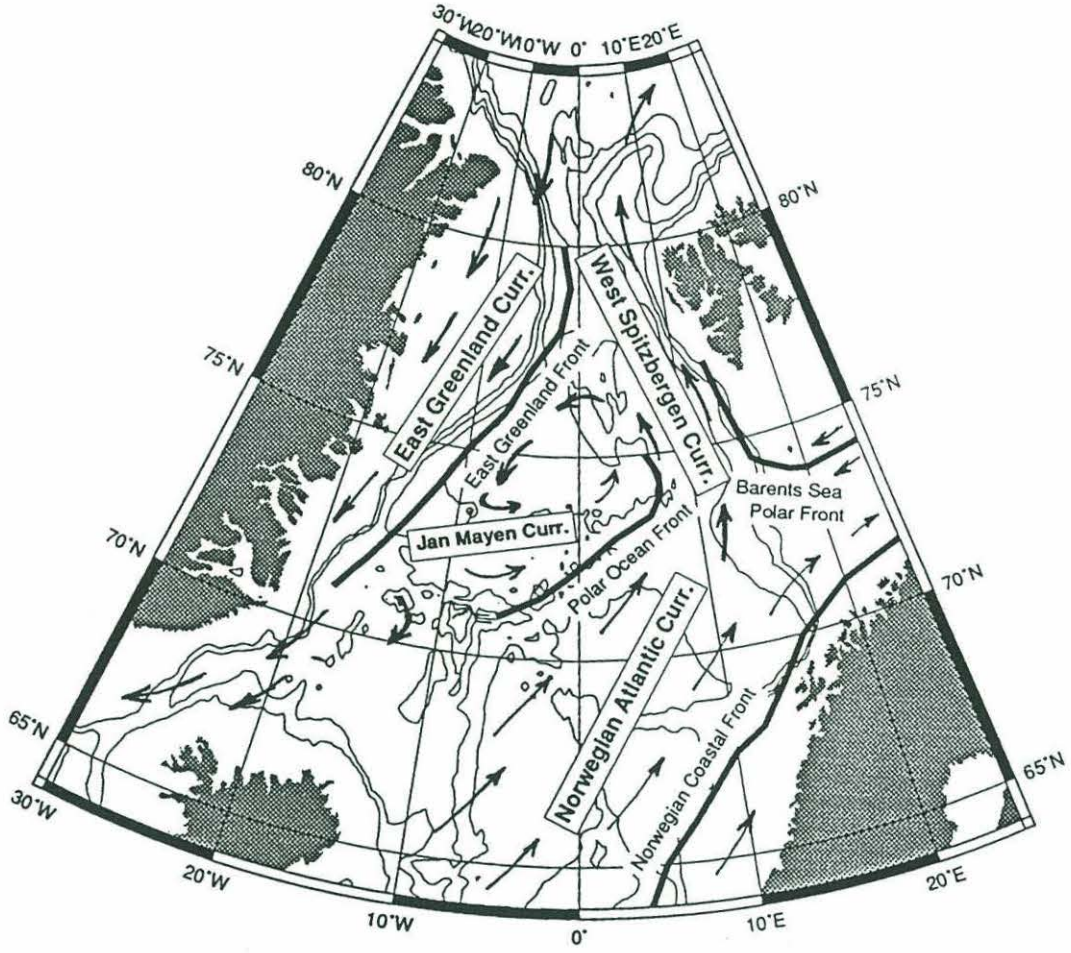

Figure 2-2: Major Circulation Features in the Nordic Seas

correct magnitude and location, the weak stratification and large bathymetric variations in the Nordic Seas would seem to invalidate the assumptions behind such a balance except at time scales of greater than several decades - the time scale for the propagation of long non-dispersive baroclinic Rossby waves across the basin, which compensate for the bathymetric effects in generating a flat-bottom balance in a stratified ocean with bathymetry [*Anderson and Killworth*, 1977]. It is not clear that the forcing (or indeed that deep convection) is steady over those time periods. A recent numerical model [*Legutke*, 1991] initialized with a smoothed climatological temperature and salinity field and forced by climatological winds did produce a gyre, but the 2-year spin-up may not have been long enough to result in a completely wind-driven circulation. The circulation patterns in this model largely consisted of surface-intensified barotropic flows, which would certainly be greatly affected by topography. Isolines of constant ambient potential vorticity (f/H contours), the preferred paths for barotropic flow, are closed in the Greenland Sea implying that the lowest order dynamical balance is between wind stress curl forcing and bottom friction (i.e. *along* isoline flow), rather than between wind stress curl and cross-isoline flow as found in the Sverdrup balance [*Pedlosky*, 1987]. In this regard *Meincke et al.* [1992] found that mean wind stress curl over the Greenland Sea was low during the late 1970s and 1980s, roughly coincident with a period of little or no deep water renewal. They proposed that the decreased curl implied a weaker cyclonic circulation via the flat-bottom Sverdrup balance, hence less doming of isopycnals and less predisposition to deep convection. There are, however, other mechanisms by which wind stress curl and convective depth could be related.

Another possibility is that the gyre is driven by deep water formation (DWF). It is well known that the conversion of upper layer water to lower layer water in a 2-layer ocean can drive a cyclonic surface circulation [*Gill et al.*, 1979; *Crépon et al.*, 1989] as the surface water which flows inwards to replace the sinking converted water is affected by the coriolis force. Although the extent of this cyclonic circulation scales with the baroclinic deformation radius in the steady state, the intermittency of the forcing will drive baroclinic rossby waves which can spread the effect throughout the basin [*Barnier et al.*, 1989; *McDonald*, 1992]. Thus one might hypothesize a kind of flywheel effect in which annual deep water formation events force a cyclonic circulation which disperses on the time scales of long non-dispersive baroclinic waves and hence lasts until the next season.

It may also be the case that the gyre circulation is simply a result of the interaction

between the northward-flowing Atlantic Water, the southward flowing Arctic Water, and the particular bathymetry of the region, or indeed some combination of all three factors.

The Greenland Sea is located in a Marginal Ice Zone (MIZ). During the summer, ice extent is limited to the continental shelf, but during the winter the ice edge can extend far to the east, covering most of the gyre. In many but not all years, a large tongue of ice (called the "odden") roughly coincident with the Jan Mayen Current lies to the south of a bay in the ice ("nordbukta") which forms over the gyre center and the region of DWF. This feature has been well-known to whalers as far back as the 17th century [*Wadhams*, 1986; *Sanger*, 1991], but the reason for its existence is unknown (a theory explaining this feature will be discussed in this thesis). The exact location and extent of the ice edge can vary enormously from year to year [*Vinje*, 1977; *Walsh and Johnson*, 1979]. Some particularly prominent examples of the odden are shown in figure 2-3.

2.2 Deep Circulation

Although the patterns of the surface circulation appear to be fairly well-known, the same can not be said for the deep circulation. In particular, the sequence through which the various deep waters are transformed into one another is still an active area of investigation.

The Greenland Sea Deep Water (GSDW) seems to be the youngest of the deep waters, as well as the coldest, freshest, and (in terms of σ_3) the densest. The center of the Greenland Sea gyre has long been known to be a region of DWF. Figure 2-4 shows a north-south transect through the Norwegian and Greenland Seas and the Arctic Ocean. Isopleths of all variables are mostly level in the Norwegian Sea. A slight salinity minimum near 500m is associated with the Arctic Intermediate Water. Isopleths are also mostly level in the Arctic Ocean itself (although data quality and availability is lower there). However, in the Greenland Sea all variables indicate some connection with the surface. It is this feature, as well as the extremal temperature and salinity characteristics of the GSDW, that has traditionally been cited as evidence for deep water formation in this basin. The Canadian Basin Deep Water (CBDW) is the warmest and most saline, as well as the lightest of the deep waters. It is apparently formed from shelf waters which are enriched by brine rejection during ice formation [*Aagaard et al.*, 1981].

Between the Canadian Basin and the Greenland Basin lies the Eurasian basin. Eurasian

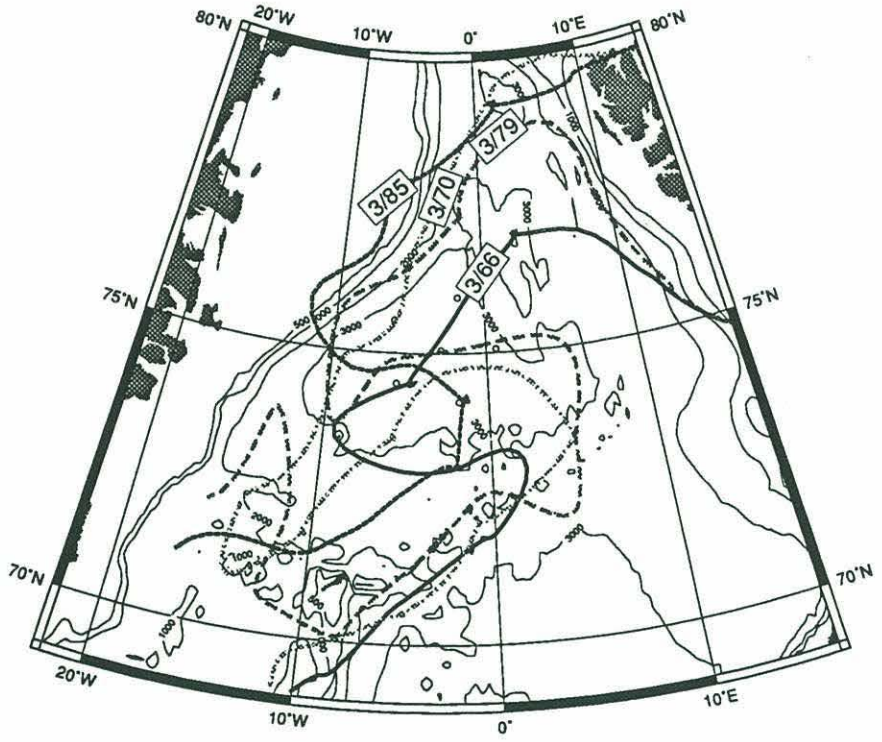

Figure 2-3: Some examples of pronounced odden events from the Walsh Ice climatology (see chapter 3). The ice edge is denoted by the 40% concentration contour

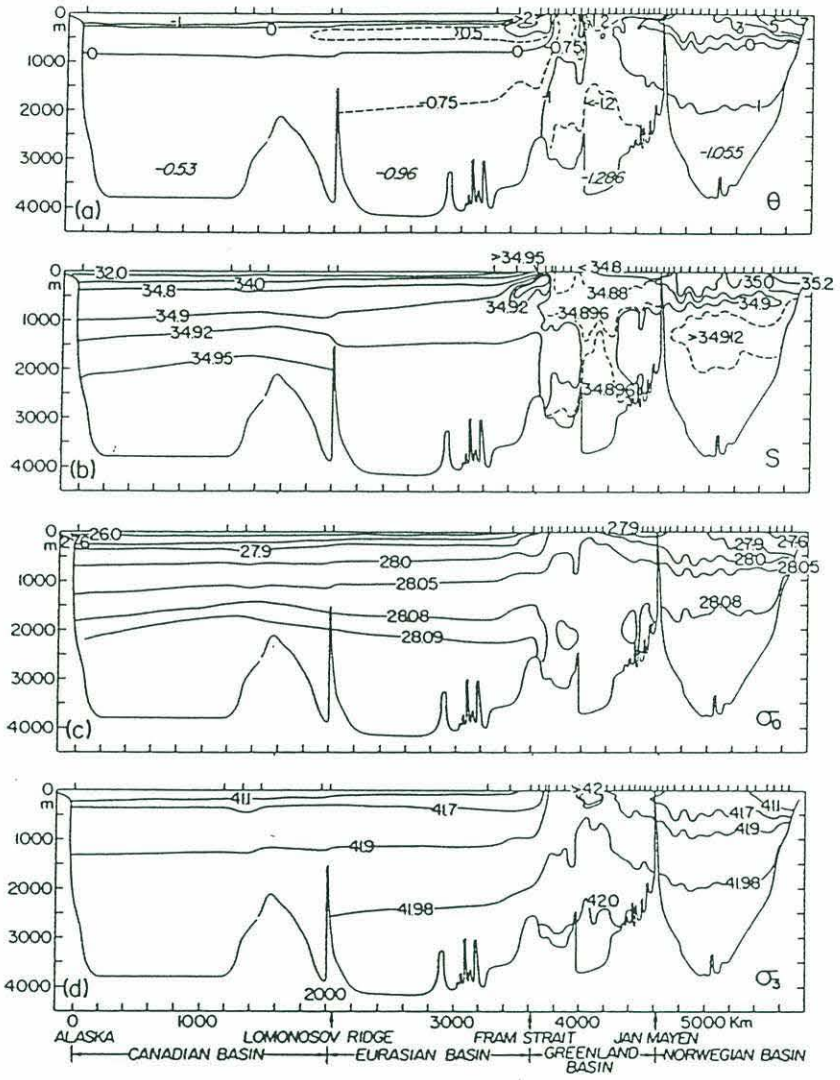

Figure 2-4: Water properties on a transect across the Arctic (from *Aagaard et al.* [1985], from the Canadian side (at left) throught the Fram Strait (center) to the Norwegian Sea (right).

Basin Deep Water (EBDW) is thought to result from the mixing of GSDW and CBDW. Norwegian Sea Deep Water (NSDW) is presumed to form around the periphery of the Greenland Sea as a mixture of GSDW and Arctic Ocean Deep Water (AODW), which is a modified version of the EBDW [*Aagaard et al.*, 1985]. The newly formed NSDW flows into the Norwegian Sea over the Mohns Ridge east of Jan Mayen (see the discussion in *Bourke et al.* [1993]).

The overflow over the Greenland-Iceland-Scotland Ridge that forms the North Atlantic Deep Water (NADW) is mostly composed of AIW, although some NSDW is apparently entrained in the outflow through the deeper Faeroe Bank Channel [*Aagaard et al.*, 1985].

2.3 Theory and Observations of Deep Convection

In order to fully understand the deep circulation in the Arctic, we must understand how the GSDW is formed. Figure 2-4 shows that the potential density (σ_θ) of the surface water is not great enough to allow sinking to the bottom. The GSDW is the lightest of the deep waters when density is referenced to the surface, but when referenced to 3000m (i.e. when considering σ_3) the GSDW is seen to be the densest deep water. Near-surface water *is* dense enough in σ_3 to replace bottom waters, but there seems no obvious method for it to traverse the "mid-depth barrier". Thus DWF in the Greenland Sea is apparently quite different from that observed in the Mediterranean, in which surface cooling is enough to drive convection to the bottom [*MEDOC Group*, 1970].

This has always been the puzzle: surface water is too light to replace the deep water, but the recirculated Atlantic Water (which appears as the AIW at depths of 200-800m in the gyre) which *could* replace the deep water if cooled does not appear to come to the surface, and hence cannot be cooled!

Attempts to better understand DWF have been hampered by the difficulties involved in working in the MIZ in winter, and until recently little more was known about the hydrography of this region than typical summer and winter profiles. Most descriptions were based on the first comprehensive surveys of this region made during the International Geophysical year [*Dietrich*, 1969]; however as will be shown in the next chapter observations from that program seem to be somewhat anomalous.

One of the earliest theories of DWF was that of *Metcalf* [1955], who hypothesized sinking

along tilted isopycnals based on a number of observations that seemed to show surface densities (i.e. at 0m) much greater than those of the first subsurface sample (usually at about 50m) but with no evidence of vertical homogeneity. The surface values were taken from bucket samples and their accuracy was questioned by *Carmack and Aagaard* [1973] who proposed instead a mechanism (later elaborated upon by *McDougall* [1983]) in which inflowing AIW was slowly transformed into GSDW by a double-diffusive process at the interface between the AIW and the surface water. In this scenario, large convection cells in the surface waters transport heat to the surface, while little salinity exchange occurs. By comparing a census of summer and winter water masses using the IGY stations, they estimated that about 30×10^3 km^3 of deep water was formed annually.

In 1972 tritium and radiocarbon profiles were measured at stations in the center of the major basins as part of GEOSECS. Analyzing this data using a box-model with 3 elements, *Peterson and Rooth* [1976] estimated that renewal times for the GSDW were about 30 years, implying that about 100m of the surface water were converted to bottom water each year. They also concluded that the source of North Atlantic Deep Water was probably the AIW, and that the deep waters were essentially isolated from mid-latitude oceans. A similar renewal time was found by *Bullister and Weiss* [1983] using 1982 observations of anthropogenic chlorofluorocarbons (CFCs).

The discovery of a narrow chimney in the Weddell Sea in February 1977 gave rise to a new theory of open ocean convection in which deep water is formed inside baroclinic eddies [*Killworth*, 1979]. The cyclonic surface rotation of these eddies will precondition the water column by bringing the intermediate water to the surface, where it can be cooled. Some simple arguments were advanced which implied that such chimneys would be rather rare, and that because of the somewhat sparse observational database it was extremely unlikely that any such chimneys would have been observed in the Greenland Sea. However, during 1989, a 20 km wide chimney containing deep water *was* observed in the Boreas Basin near 78°N, somewhat to the north of the central Greenland Sea and not far from the ice edge [*Johannessen et al.*, 1991].

So far little attention had been paid to the possible dynamical and thermodynamical role of ice in this process. It is well-known that the bulk drag coefficient over ice can be double that over the open ocean [*Fairall and Markson*, 1987; *Anderson*, 1987; *Guest and Davidson*, 1987]. Thus winds along the ice-edge can cause an Ekman divergence, leading to

upwelling of subsurface waters. This subsurface water could then cool and sink, replacing the deep water [*Häkkinen et al.*, 1992].

On the other hand, the formation of ice results in the rejection of brine into the underlying water, increasing its salinity. *Clarke et al.* [1990] coupled a simple 1D mixed-layer model with non-penetrative convection forced by surface heat and salt fluxes to a thermodynamic ice model to determine the possible evolution of various profiles measured in March of 1982. They found that deep convection would be accelerated in a process whereby cooling would result in the formation of ice and consequent rejection of brine into surface waters which could then mix downwards, bringing up warmer water which would then melt the ice. Removal of the ice by surface winds resulting in a net increase in salinity would further enhance this process. However, the winter of 1981-82 was not long or cold enough for convection to the bottom to occur in this way. *Rudels* [1990] considered the formation of dense convective plumes through freezing processes.

These two ideas can be combined: winds at 0° to 45° relative to an ice edge on their right will sweep newly-formed ice into a compact ice-edge, keeping clear an area where air-sea temperature differences are particularly large so that heat fluxes are particularly strong [*Guest and Davidson*, 1991]. Winds in this direction will also result in ice edge upwelling.

However, the vertically homogeneous mixed-layer that should result from these processes has never been observed near the center of the Greenland Sea, although indirect evidence for the conversion of surface waters can be found in figure 2-5 (adapted from *Livingston et al.* [1985]), which shows the surface concentrations of radioactive Cesium in 1981-1982. Although fallout from atmospheric nuclear testing in the late 1950s and early 1960s had introduced ^{137}Cs into the surface waters, by the 1970s this source had become small, and the sudden increase in ^{137}Cs concentrations found in the West Spitzbergen Current in 1979 was due to its introduction into the Irish Sea by low-level radioactive wastes from the British Nuclear Fuels Ltd. reprocessing plant in Sellafield, Great Britain. One can clearly identify plumes associated with the major currents shown in figure 2-2, as well as a small region of quite low concentrations (lower than the background levels found in the Arctic and almost as low as the mid-latitude oceanic background level) in the center of the Greenland Sea. This lower level is consistent with a homogenization of the water column (i.e. mixing with the deeper and uncontaminated waters below) sometime in the previous few years. Although interpretation is complicated by the possibility that the tracer-marked waters flow mostly

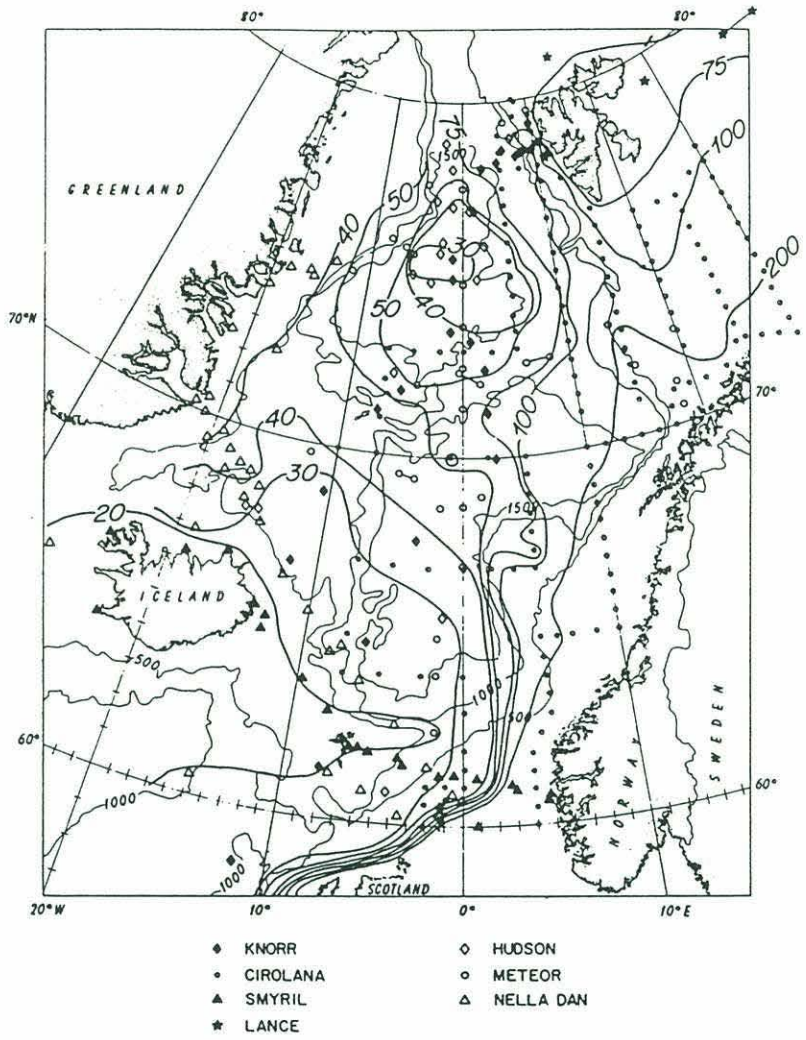

Figure 2-5: Surface Distribution of ^{137}Cs in 1981-82 (adapted from *Livingston et al.* [1985]). Filled symbols are observations from July-August 1981. Open symbols are from observations made in March-August 1982.

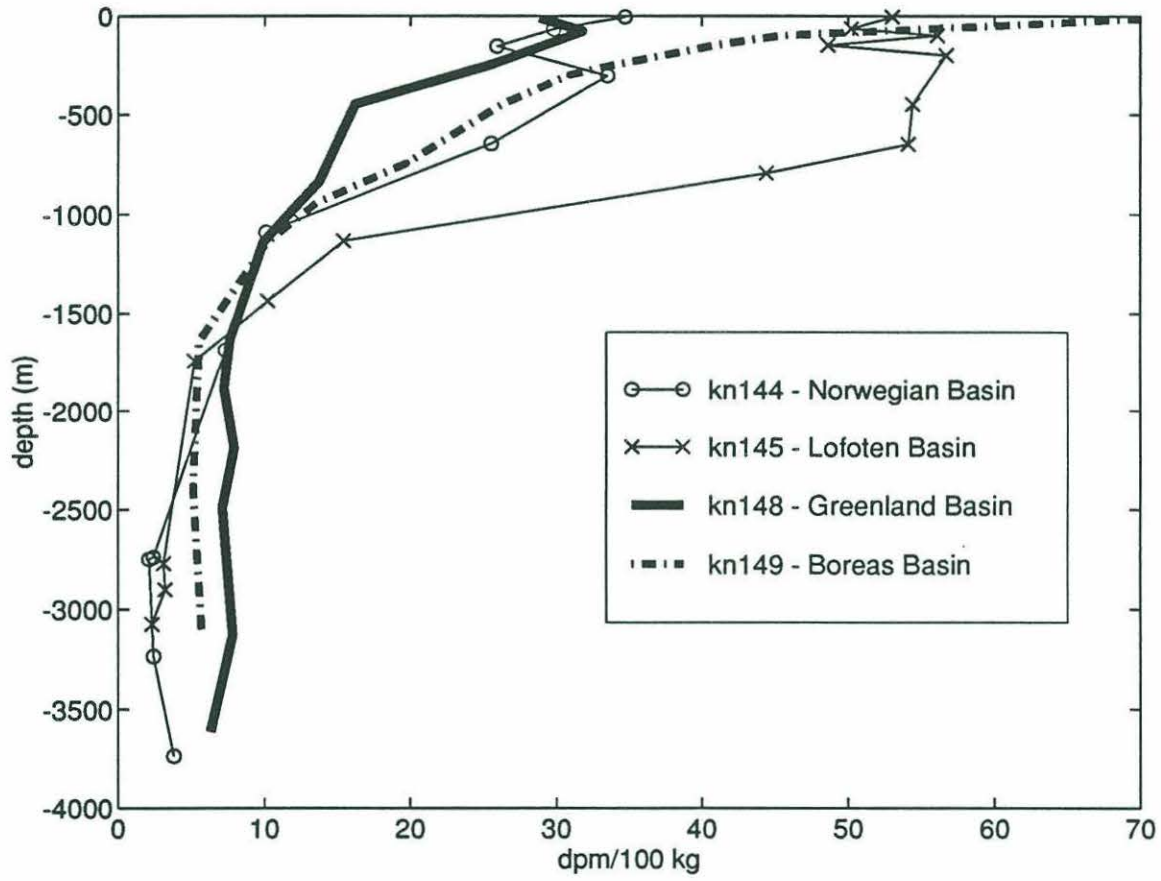

Figure 2-6: Vertical distribution of ^{137}Cs in the various basins of the Nordic Seas in July 1981. Levels in the NSDW are about half those seen in the GSDW. The Greenland Sea has the most vertically homogeneous profile, although the total amount of ^{137}Cs in the water column is less than in all other basins (adapted from *Casso and Livingston* [1984]).

in the boundary currents and do not enter the gyre, profiles from July 1981 show that the Greenland Sea is more vertically homogeneous than surrounding waters and that the GSDW has far greater amounts of ^{137}Cs than the deep waters in other basins (figure 2-6).

Part of the problem in understanding DWF from the relatively sparse database may be that replacement of the deep water is not an annual occurrence. A long time series of deep temperatures from a weather station in the Labrador Sea analyzed by *Lazier* [1980] shows that intermittent periods of DWF there are associated with step changes in the temperature of the deep water. The temperature changes of GSDW are known much less well, but apparently vary over decadal time scales [*Aagaard*, 1968]. Although this change may be related to intermittency of convection, other factors may also be important (see also figure 3-2a and section 8.1). Observations of anthropogenic tracers have become common in recent years, and analysis of this data using box models indicates that DWF has not occurred after about 1982, although it must have occurred in the previous decade (e.g., *Schlosser et al.* [1991], *Rhein* [1991] and references therein). Thus oceanographers in the 1980s have been placed in the peculiar position of attempting to identify a process which has not been occurring!

As it happens, wintertime convective activity in the Greenland Sea over the period 1986-1990 reached depths of 200m, 1350m, 1600m [*GSP Group*, 1990], and 250m [*Budéus et al.*, 1993], so that the tomographic observations made during 1988-1989 are more helpful in our quest than we perhaps deserve.

2.4 Numerical Studies of Deep Convection

In parallel with the observational effort a number of theoretical and numerical studies of deep convection have been pursued. Early studies externally specified the convection process in some way, e.g. *Gill et al.* [1979], *Crépon et al.* [1989], *McDonald* [1992] and references therein, or concentrated on the adjustment problem, studying the methods by which a homogenous chimney would come to equilibrium after the surface forcing was removed [*Hermann and Owens*, 1991]. In general these studies found that packets of waves would be radiated by the collapsing chimney; first gravity waves, then barotropic Rossby waves, and finally baroclinic Rossby waves, setting up a large-scale cyclonic circulation in the upper waters (and an anticyclonic circulation below). In more non-linear regimes an instability at

the edges of the chimney would result in its rapid breakup into a number of eddies, elegantly studied using finite clumps of point vortices (so-called "hetons") [*Hogg and Stommel*, 1985; *Legg and Marshall*, 1993] and a continuous version thereof [*Pedlosky*, 1985].

Recently it has proved possible to run non-hydrostatic models with a very fine horizontal and vertical resolution, removing the need to parametrize the deep convection itself [*Brugge et al.*, 1991]. Currently most work has been done in neutral oceans. A surface buoyancy flux B_o results in the formation of small plumes of diameter l in which dense water sinks rapidly downwards with scale velocity u, surrounded by somewhat larger regions of upwelling. The width and velocity of plumes in a rotating ocean with Coriolis parameter f scale as [*Jones and Marshall*, 1993]:

$$l \sim \left(\frac{B_o}{f^3}\right)^{1/2} \tag{2.1}$$

$$u \sim \left(\frac{B_o}{f}\right)^{1/2} \tag{2.2}$$

These scales correspond fairly well with estimates made by thermistors and moored ADCPs in the Greenland Sea during 1988-89 [*Schott et al.*, 1993]. Collectively the plumes or convection cells which are separated horizontally by a distance L act to homogenize the region of convection to a depth D, forming a chimney. The chimney scale will be set by the initial preconditioning or by the scale of the buoyancy forcing. Little fluid exchange occurs through the sides of the chimney, since horizontal motions will be inhibited by rotation, and horizontal convergences and divergences will result in strong geostrophic currents around the chimney. Geostrophic forces will also limit the distance between plumes, i.e. the horizontal scale of individual convection cells, such that [*Boubnov and Golitsyn*, 1986; *Klinger and Marshall*, 1993]

$$\frac{L}{D} \sim 0.1 - 1 \tag{2.3}$$

The vertical convection cells act to homogenize the water in a chimney within a few days, after which the chimney can break up as above.

Chapter 3

Seasonal Climatology of Temperature and Salinity

3.1 Introduction

As was discussed in the previous chapter, the major difficulty in understanding deep water formation (DWF) in the Greenland Sea lies in the lack of observations of deep, vertically homogeneous regions consistent with ideas of large-scale overturn. In turn this may be due to the apparent freshness of the surface waters. There is also the heretofore ignored "odden" feature which may be linked to DWF.

In order to understand the reasons for the formation of the odden and of the possible role of ice in the deep convection process a better description of the seasonal cycle of surface temperature and salinity is necessary. Here we attempt to delineate the characteristics of this cycle by analyzing historical data in two different regions of the Greenland Sea (see figure 3-1). The first region (6°W–0° long., 74°N–76°N lat.), hereafter called the "mid-gyre" region, coincides with the gyre center, a region of deep mixing, and the location of the Greenland Sea Tomography Experiment. This area is characterized by a fairly weak stratification below the mixed layer at all times. The second region (6°W–0° long., 72°N–74°N lat.) is directly to the south in the area covered by the odden tongue (and will be referred to as the "odden" region). Although extending the southern boundary to 71°N would almost double the available data, many of the extra observations lie close to the Polar Ocean Front and are unrepresentative of the odden region. A similar effect limits the

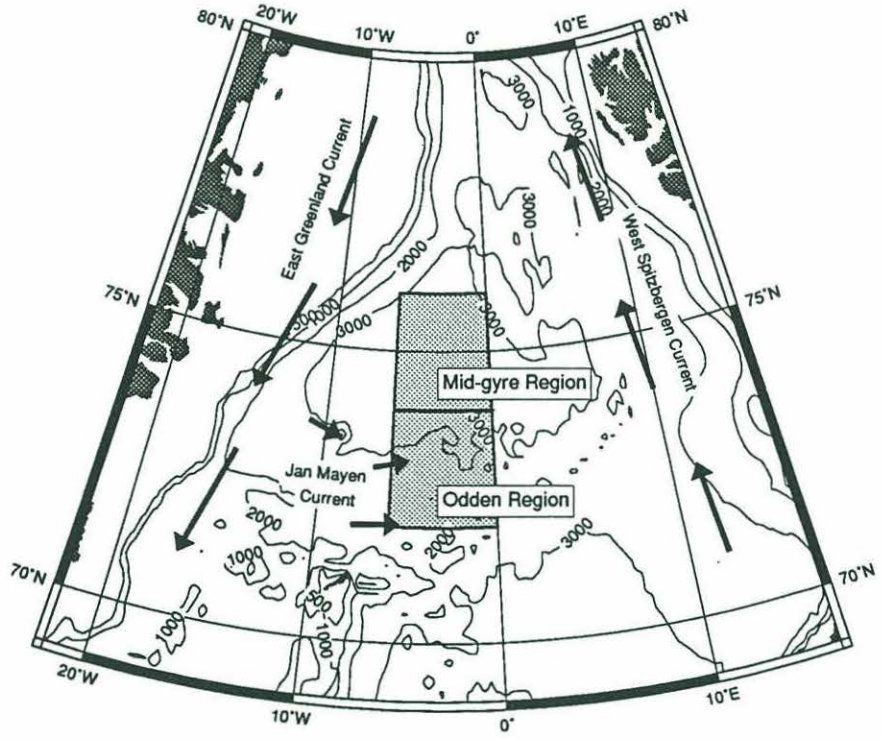

Figure 3-1: Historical data is binned in the two shaded squares in the Greenland Sea

northern extent of the mid-gyre region. Longitudinal boundaries roughly bracket the gyre center, but the eastern limit of 0° is also close to the eastern edge of the odden. Moving the western limit (6°W) further west would result in little additional data, and could include the waters of the East Greenland Current on the other side of the East Greenland Front.

In section 3.2 of this chapter, a brief description is given of the data sources and quality. Section 3.3 describes the procedures used to form a monthly climatology. In section 3.4 an analysis of the resulting time series is carried out. Finally we discuss some implications of this cycle for understanding DWF and the odden event.

3.2 Sources of Data

A search was made for standard hydrographic data from the Greenland Sea. Only bottle casts and CTD stations were considered, although a large number of shallow bathythermograph (BT) casts of variable quality were also available. Temperature and salinity profiles were obtained from the following sources (the number of stations in the odden/mid-gyre regions are noted in parentheses):

1. **NODC Archives (96/93)** Bottle casts distributed roughly uniformly between 1950 and 1985 with one station in July of 1906. By far the greatest number of stations were occupied in June. International Geophysical Year (IGY) Polar Ocean Survey stations [*Dietrich*, 1969] are included here.

2. **CEAREX Archives (0/11)** There is some overlap with the National Ocean Data Center (NODC) database. The only extra information comes from the (1989) SIZEX data. The R/V Polarbjorn stations are unusable due to problems with their CTD, but the R/V Haakon Mosby stations are included in spite of salinity values that seem about .04 psu too high.

3. **Meteor Cruise (3/7)** A fairly comprehensive survey made in November of 1989. These are the only available stations for November.

4. **Valdivia Cruise (0/8)** Stations occupied in Feb/Mar 1989.

5. **Greenland Sea Tomography Experiment Deployment/Recovery Cruises (0/13)** A series of deep CTD casts made in the mid-gyre region in September of 1988 and 1989.

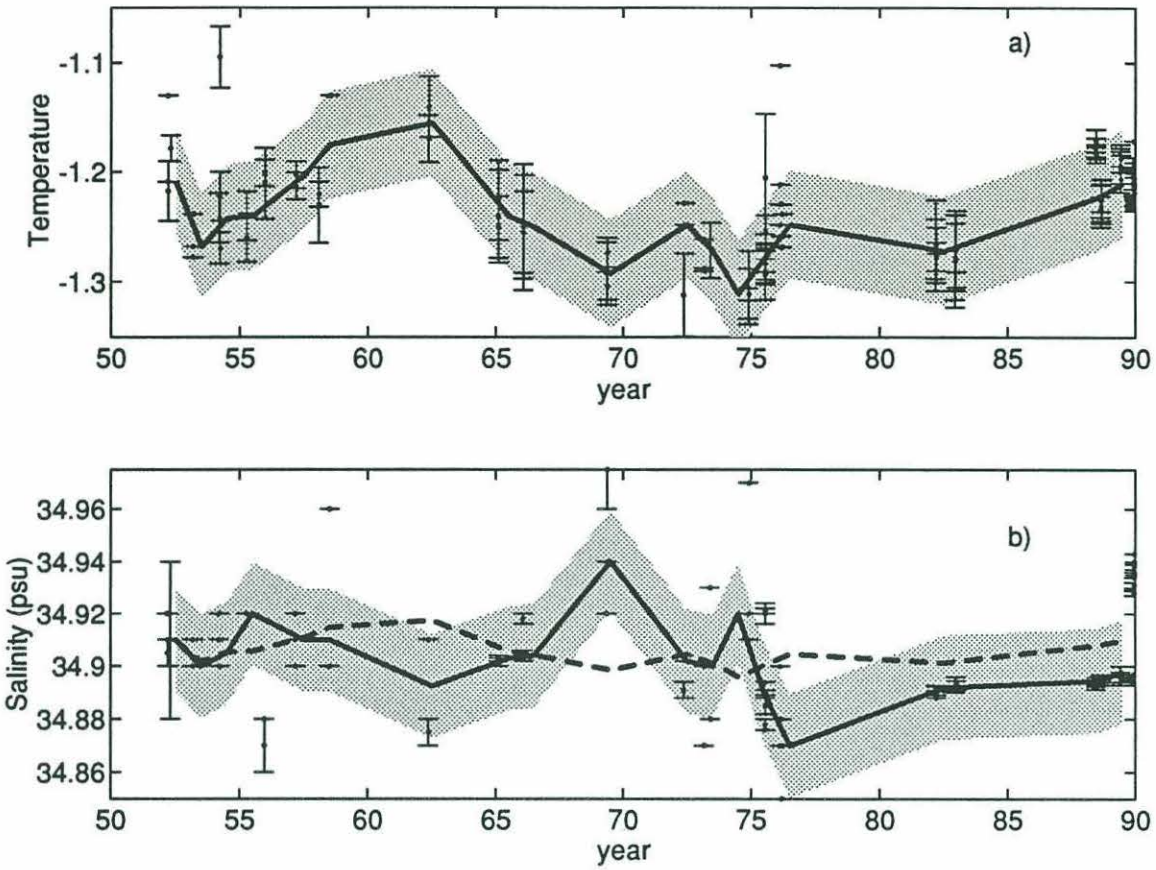

Figure 3-2: All available data below 2000m in the mid-gyre region. For each cast, the error bars shows the range of values seen below 2000m. The thick solid curve joins yearly median values for years with one or more casts. The shaded area indicates estimated error bars based on the spread in the data (see text). a) Potential temperature. b) Salinity. The dashed line shows the salinity that would be necessary to keep $\sigma_{2.5}$ constant for the observed temperatures.

Archived data was extracted from CD-ROMs available from the NODC and the National Snow and Ice Data Center (NSIDC). The majority of the data was obtained from the NODC archives. However, the more recent data is crucial in filling in some gaps that occur in the late fall and winter. Sampling of the mid-gyre region is much better than that of the odden region.

Purely instrumental errors are estimated by examining the temperature and salinity values of the Greenland Sea Deep Water from all casts. Temperature values are in general quite good. A time series of temperature from the bottom of all casts (see figure 3-2a) corresponds well with figure 12 of *Clarke et al.* [1990] (which probably uses much of the same data), showing a maximum in deep water temperature in the early 1960s, followed by

lower temperatures in the 1970s and then a gradual increase through the 1980s. Although there is some obviously erroneous data the scatter about this long-term change, assumed to be an upper bound on the temperature error, seems to be about ±0.05°C. Salinity values (see figure 3-2b) are of lower quality, especially for stations occupied before the 1980s. The scatter in bottom water values (taken to be an upper bound on the salinity error) is at least ±0.02 psu for these earlier observations. No attempt has been made to correct for different salinity standards. Such a correction would be important primarily in the deeper water where no seasonal signal is evident; near the surface the seasonal salinity variation is of order 1.0 (much greater than any needed correction). Also shown in figure 3-2b is a curve representing the salinity changes needed to keep the density of the deep water constant. In general the salinity data are not accurate enough to determine whether this in fact occurs. A number of (pre-1980s) casts show anomalous salinity values at some depths; treatment of these errors is discussed in the next section.

A monthly analysis of Arctic ice concentrations from 1953-1988, compiled from a variety of sources and digitized onto a 60 nautical mile grid by John Walsh of the University of Illinois, was acquired from the National Center for Atmospheric Research (NCAR). This is an extension of the 1953-1977 dataset described in *Walsh and Johnson* [1979]. Quantifying the errors in this dataset is difficult, if not impossible. Ice limits, especially during January-April, can vary enormously even on periods as short as a few days, so that much of the fine-scale information is lost. The southern limit of the odden (when it exists) generally coincides with the Mohns Ridge and the Polar Ocean Front, extending north-eastwards from Jan Mayen, and the ice limits north of the study region generally follow the East Greenland continental shelf (and the East Greenland Front). However the details of the odden can change enormously from year to year. Figure 2.2 in the previous chapter shows several examples of particularly prominent odden/*nordbukta* events. In some years the odden does not appear, and even in years when it does the *nordbukta* does not always appear in the analysis. It is not clear to what extent this is an artifact of the lack of observational data, the coarseness of the time sampling, the spatial grid spacing used, or other problems. Unfortunately, we are considering only a very small part of the grid (only 4 grid points fall into each of the regions being analyzed here), which exacerbates these problems. Note that the variability of the odden will be to some extent a self-correcting problem in terms of the oceanographic sampling, since the location of these observations will be partly determined

by the location of the ice edge. That is, if the odden is slightly further north, then the available observations will also be from a region slightly to the north, and so on.

3.3 Analysis Procedure

All casts were first quality controlled using salinity to identify (and remove) dubious casts. This test flagged casts in which any salinity value at depths greater than 800m was outside the range $34.9 \pm .05$, or in which a change of greater than 0.1 occurred between successive samples at depths greater than 150m. The majority of the casts thus rejected (15/10 in the odden/mid-gyre regions) were of USSR origin, although it should be noted that much of the data was taken by Soviet ships (for example, all of the 1958 IGY summer and winter survey casts in this area, and every October cast).

For each station, observed values were binned into depth ranges of 0–30m, 30–60m, 60–90m, 90–120m, 120–160m, 160–200m, 200-300m, 300–400m, 400–600m, 600–800m, 800–1200m, 1200-1600m, 1600-2000m and 2000-3000m. A "depth-binned" profile was computed by finding the median value for all samples in a depth-bin; if no data was available in a particular bin a "missing-data" flag was set. Depth-binning was done to prevent the far more finely-spaced CTD data from statistically overwhelming the bottle data. Medians are used in preference to means in this entire procedure because they are more robust with respect to the numerous outliers in the data.

Depth-binned profiles were then grouped by month in both regions. June had the most observations, with some months having none or only one observation (see figures 3-3 to 3-5). The sampling pattern has changed qualitatively since the 1950s, as cruises have become more infrequent. However, the number of stations occupied per cruise has increased as surveys become more comprehensive.

Some minor adjustments were made to the groupings (for example the one December cast was grouped with the November casts from the same cruise). Within each month, depth-binned profiles were combined by finding the median value in each depth bin for all profiles. If a particular depth bin had *no* observations, then a T/S value was linearly interpolated from neighbouring values (if the depth range was in the center of the profile), or replicated from the nearest valid T/S value (if the missing value was near the surface or in the deepest bin). No other corrections or smoothing procedures were applied.

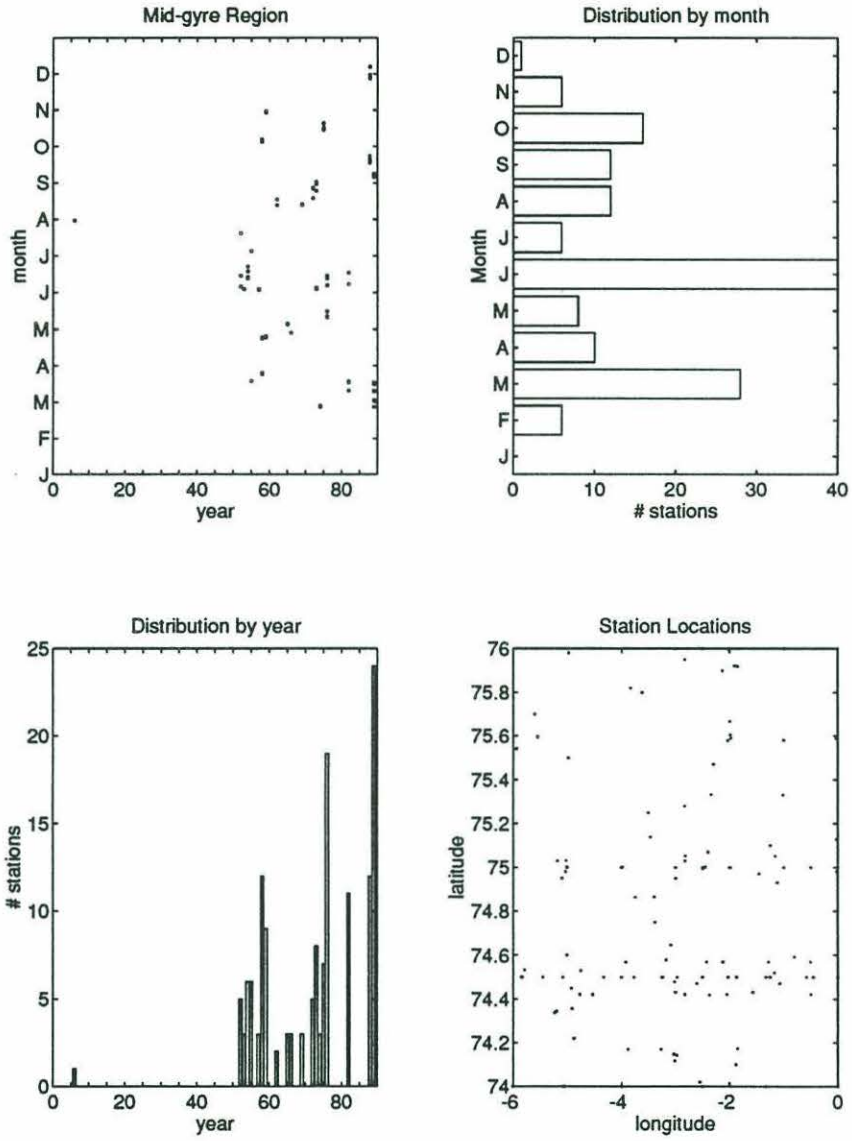

Figure 3-3: Data distribution in Mid-gyre Region. Most observations are in June, followed by March. January and December have no useful data; the distribution is roughly uniform for the other 8 months.

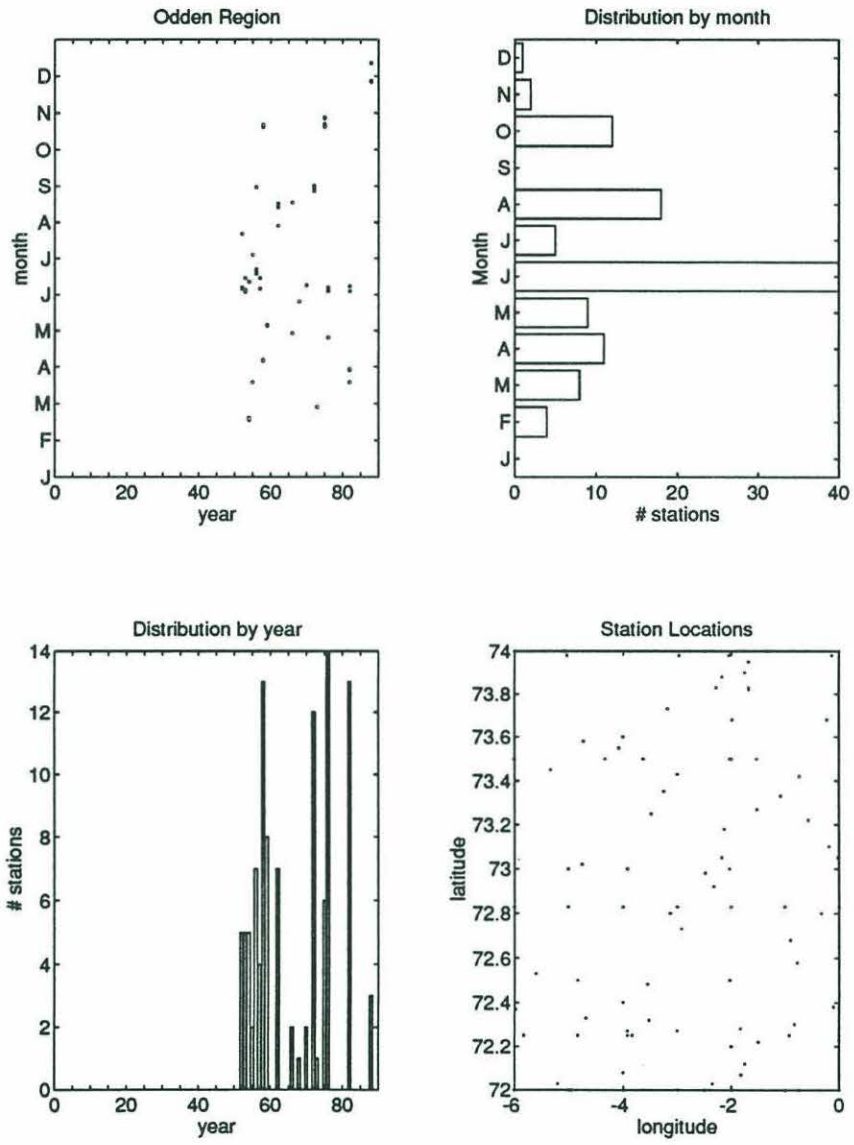

Figure 3-4: Data distribution in Odden Region. Most observations are in June. The late summer/fall is not well sampled.

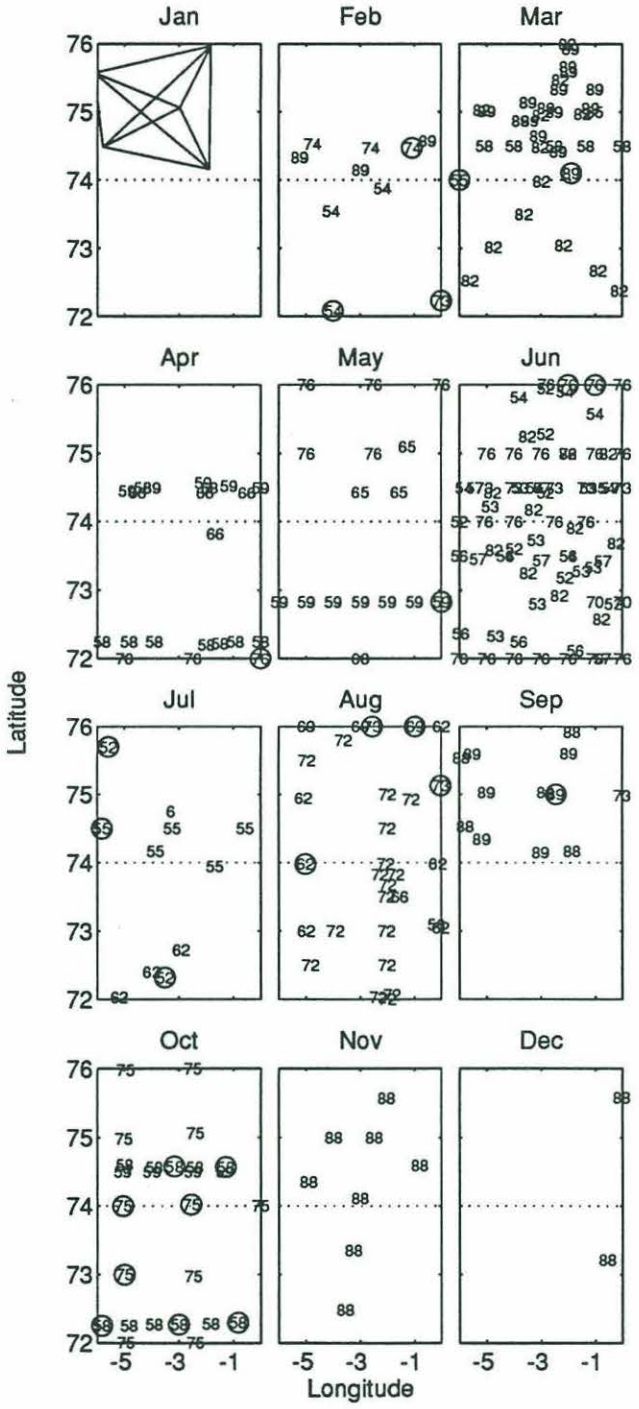

Figure 3-5: Spatial distribution of all casts by month. Casts are labelled by year, and those rejected by the salinity filter (considered to be of dubious quality; see text) are circled. The tomography array is shown in the map for January.

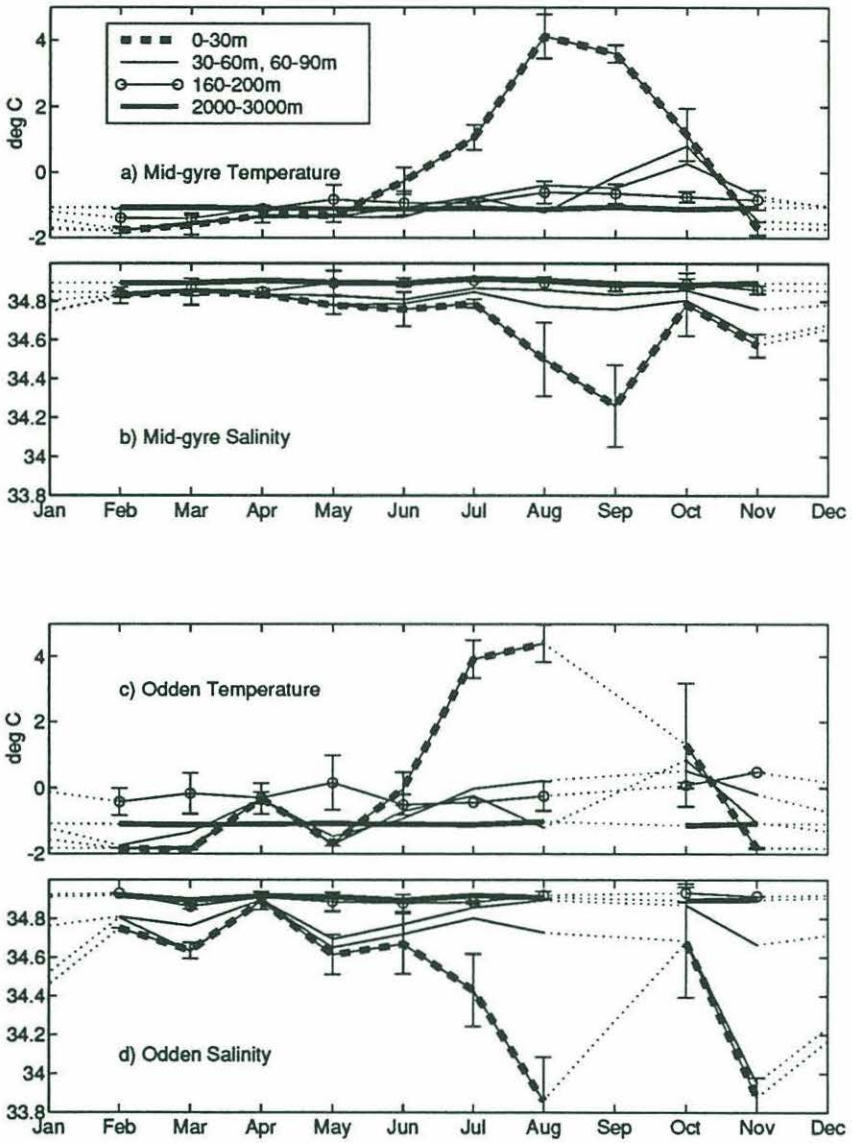

Figure 3-6: Monthly climatologies of temperature, salinity, and ice concentration for mid-gyre (a,b,e) and odden (c,d,f) regions. Curves in (a-d) represent time series of median temperature/salinity in depth ranges of 0–30m, 30–60m and 60–90m representing the surface mixed-layer, 160–200m which coincides with the temperature maximum of the Arctic Intermediate Water, and 2000-3000m which represent deep water values. Months for which no data is available are spanned by dashed lines. Error bars represent an estimate of the interannual variability of the available data using a normalized median absolute deviation statistic for the 0–30m and 160–200m bins. Salinity changes are greatest in the surface bin. Temperature changes are also greatest in the surface bin, but there is another maximum at about 180m (see also Figure 3-7).

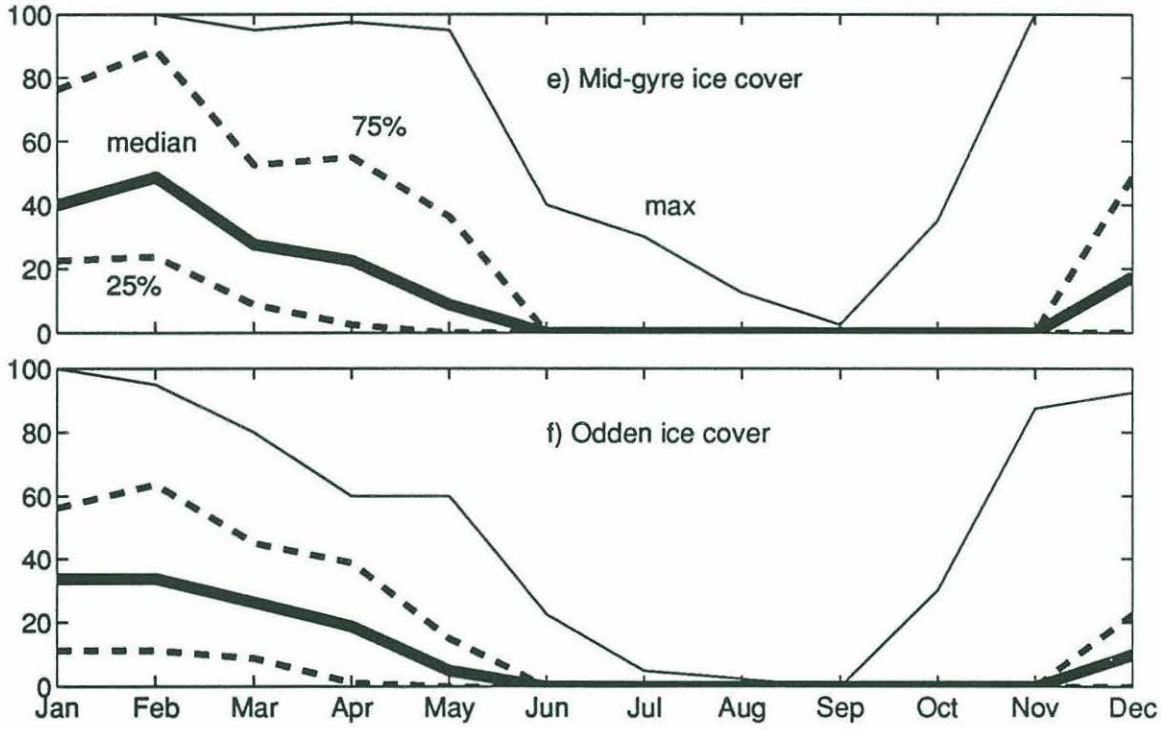

Figure 3-6: Figure 3-6 continued. Ice concentration in the e) mid-gyre and f) odden regions. The distribution of concentrations in each month is shown by 25th, 50th (median) and 75th percentiles. Maximum monthly concentrations seen during the entire climatology are also shown. A suggestion of the *nordbukta* can be seen in March, when odden region concentrations are slightly higher than mid-gyre concentrations.

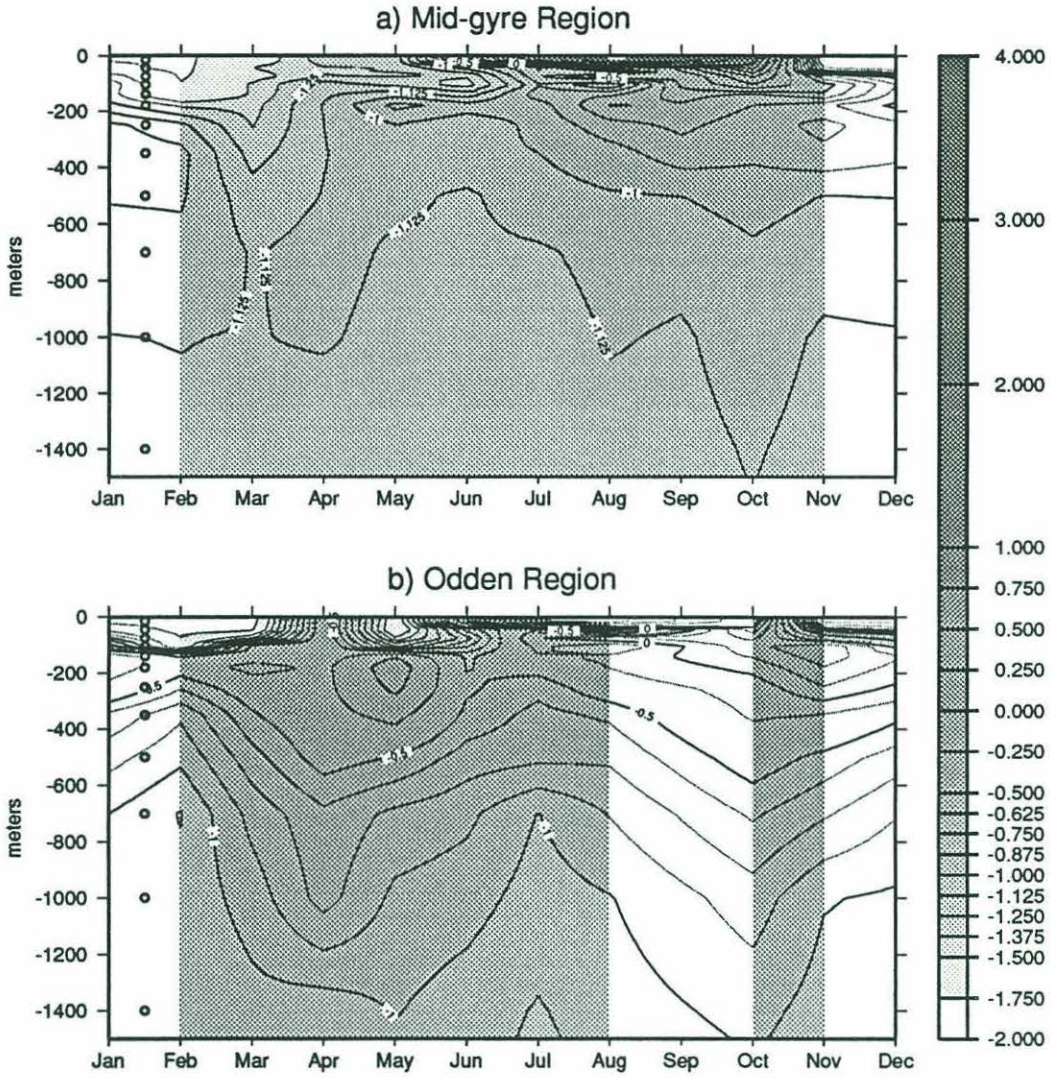

Figure 3-7: Monthly climatologies of potential temperature for the a) mid-gyre and b) odden region. Small circles on the left hand side indicate the centers of depth bins used in the analysis. Months for which there is no data are shown unshaded. The vertical bar at right shows the contour levels used.

The results of the binning procedure are shown in figures 3-6 a)-d) and 3-7. Error bars are estimates of the standard deviation of the data in a particular bin based on a normalized median absolute deviation (MAD) statistic [*Kleiner and Graedel*, 1980]. In general the MAD decays quite rapidly with depth to an asymptotic limit at O(200m). Since error bars near the surface are much larger than the purely instrumental errors estimated above, they can be considered as rough estimates of the interannual variability, albeit not very good ones given the spottiness of the record. It is interesting to note that the interannual variability of salinity as a fraction of seasonal range is much greater than that of temperature.

Also note the generally higher October salinities in both regions (based primarily on 1958 IGY and 1975 data) than in neighbouring months (almost exclusively 1988/89 observations), and the warmer more saline odden upper waters in April (primarily based on the 1958 IGY survey) compared with March and May (observed in 1959 and 1982). The more saline IGY observations have been noted by *Clarke et al.* [1990] and *Bourke et al.* [1992], who speculate on a connection with the the fresher waters of the "Great Salinity Anomaly" [*Dickson et al.*, 1988], via either the freshening of the waters north of Iceland in the late 1960s (seen also in the ice indices of *Mysak et al.* [1990]) or by the freshening of the inflowing Atlantic Water in the Faeroe-Shetland channel in the early 1980s. Neither argument explains the large changes between April 1958 and May 1959 observations in the odden region. It should also be noted that the odden apparently did not appear at all during the 1956/57 and 1959/60 winters, and only briefly during the intervening winters.

An attempt was made to generate an ice climatology indicating the presence of the odden. However, the interannual variability of the ice cover is so strong that averaging served only to indicate a broad band of variability with little discernible spatial structure (the extreme variability can also be seen in the charts of *Vinje* [1977] and the ice anomaly series of *Mysak et al.* [1990]). Instead, a more limited procedure was adopted. For each month, the median concentration for all grid points (4) within the study regions was determined. A monthly climatology was then found by taking a median for all data over the years 1953-1988 (see figures 3-6 e) and f)).

3.4 Seasonal Climatology

Temperature series in the upper 100m of both odden and mid-gyre regions are very similar. Surface temperatures presumably remain near the freezing point from November to February (during this period the surface is covered by a dense ice pack, making direct observations difficult). In March the mid-gyre surface warms to about $-1.4°C$ through mixing with deeper and warmer waters (note the partial homogenization of potential temperature at this time in figure 3-7a), but does not warm much more until May when solar insolation becomes significant. The anomalously warm April surface temperature in the odden region discussed above appears prominently in figure 5b. Mid-gyre and odden surface waters then warm steadily, reaching a temperature of about 4°C in August; the mixed layer depth is of order 50m at this time. In September and October the surface begins to cool, but apparently mixes downwards so that temperatures at depths of 30-90m increase slightly. The timing of this cycle strongly suggests that local surface fluxes alone can explain much of the temperature variability in the upper 100m. This hypothesis will be discussed below.

The water at intermediate depths (i.e. 100-400m), usually classified as Arctic Intermediate Water (AIW) in the mid-gyre region, is coldest in March and warmest in September. In the odden region, warmest temperatures at intermediate depths occur in November, and coldest in February. However it is important to keep in mind that there are *no* observations in December and January - warmest temperatures at intermediate depths may occur during those months even though the surface mixed layer is at the freezing point. There seems to be a distinct separation between the surface and intermediate waters over much of the year; note the temperature minimum at about 100m in the mid-gyre region in April-June (figure 3-7a) separating the surface mixed layer and warmer intermediate waters. This suggests that cooling of the AIW in the mid-gyre region occurs no later than March (and no earlier than December), followed by an inflow of warmer water to restratify the mid-gyre. The classically observed "dome" feature in the center of the gyre is reflected by the generally warmer waters at intermediate depths in the odden region compared to the mid-gyre region.

Small temperature variations can also be seen at depths below 1000m. However, the warm extremes occur in April and October and as noted above, the observations in these months are somewhat inconsistent with the rest of the data. In the deep water below 2000m there is no discernible seasonal signal.

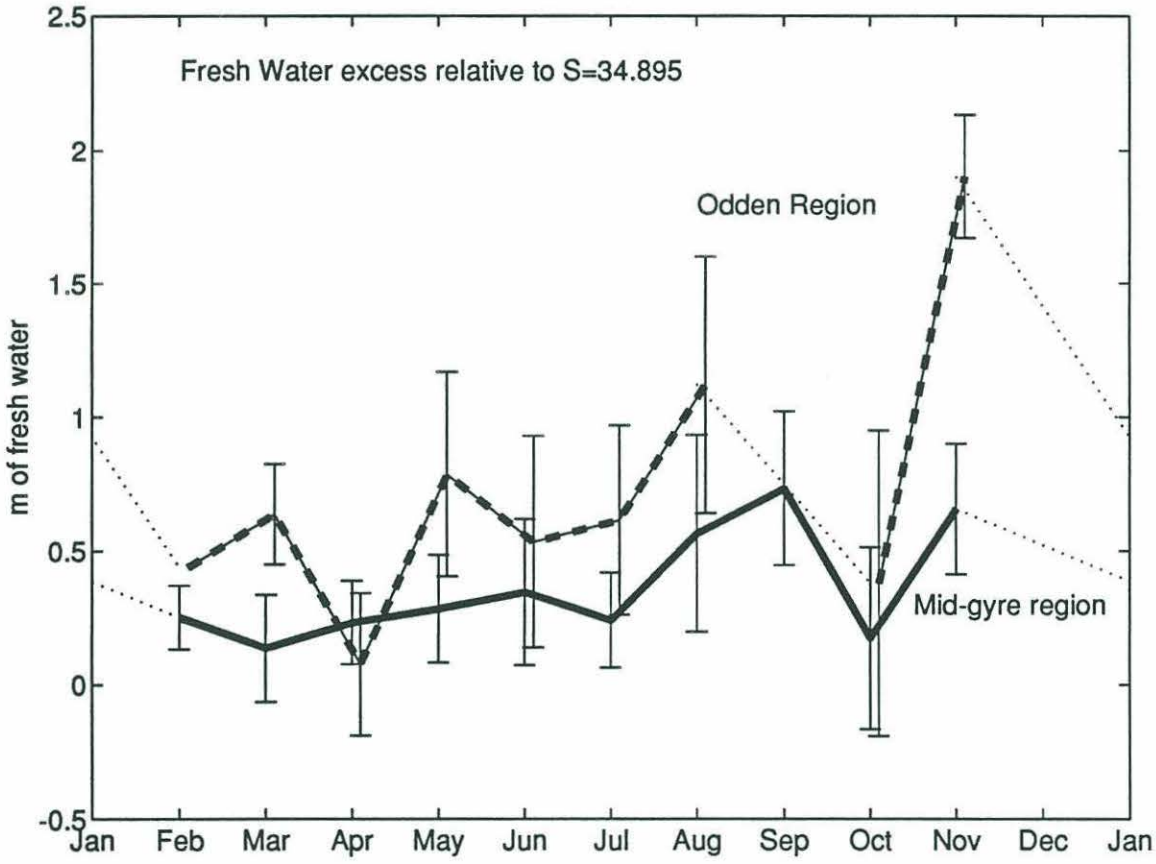

Figure 3-8: Equivalent depth of fresh water relative to a salinity of 34.895 in the mid-gyre and odden regions, Error bars result from carrying through the error bars in the salinity climatology, and can be very large since this is an integral measure.

Salinity changes are more interesting. In figure 3-6 one can see that surface salinity decreases drastically in July and August, some months after the ice cover usually vanishes. The decrease appears to be later and smaller in the mid-gyre region than it is in the odden region. We can compute an "equivalent fresh-water" budget for the upper part of the water column relative to some background salinity $S_o = 34.895$ by partitioning the water column with observed salinity $\bar{S}$ into a depth f of fresh water and a depth s of water with salinity S_o. Then

$$(f + s)\bar{S} = sS_o \tag{3.1}$$

The total depth $D = f + s$ should be greater than the mixed layer depth, but errors will increase with D so it should not be too large. Here we use $D = 120$m. Figure 3-8 shows f for both regions (the equivalent amount of sea ice with a bulk salinity of 7 is about 24% larger). The seasonal change in salinity thus seen to be equivalent to an input of about 50 cm of fresh water in the gyre center and about 100 cm in the odden region. This signal lags the temperature increase by a month or so, suggesting a different - probably non-local - forcing mechanism. After August the *net* rate of freshening appears to slow or halt until November, although the surface salinity increases as the mixed layer deepens. Between November and February this fresh anomaly is eliminated, and the most saline surface waters are observed in March (mid-gyre region) and April (odden region). As noted before, the observed interannual variation in salinity is much greater than that of temperature, making interpretation of a mean seasonal cycle more difficult. Although it is more difficult to accurately compute salinity, this variability is far larger than one would expect on that basis alone (the estimated instrumental error for salinity was estimated above to be at most about ± 0.02, almost an order of magnitude smaller than the ranges of interannual variations shown). Salinity variations below 200m are of the same order as the the instrumental errors and no seasonal signal can be seen.

The ice cover series (figures 3-6 e and f) show densest ice in February, although this can vary significantly from year to year. The ice generally disappears in April or May, although it sometimes persists well into June. Ice can return to this area as early as October or as late as January, although in some years it does not appear at all. Note that the climatological surface temperature series will not necessarily show freezing temperatures to match the climatological ice series because sampling occurs during different years.

Several questions immediately arise:

1. During what period(s) is advection important in the surface waters, and when is a 1-D mixed layer model (MLM) sufficient? (i.e. when are local fluxes enough to explain changes in the mixed layer?)

2. What is the source of the fresh anomaly in July-August?

3. What removes the fresh anomaly in December-January?

To investigate the first question, simulations were carried using a 1-D MLM forced by analyzed fluxes from 1988-89. The MLM is similar to that of *Price et al.* [1986]. The advantage of this model is that turbulent entrainment processes are parametrized using critical Richardson numbers derived from laboratory experiments so that there are (in theory) no tuneable parameters in the model. The disadvantage is that much of the velocity shear driving entrainment arises from inertial oscillations so that forcing with climatological winds is not possible. The model was forced by analyzed 3-hourly surface heat fluxes and wind stresses for 1988-89 available from the United Kingdom Meteorological Office (UKMO) Fine-Mesh Operational Forecast Model [*Bell and Dickinson*, 1987]. A discussion of the quality of these fluxes is given in Chapter 6. No estimates for evaporation and precipitation were available from the UKMO, and rather than using climatological values it was assumed that E-P=0 at all times. The probable errors due to this assumption are discussed below.

Two runs were made, representing fall and spring cases. The fall run was initialized with a typical September gyre center profile, and the model was integrated until the mixed layer temperature reached the freezing point. The spring run was initialized with a typical, almost adiabatic, March mid-gyre profile, and integrated until August. In both cases the resulting temperature profiles were entirely consistent with the historical data (see figure 3-9). Salinity profiles in the fall run were also consistent with the observations, (i.e. no net freshening but an increase in surface salinity as the mixed layer depth increases) however the observed July/August freshening was not reproduced in the spring simulation.

Thus it appears that a significant input of fresh water must be occurring in July and August. However, a 1-D model seems to be sufficient to explain temperature changes. This implies that cumulative surface heat fluxes are similar over a large area with little horizontal advection of heat. There are two possible sources for the fresh water: excess precipitation and/or meltwater from the East Greenland Current. Estimates of precipitation minus

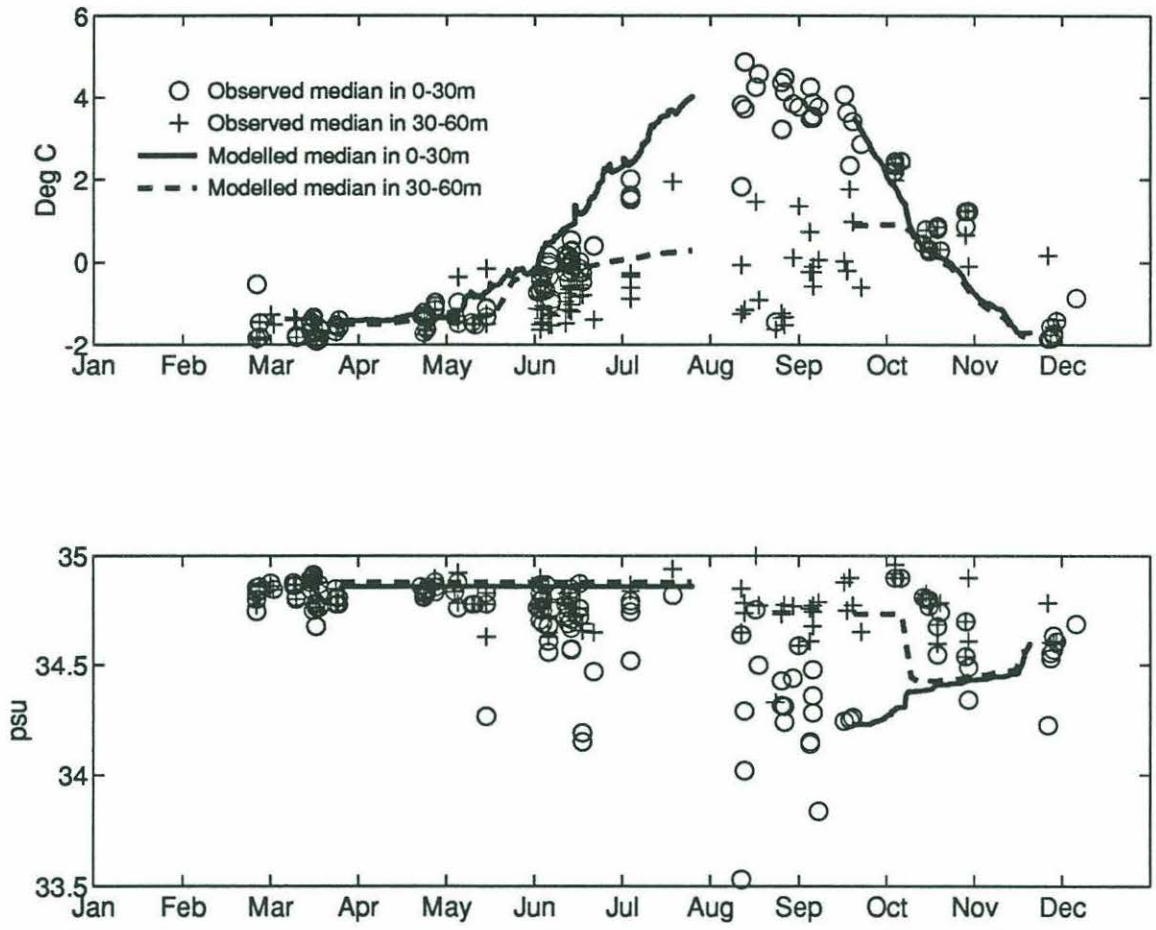

Figure 3-9: Comparison of median mid-gyre temperatures in 0-30m and 30-60m bins with results of MLM simulations using analyzed fluxes from 1988/89. The fall simulation begins in September, and the spring simulation begins at the end of March. Note how the modelled temperatures are consistent with the observations. Salinity observations are quite variable, but salinities in the spring run are not at all consistent with observations, remaining constant while the data shows a surface freshening. In the fall, both observations and model results show an increase in the surface salinity due to entrainment.

evaporation are scarce. The atlas of *Gorshkov* [1983] indicates that that the precipitation excess is about 10 cm/yr in the Greenland Sea gyre, decreasing rapidly to the east. However, the plots of annual cycles at selected locations indicate that the amplitude of the evaporation cycle is comparable to the mean value and that almost no evaporation occurs in July and August; whereas precipitation at this latitude remains fairly steady all year at a rate of about 5 cm/month. Thus one would expect a summer freshening of perhaps 10–15 cm from precipitation alone, implying that about 40-90 cm are due to advection. The fact that the freshening in the odden region appears to lead that in the mid-gyre region (see figure 3-6) is a possible indication that this fresh water is coming from the south-west (i.e. advected by the Jan Mayen Current). However, attempts to track this propagation by analyzing data in other regions (not shown) had inconclusive results due to the scarcity of data. The freshening did decrease to the east – another possible indicator of a south-western origin – although mean evaporation [*Gorshkov*, 1983] also increases dramatically as we move eastwards. *Aagaard and Carmack* [1989] discuss the inflow of fresh water into the convective gyre using different assumptions; they estimate that only about 3% of the fresh water advected by the East Greenland Current (EGC) enters the convective region of the gyre. It is possible that such a small fraction could have significant interannual changes even without considering changes in the fresh water transport of the EGC itself.

The removal of this fresh anomaly is probably due to brine rejection from ice formation. Formation of about 65cm of ice with a bulk salinity of 7 (typical of newly-formed ice) is enough to remove the mid-gyre anomaly, and about twice as much ice formation is needed to remove the anomaly in the odden region. Winds are generally from the north during the winter and average 5-10 m/s, which would tend to blow the newly-formed ice south-westwards at speeds of 10-20 cm/s, using the generally accepted rule-of thumb that ice drifts at about 2% of the wind speed at about 20° to the right of geostrophic winds [*Gow and Tucker*, 1990] or 40° to the right of surface winds [*McPhee*, 1990]. This suggests the following hypothesis to explain the formation of the odden tongue: By November a fresh anomaly exists over the whole Greenland Sea, but the freshening is much less over the gyre center because of the predominantly cyclonic circulation. The fresh surface water is much lighter than the warmer, more saline intermediate waters and hence a large density gradient exists at the base of the mixed layer. This acts to both confine the cooling to the mixed layer so that it can reach the freezing point, and inhibits mixed layer deepening. Ice forms

over the whole gyre at roughly the same rate; over the gyre center the fresh anomaly is erased earliest, enabling entrainment of the deeper (and warmer) waters and preventing further ice formation. Immediately to the south the anomaly is not eliminated as soon, and ice continues to be formed in the odden tongue.

3.5 Discussion

The surface temperature in the central Greenland Sea responds primarily to surface fluxes. During much of the year a 1-D mixed-layer model can work reasonably well at predicting surface temperature. This does not necessarily imply that horizontal mass transport is negligible - merely that it occurs on scales smaller than those over which the surface fluxes change so that heat advection is not significant. In fact a significant inflow of fresh water occurs in July and August, giving rise to the classical conundrum in which the deep water cannot be renewed because the surface water is too fresh to sink even when cooled to the freezing point. This freshening is greater, and apparently occurs a little earlier, in the southern part of the gyre relative to the gyre center, and is mostly due to horizontal advection rather than excess precipitation. Interannual changes in the fall salinity can be large.

During October and November the surface waters are cooled to the freezing point, after which ice begins to form. The fresh anomaly creates a large density gradient across the base of the mixed-layer which inhibits mixing with the warmer waters below and allows the mixed-layer to remain at the freezing point. During the winter the winds are strong and from the north, causing the newly formed ice to drift south-westwards. Brine rejection resulting from the formation of ice slowly erases the fresh anomaly and preconditions the gyre. Towards the end of the winter, the anomaly will be removed first in the gyre center (since the freshening was weakest there). Thereafter, continued cooling will result in a rapid deepening (and warming) of the mixed-layer, precluding further ice growth. To the south, ice formation will continue in the odden region - thus an ice tongue will appear to the south of a bay over the center of the gyre. In late April the deep mixing in the mid-gyre region will cease as the net surface fluxes change sign, and the warm AIW will begin to return to the mid-gyre region, slowly flowing in from the gyre edges during the remainder of the year.

This implies that deep water formation depends on a delicate balance between the

amount of fresh water entering the gyre and the winter temperatures and winds. In turn the amount of fresh water entering the gyre will depend on the amount of fresh water in the East Greenland Current (which will be sensitive to springtime heat fluxes and the transport through the Fram Strait, both of which can have large interannual changes), and the fraction thereof diverted into the gyre – which will presumably be affected by surface winds. A large amount of fresh water and a mild winter in which winds do not quickly remove newly-formed ice will result in little deep mixing, whereas a small fresh inflow and a bitter winter may result in a large amount of deep mixing. The depth to which convection occurs may also be limited by the amount of underlying AIW, or equivalently the strength of the cyclonic circulations [*Meincke et al.*, 1992].

An interesting corollary to this picture is that it may be possible to infer the onset of deep water formation from satellite imagery of ice cover. Since ice formation acts to precondition the gyre by adding salt to the upper waters, and deep mixing must occur before April (before the sun begins to warm the upper waters), the timing and magnitude of a decrease in areal coverage of ice (especially in the gyre center) could also act as a proxy for the strength of deep mixing in a given year. To test this idea, we consider the period 1982-1991 (for convenience, unless a particular month is given, we will refer to the period summer 1981-summer 1982 as 1982 and so on in the following discussion). Figure 3-10 shows mean ice concentrations at the end of every month for this period for the mid-gyre and odden regions. The Walsh ice climatology (presumably largely based on satellite observations during this time period) was used for the period 1982-December 1988. To extend the series, mean ice concentration for the last week of every available month was computed from SSM/I data (years 1988-1991, excepting December 1987). The overlapping periods of the 2 time series are used to indicate the consistency between the two ice products. Also shown is the annual mean wind stress curl over the Greenland Sea taken from figure 4 of *Meincke et al.* [1992] for the years 1982-1987, and computed from UKMO analyses for 1989. Convection depths were taken from a variety of sources. In 1982, [*Clarke et al.*, 1990] found the mixed-layer depth to be about 100m in the Greenland Sea using the usual criterion of density changes less than $0.02 kgm^{-3}$. However, as complete homogeneity was not found in the climatology derived above, we quote instead the depth of approximately 500m at which an oxygen discontinuity was found. In 1984, *Nagurny and Popov* [1985] apparently found convection to the bottom, although this conclusion is regarded as questionable by *Meincke*

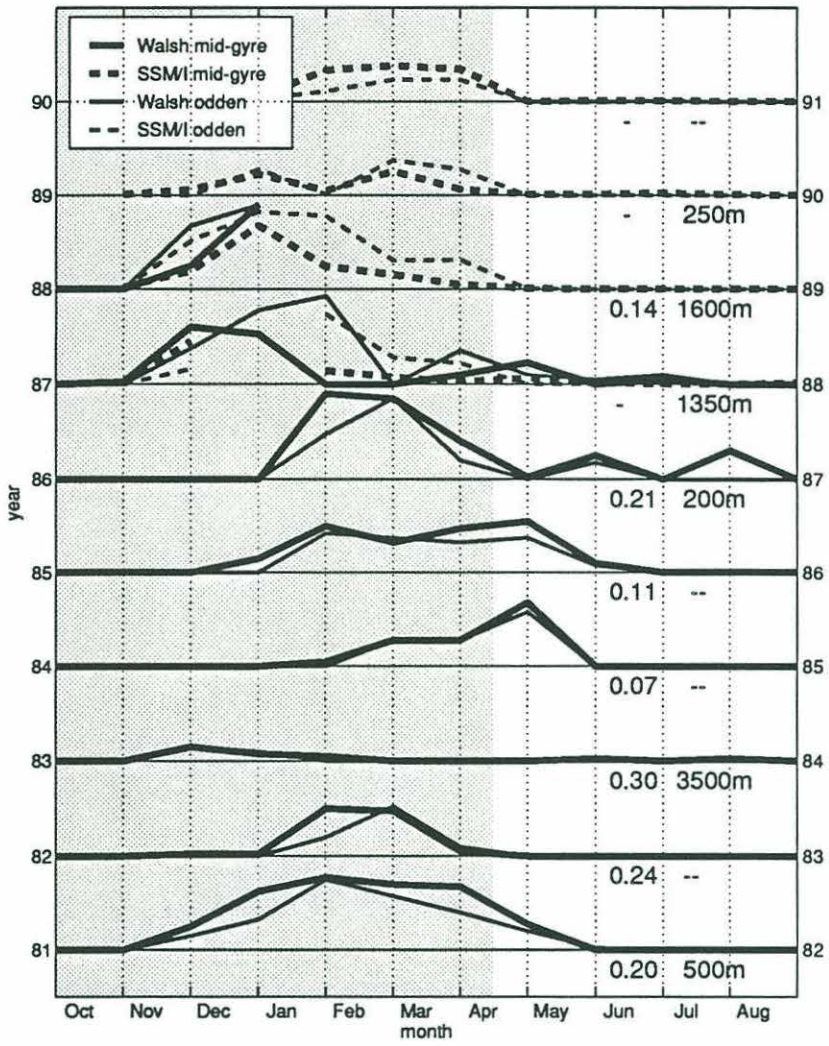

Figure 3-10: Comparison of ice concentrations in the Greenland Sea with observed depths of convection during 1982-1991. Curves represent mean ice concentration at the end of each month in both the mid-gyre (thick) and odden (thin) lines, for years 1981/1982, 1982/1983, etc., offset by concentrations of 100%. Ice concentrations are derived from the Walsh ice climatology (solid) and SSM/I data (dashed lines). Consistency of the 2 ice products can be judged from the degree of overlap during 1987-1988. The shaded region indicates the portion of the year during which surface waters are cooled. The first column of numbers represents the mean wind stress curl over the Greenland Sea (in units of Pa/1000km). The second represents the observed depth of convection during that winter (for details, see text). Years for which no numbers are available are indicated by a dash. Deep convection seems to be associated with the early appearance of ice and a rapid return to low or zero levels. Shallow convection seems to be associated with years in which ice arrives later, and/or lingers.

et al. [1992]. During 1987-1989 we take the values of 200m, 1350m, and 1600m from *GSP Group* [1990], and from 1990 we have a convection depth of 250m from *Budéus et al.* [1993] (note that these authors find a convection depth of some 2200m for 1989).

Examining figure 3-10 we find that the two years showing deepest convection (1984 and 1989) also show ice appearing quite early, in November and December, followed by several months of very low (or zero) concentrations before mid-April when surface heat fluxes change sign and begin to warm the surface waters. In fact, the odden does not appear at all during 1984. Conversely, the years in which shallow convection was observed (1982, 1987, and 1990) seem to show ice appearing rather later, and/or remaining at constant levels for a longer period of time. It is also interesting that the mean wind stress curl is greatest during 1983-1984, so that the possible very deep convection during this winter is also consistent with the idea of *Meincke et al.* [1992] that a stronger cyclonic circulation allows convection to deeper levels by keeping AIW from entering the gyre center. In contrast, wind stress curl is quite low during 1988-1989, another period of deep convection, and it is likely that changes in the cyclonic circulation only occur on time scales longer than several years (the time scales of baroclinic Rossby waves). On the other hand, wind stress curl is probably correlated with wind stress (and thus the amount of available wind mixing energy), and also, through their wind speed dependence, with latent and sensible turbulent heat fluxes, both of which may also be crucial in determining the depth of convection. In any case, this simple analysis, although highly speculative, seems to indicate that details of the ice cover are strongly linked with convection.

Chapter 4

Acoustic Propagation in the Greenland Sea

The Greenland Sea Tomography Experiment was the first high-latitude tomography experiment to be performed. Acoustic propagation in high latitudes is qualitatively and quantitatively different from that in mid-latitudes, since it is characterized by surface and near-surface ducts and is thus mostly affected by near-surface processes. In this chapter we will first discuss the details of the tomographic deployment, and then describe the characteristics of acoustic propagation that were observed during the experiment.

4.1 Greenland Sea Tomography Experiment

The Greenland Sea Tomography Experiment consisted of a year-long deployment of six moorings in the Greenland Sea Gyre (see figure 4-1). Moorings were placed to span the gyre center in a pentagonal array about a central element. Paths joining the moorings can be grouped by nominal length into 3 categories: short paths of nominal length 105km radiating out from the central mooring, medium length paths (125km) around the edge of the array, and long paths (200km) crossing the array. This grouping considerably simplifies the task of understanding propagation. Water depths were about 3600m. The nominal 194 dB re 1 μPa @ 1m HLF-5 acoustic sources were placed on taut moorings as close to the surface as prudent, at a nominal depth of 95m. Bathymetry measurements were taken along all tracks but no seamounts high enough to cause problems were found (see figure 4-2). Immediately below the sources was a 4 element vertical line receiver array. Hydrophone

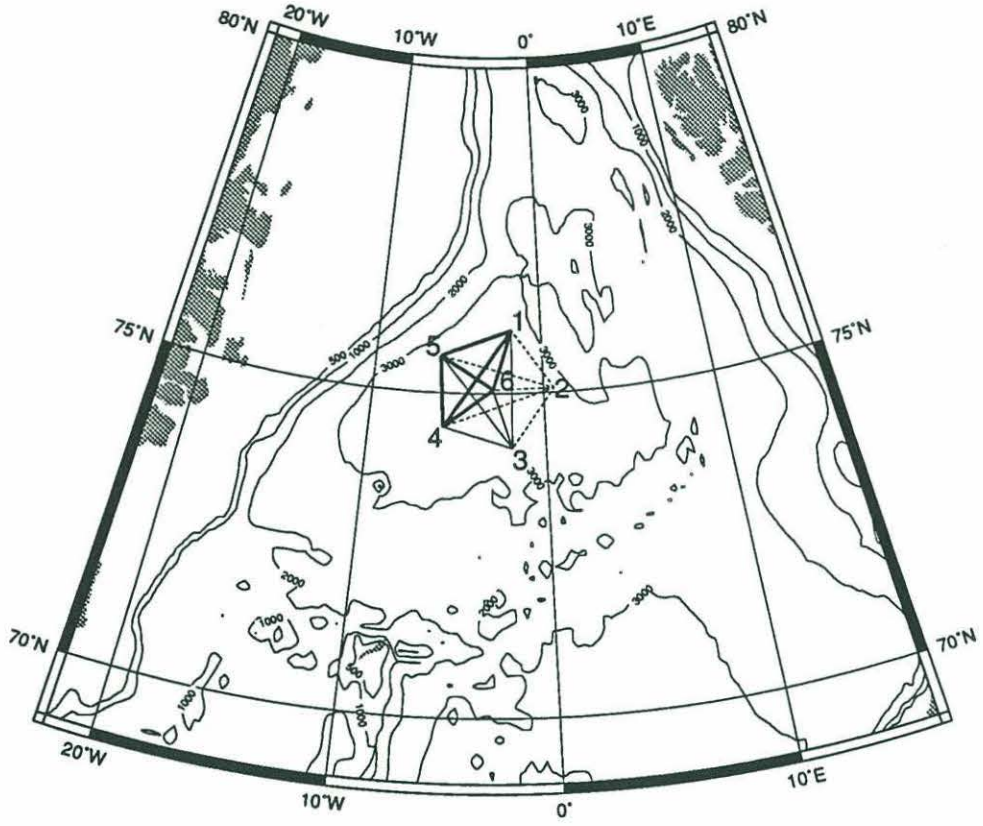

Figure 4-1: Greenland Sea Tomography Experiment. Mooring 2 failed completely, and mooring 3 acted only as a source, thus reciprocal transmissions were made over the paths indicated by thick lines, and one-way transmissions over the paths indicated by thin lines. No useful transmissions were recorded over dashed paths.

elements were placed 9m apart (about $3/2\lambda$) giving a 3dB beamwidth of about 9° which was sufficient for resolving up and down-going rays. Moorings 1, 2, 3 and 6 had two additional deeper receiver elements used to identify near-surface acoustic normal modes. Moorings 4 and 5 used Webb Research Corporation receivers; the other moorings incorporated Scripps Institution of Oceanography AVATAR receivers [*Worcester et al.*, 1985].

Each mooring was locally navigated using a bottom-mounted 3 or 4-element transponder array, so that transceiver positions were always known to a nominal accuracy of a few meters relative to their anchor location even though horizontal tidal and inertial motions of up to ±300m (more usually ±100m) were observed (see figure 4-3). Mooring motions did not reflect predictions of either tidal velocities or displacements; see Appendix B for details. Absolute mooring positions were surveyed after deployment using LORAN-C; as will be discussed later there appear to be errors of up to several hundred meters in these positions. Corrections to travel-time observations for mooring motion relative to anchor locations were computed after recovery.

On-board clocks on each mooring were supposed to keep correct time to within 100 ms over the deployment period (correctable to within 1 ms during post-processing). However, the clock on mooring 5 drifted about 1.2s over the year, and correction to better than about 2ms absolute at any time during the deployment was not possible (see appendix A), although this error is very smooth in time and will change by less than 1 ms over a time scale of weeks. This has little impact on the temperature inverses.

511-bit phase encoded PN-sequence tomographic transmissions [*Spindel*, 1985] with a center frequency of 250 Hz and a bandwidth of 100 Hz were made every 4 hours. "Sing-around" time for the array was 8 minutes, so that reciprocal transmissions could be used to estimate mean current velocities (not discussed here). Each transmission consisted of 4 repetitions of the 8.176 sec PN-sequence, 3 of which were coherently averaged at the receiver. Although transmissions were made every 4 hours to allow resolution of tidal and inertial signals, the westernmost moorings (numbers 4 and 5) had limited storage capacity and only recorded the six receptions of every third day. Sequence removal (or pulse compression) for the unprocessed receptions at these moorings was done after recovery of the instruments. At the other moorings, every 10th reception was stored unprocessed; the remaining receptions had sequence removal done *in situ* and only samples near peak values were stored. The signal bandwidth implies a pulse width of about 10 ms, although in mooring 4 and 5 an

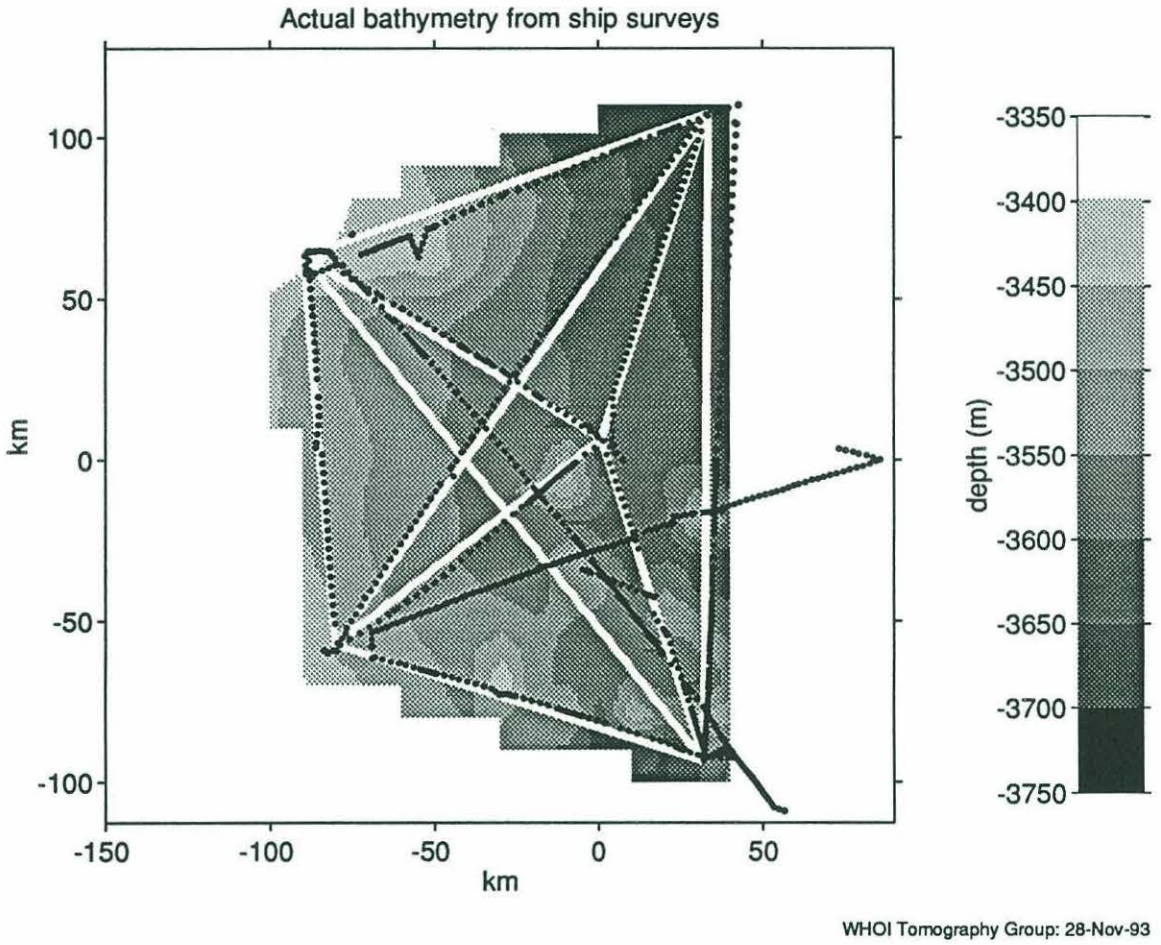

Figure 4-2: Bathymetry for the Greenland Sea Tomography Experiment determined from ship echo-sounder records made during the deployment and recovery cruises. Depths were computed using an adiabatic soundspeed profile, binned into 10km squares, and a complete surface was interpolated using an inverse-distance weighting scheme. Ship tracks are indicated by dotted lines and actual mooring paths by solid lines. Contour intervals are 50m. The bottom slowly shoals towards the west from a depth of about 3700m in the north-east corner. A number of seamounts can be seen in south-eastern part of the array.

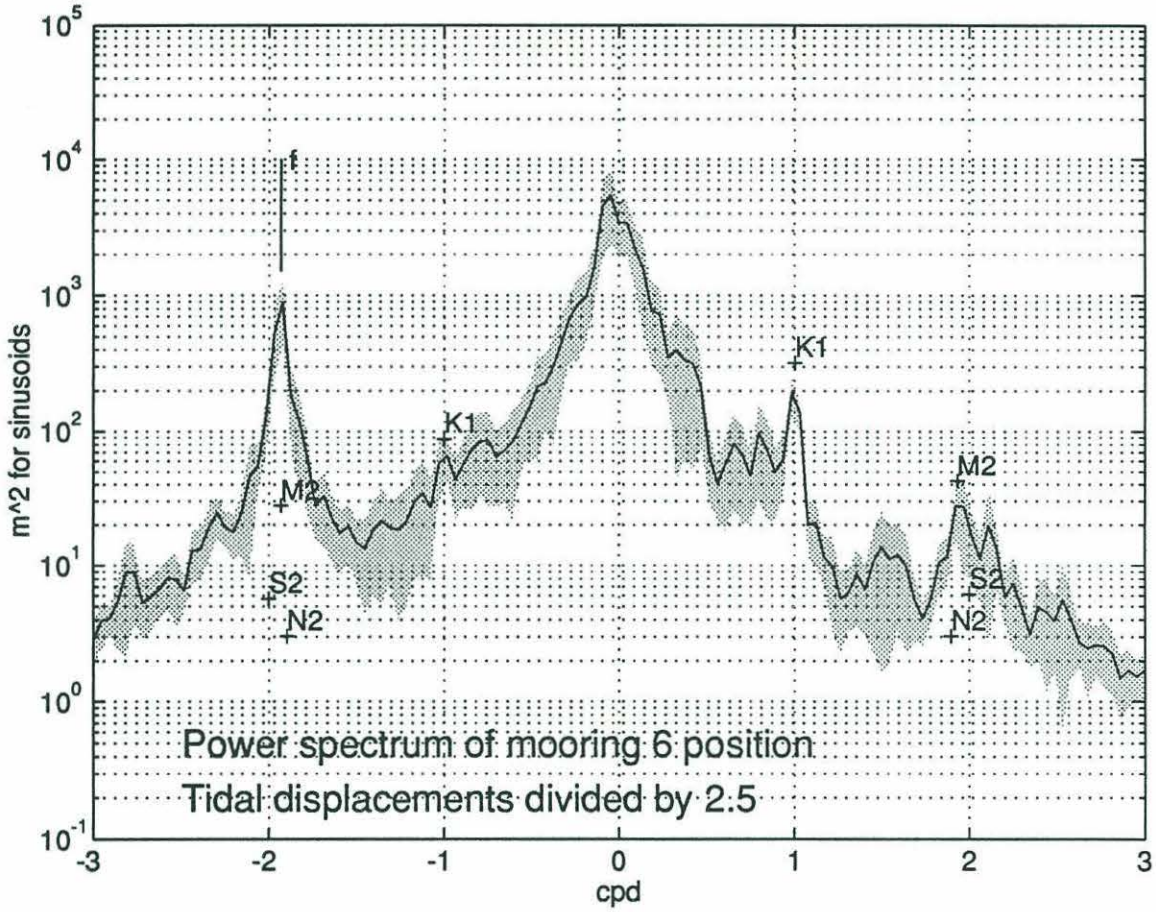

Figure 4-3: Rotary spectrum of mooring 6 position, computed from hourly observations. Vertical scale has been normalized to indicate the correct amplitude for line frequencies. Computed displacements for various tidal components are also shown (B. Gjevik, pers. comm. 1990), divided by 2.5. Shaded region indicates uncertainty in spectral estimate. Note the large inertial peak.

Mooring	Position	Transmission		Comments
		First	Last	
1	$75°58.08'N, 001°50.00'W$	17/9/88	20/8/89	Intermittent Rx failure
2	$75°03.88'N, 000°38.20'E$	30/9/88	14/10/88	Early battery failure
3	$74°09.38'N, 001°52.90'W$	28/9/88	21/8/89	Rx failure
4	$74°28.90'N, 005°47.30'W$	19/9/88	7/9/89	
5	$75°34.27'N, 006°07.70'W$	15/9/88	29/8/89	Large clock drift
6	$75°03.60'N, 002°58.00'W$	21/9/88	27/7/89	

Table 4.1: GSP-88 Tomographic moorings

analog prefilter of bandwidth 67Hz (instead of 100Hz) was mistakenly installed. Thus the received pulses were somewhat broader. Complex demodulated signals were sampled every 8 ms at moorings 4 and 5 and every 4 ms at the other moorings.

As well as tomographic receptions the receivers also recorded ambient noise, pressure, and temperature measurements for engineering purposes. These observations have proved useful in interpreting the tomographic data and inverses and in correcting the clocks, and the ambient noise measurements have also proved quite interesting in their own right [*Lynch et al.*, 1993].

Moorings were deployed in September of 1988 and recovered in September of 1989 (see Table 4.1). The instrument on mooring 2 failed after deployment due to leakage in a cable connection and was recovered and redeployed. However, it then failed completely after approximately one month of service. The receiver failed on mooring 3, but the source continued to function throughout the experiment. Receptions at mooring 1 became increasingly erratic in the summer of 1989 because of disk drive problems. Data storage on all instruments generally ended near the end of July 1989 when no more disk space was available, thus there exists a gap of a month or more between the last recorded tomographic receptions and instrument recovery. Thus we have two-way travel-time information along 6 paths, and one-way travel-time information over 4 additional paths.

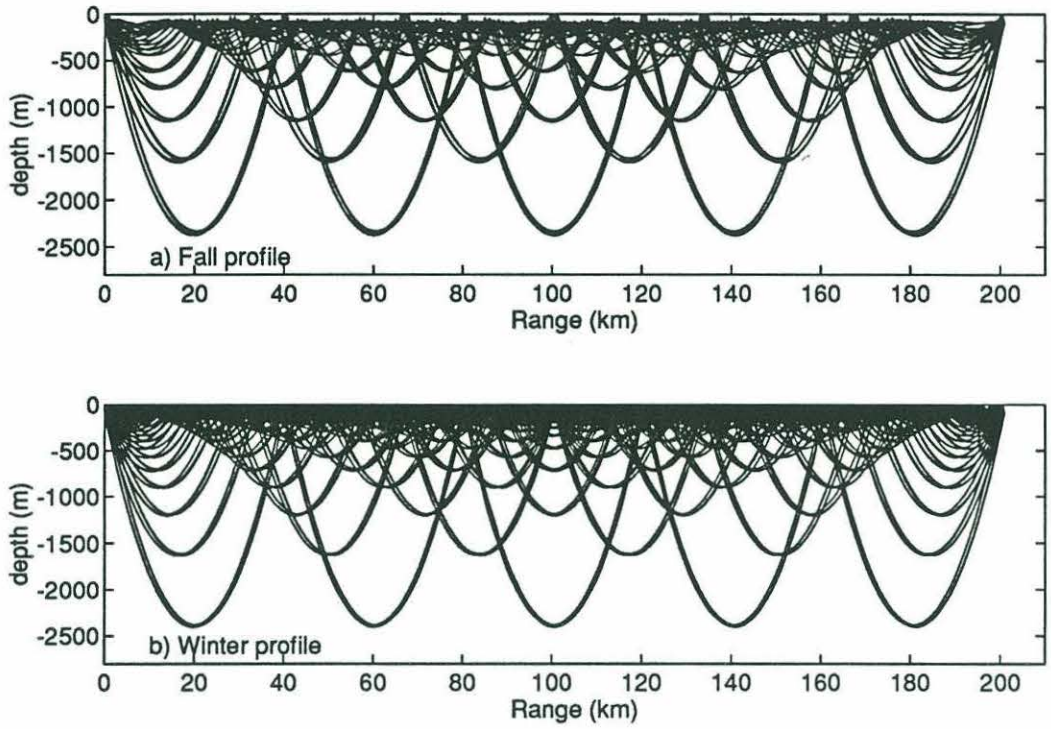

Figure 4-4: Eigenrays for a Long Path (1-3, 1-4, or 3-5) in a) fall and b) winter.

4.2 Acoustics in the Greenland Sea

4.2.1 Forward modelling of propagation

Exact solutions to the acoustic wave equation are difficult to generate in all but the most ideal cases, and in practice one of a number of approximations are usually used. Historically, tomographic inversions have been performed using the ray paradigm, a high-frequency approximation in which propagation of narrow "almost-plane" wave-front segments are traced through a spatially varying medium ignoring diffraction effects [*Brekhovskikh and Lysanov*, 1991]. This is a very efficient representation when travel-times for pulse propagation along various rays differ substantially, and leads naturally into a fairly simple statement of the inverse problem. Rays that travel from the source to the receiver are called *eigenrays*, and in general sound travelling along different eigenrays will arrive at the receiver at different times.

However, solution of the wave equation for propagation "near" a channel axis (i.e. a local sound-speed minimum) usually involves the summation of a large number of rays that arrive almost simultaneously, and it becomes easier to formulate a solution in terms of a small

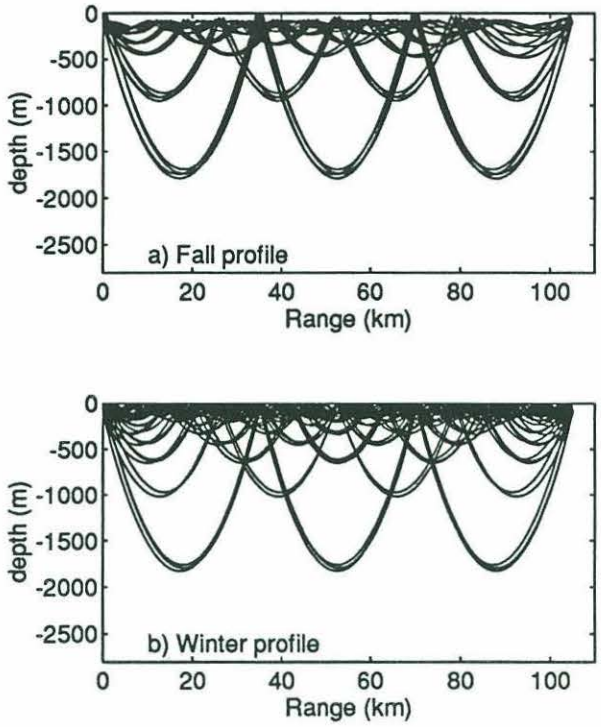

Figure 4-5: Eigenrays for a Short Path (6-4, 6-5, 6-1, or 6-3) in a) fall and b) winter.

number of normal modes (i.e. the eigenfunctions of the vertically separated wave equation [*Brekhovskikh and Lysanov*, 1991]). In a WKB sense, both solutions are equivalent, and a ray can be expressed as the sum of a number of constructively interfering normal modes (a "mode bundle"), and conversely a mode can be expressed as the sum of a number of constructively interfering rays (a "ray bundle") [*Guthrie and Tindle*, 1976]. For convenience we commonly speak of *ray* propagation for energy that travels far from the channel axis, and *mode* propagation for energy that is trapped near the channel axis. Between these two cases is a transition area where neither description is particularly efficient.

To first order the sound-speed profile in the Greenland Sea is almost linear, with sound speed increasing as a function of depth due to pressure effects only. Thus all rays are upward-refracting/surface reflecting[1] and the channel axis is near the surface, in sharp contrast to the usual mid-latitude case where the channel axis lies below the seasonal thermocline at depths of about 1000m and rays do not necessarily reach the surface.

The travel time for eigenrays increases as their turning depth (the maximum depth

[1]Ignoring for the moment the fact that shallow near-surface rays are actually trapped below the summer mixed-layer, but what's a small generalization between friends

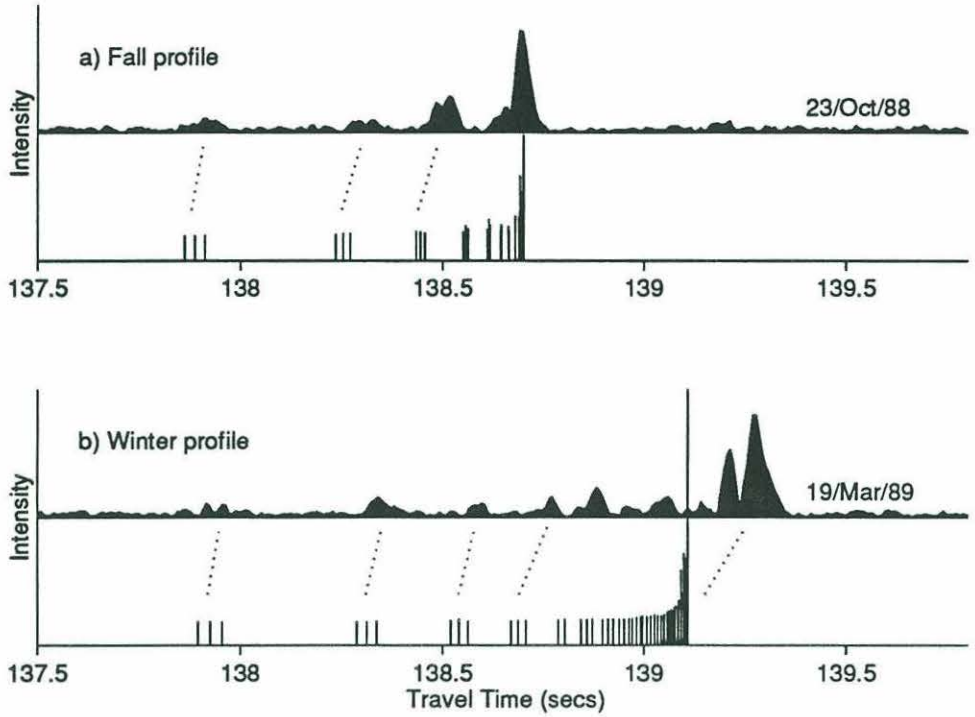

Figure 4-6: Predicted Arrival Pattern for a long path in a) fall and b) winter, using a profile similar to that actually seen, compared with actual receptions at the topmost hydrophone at mooring 4. Separate rays within the ray groups are generally not resolveable when processing data from a single hydrophone. Identified groups for these waveforms are indicated by dotted lines

attained by the ray) decreases. The earliest acoustic arrival is associated with the deepest-travelling rays, and the latest arrivals are associated with near-surface modes. In this paper we will approximate the behavior of the last-arriving mode (the largest peak just before a final cut-off of energy) by using a "last" ray. This is not unreasonable since the the rays making up the "ray bundle" equivalent to the last-arriving mode all traverse approximately the same depth range of the ocean - thus they provide little independent information, and the information contained in the "last" ray is almost equivalent to that contained in the last mode. As we shall show below, the purely ray inverses are good enough to describe the large-scale oceanography.

Figures 4-4 and 4-5 show plots of eigenrays for short and long paths using typical sound-speed profiles from the fall (September) and winter (February). Propagation along deeper rays is virtually unchanged throughout the year. Near the surface one can see that energy is trapped below the warm surface mixed layer as shallow rays (or low order modes) in

the fall, but that it reaches the surface in winter. Because of the near-axis location of the source/receiver pairs, eigenrays occur in groups of 4, all of whom have the same number of lower turning points. The earliest ray in a group travels downwards from the source and arrives at the receiver from below. The latest ray in a group travels upwards from the source and arrives at the receiver from above. The middle rays either depart below and arrive from above, or depart above and arrive from below. The transmitted pulse and receiver array beamwidth parameters imply that two rays groups can be resolved for the short paths, three for the medium length paths, and four for the long paths, followed by a large "transition" region in which nothing can be resolved. In turn this transition region is followed by a "last" ray of near-surface propagation. Predicted travel-times over a long path for fall- and winter-like profiles are shown in figure 4-6. The ray arrivals come in groups of 4, although the 2 middle rays in each group can only be resolved by angle since they are almost coincident in time. In theory the early and late arrivals within a group are spaced far enough apart that they can be resolved in time as well as by angle. Largest travel-time changes over the year occur for the last arrivals. Amplitudes generally increase with arrival time.

4.2.2 Observed acoustic propagation

Figure 4-6 also shows the arrival pattern actually observed over the 1-4 path at two different times. Only data from a single hydrophone is plotted. The locations of various ray groups can be immediately discerned (these identifications are shown by dotted lines). Individual rays within a group can sometimes be identified, but in general beamforming is always required to identify rays on the long paths. Over short paths this is not always the case. Note that the observed travel times are different than those generated using the "typical" soundspeed profiles. These differences are the raw data used in the tomographic inverses which are discussed at greater length in the next chapter.

In order to show the seasonal changes more easily, a dotplot is used. Figure 4-7 shows dotplots for the observed acoustic propagation after correction for mooring motion and clock drift for the uppermost hydrophone in the vertical array for two different paths. To generate these figures, the travel-times for the 40 highest peaks in each individual arrivals (two of which were shown in figure 4-6) are plotted as dots along a vertical line. Successive transmissions are plotted on successive vertical lines to the right. Eigenray travel-times

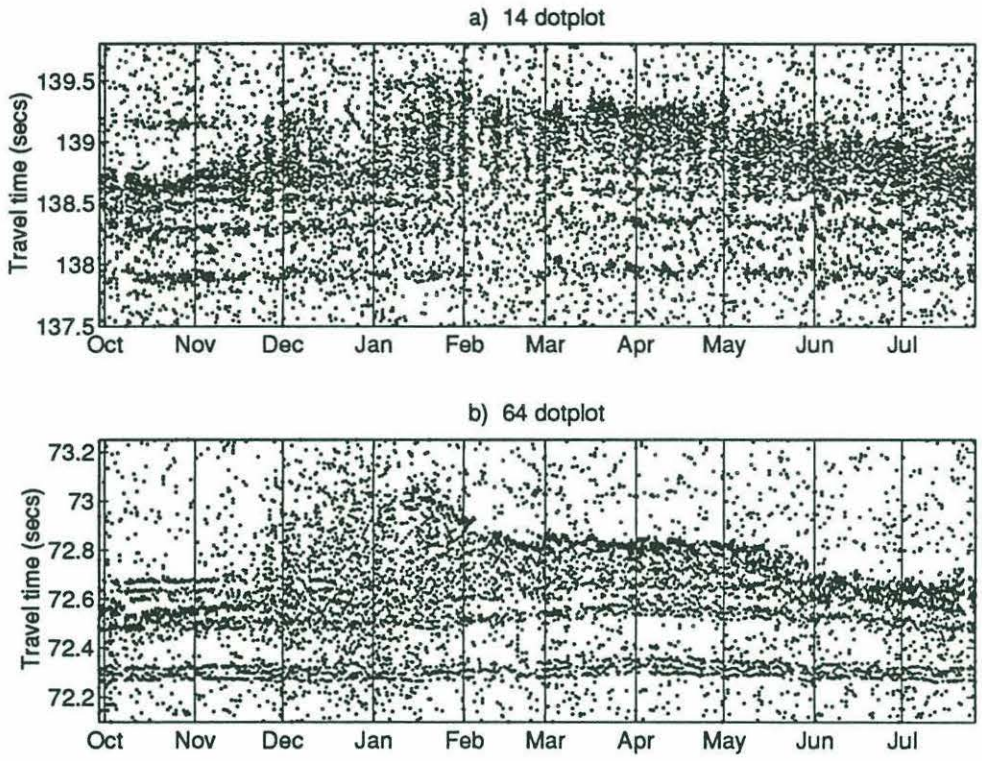

Figure 4-7: Dotplots from topmost hydrophone for a) long (1-4) and b) short (6-4) paths. Each received transmission is displayed along a vertical line, and has been corrected for clock and mooring motion. The 40 largest local maxima in each transmission are shown by dots. Three-day gaps have been eliminated for visual clarity. Ray arrivals can be seen as nearly-horizontal lines. Note the difference in vertical scale for both figures.

will then appear along roughly horizontal lines in a background noise. The two day gaps in the recorded data have been eliminated to increase visual coherence. As expected, the deepest-going ray groups can be easily identified, arriving in groups near 137.8 and 72.3 secs in a) and b) respectively. Following this group are one or more other ray groups. Finally, there is a confused region of high energy but with no discernible pattern, ending abruptly. Bottom-reflecting energy can be seen in both plots during the fall, at 139.2 and 72.65 secs respectively. At later times these arrivals are obscured by the stronger near-surface energy.

The signal-to-noise ratio is noticeably lower in the long path (1-4) than in the short path (6-4), so that the array gain from beamforming on the receiver array is crucial to providing good results.

Examining figure 4-7, one can discern 4 different regimes of propagation: early fall (October-November), late fall (December-January), winter (February-April), and spring (May onwards).

Travel-time for the earliest rays varies by about 30ms over the year, whereas travel-times for the "last" ray can vary by almost 1s. The dotplots from July of 1989 are quite different from those of October 1988, implying either that we have not fully resolved the annual cycle or that significant interannual changes in the propagation conditions occur. Also note that while the cut-off of energy is usually quite sharp and easily visible, this is not the case during the late fall. Although this coincides with the period in which dense ice covers the array region, ray travel times are apparently not greatly affected by surface ice itself [*Jin et al.*, 1993]. However, there exists a shallow, cold mixed layer whose base is just above the source/receiver pair. This sound-speed profile causes significant frequency-dependent dispersion of the modal energy because the degree to which modes are trapped in the mixed layer can change drastically with frequency for modes whose turning depths are close to the mixed layer base, i.e. the lowest order modes. We refer the reader to *Sutton et al.* [1993] and *Jin et al.* [1994] for more details of propagation during the late fall and winter.

4.2.3 Spring transition

There is an interesting acoustical effect that occurs during the transition from the winter to the spring periods, clearly visible when waveforms are normalized in a specific way. Figure 4-8 shows a gray-scaled dotplot for the 1-4 path. Instead of plotting merely the peak locations, each sample in the received waveform is plotted as a gray-scaled pixel.

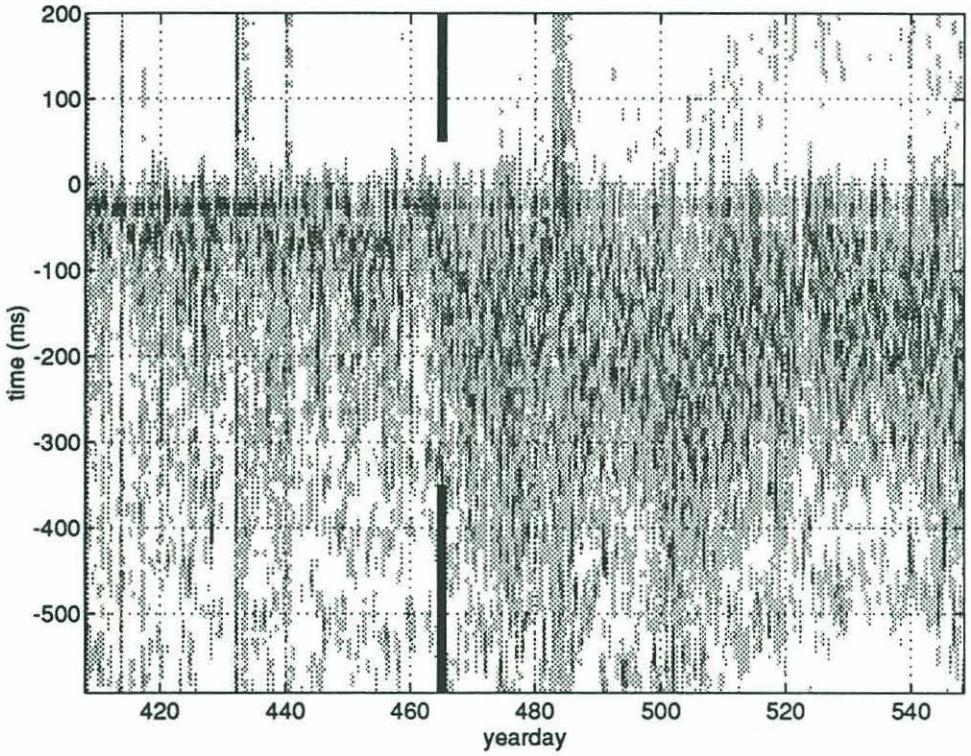

Figure 4-8: Gray-scaled normalized dotplot for path 1-4. This presentation is similar to that in figure 4-7, although here each waveform sample is represented by a gray-shaded pixel, with larger values having a darker colour. Each reception has been normalized by its maximum value, and aligned by the last peak (at -30ms on the y axis). Note the transition that appears near yearday 465 (marked by the vertical black bar). Before this time a last peak of width approximately 30ms is generally the largest, preceded by a somewhat smaller peak. After this time the last peak has been greatly reduced in relative amplitude, and maximum amplitudes occur in a broad region spanning the previous 300ms.

Furthermore, each reception is normalized by its maximum amplitude and aligned by the final arrival, which appears at about -30ms on the vertical axis. Before day 465 (April 9th 1989), the major feature of the arrival pattern is a narrow, concentrated final arrival peak of width no greater than some 30ms. Approximately 40 ms before this final peak is another peak which is generally much smaller. After day 465, the amplitude of the final arrival is much reduced, and maximum amplitudes occur in a broad region spanning the previous 300ms. Similar features can be seen in dotplots of other paths. We will now consider details of this feature as seen by the receiver on mooring 4 from all paths coming to that mooring.

This last part of the arrival pattern, which consists of acoustic energy propagating near the surface, is most efficiently described in terms of acoustical normal modes rather than rays. The final peak corresponds to the lowest order mode, and can usually be resolved in time. Earlier modes can sometimes be resolved in time, but in general there is significant interference between them. Since we are interested in the behavior of a large number of modes, we compute an incoherent (magnitude only) average performed across all hydrophones in order to provide some stability to the results. A simple cubic interpolation scheme was used to get an effective sample spacing of 2ms before averaging. For convenience, the period during days 410-465 (13 February to 9 April) will be called the winter, and the following period the spring.

Average winter arrival patterns for the 4 paths considered are shown in figure 4-9a. RMS amplitudes (in arbitrary units) have been multiplied by the square root of path range in order to remove cylindrical spreading effects, adjusted for the small differences in source level (a range of about 0.7 dB), and increased by .008 db/km to account for the attenuation due to boron relaxation at a temperature of 0°C [*Clay and Medwin*, 1977]. Time scales have also been normalized by range to adjust for mode dispersion (assuming that group velocities are uniform over the region), and the averaged waveforms horizontally aligned "by eye" to get the best agreement of peaks, so that modes of the same number appear at the same normalized time in all plots even though the actual time scales are different for each path. Mode 1 appears at 0.75, and mode 9 appears at roughly 0.5 on the normalized time axis. Since the width of modal arrival peaks is constant and their time separation will increase with range, this normalization will result in narrower peaks for longer paths. Thus mode 2 can be resolved in time in the 1-4 path, is almost seen in the 3-4 and 5-4 paths, but is not visible in the 6-4 path. The general agreement of the amplitudes in the early part of the

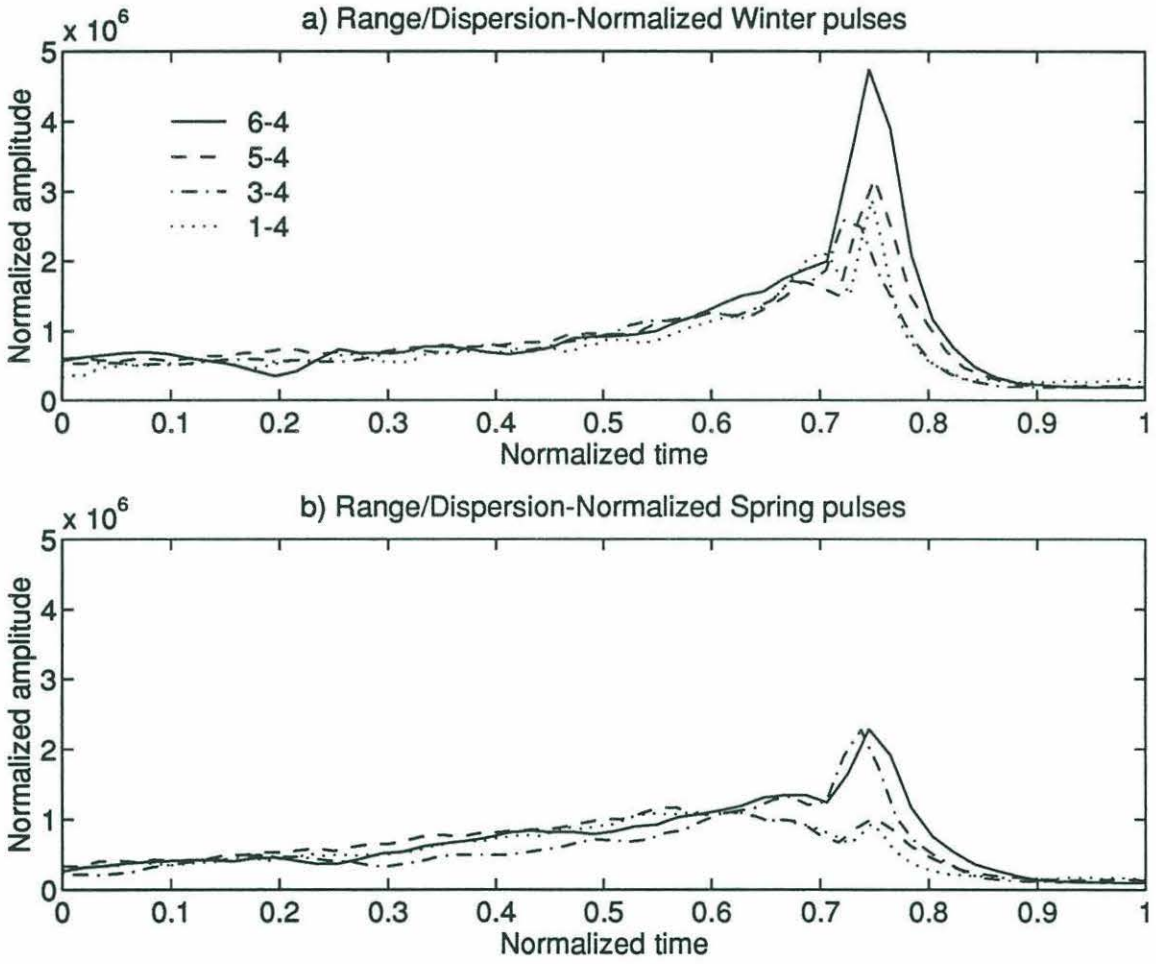

Figure 4-9: Average receptions for paths to mooring 4 in a) winter and b) spring periods. Waveforms have been normalized in amplitude and time-scale to remove all range effects and small differences in source levels.

waveforms suggests that the normalization has taken into account all relevant range effects.

The normalized amplitudes of modes along different paths will be affected by differences in the source depths, changes in the mean sound speed profile, and coupling losses due to variations in soundspeed along the different transmission paths. Energy coupled into other modes will arrive at other times. In particular, energy lost from the lowest order mode will always arrive earlier than the final peak. However energy coupled into the lowest order mode will not arrive as late as the original final mode peak. Thus mode coupling can only decrease the height of the final peak. The early part of the waveforms are composed of a large number of interfering modes, and coupling will not drastically change the energy levels there.

Source depths were similar for all sources, and the mean soundspeed field in the upper waters was also similar over the array region. Thus the amplitude differences are probably due to differences in soundspeed variability over the array region (and hence differences in coupling losses). Paths 1-4 and 5-4 travel through the northern part of the array which is heavily influenced by the dynamics of the nearby East Greenland Front. The northern part of the array (as well as the 3-4 path) is also covered by ice during the winter period. The 6-4 path has the largest final peak. This path is almost co-located with path 1-4 although with half the range, and (as will be shown in chapter 7) it traverses the region of deep mixing and remains almost completely ice-free during this period. Thus it probably has the most homogeneous upper waters. Since the temperature and hence the soundspeed field is most uniform here, we would expect to find the smallest coupling losses and largest final peak for transmissions along this path. Another possible explanation for the height of this peak is modal interference between 2 modes time-resolved in longer paths. If we assume that the phase relationship between the 2 modes is random between transmissions, then mode average powers (squares of RMS amplitude) add. This correction accounts for only about one third of the differences in peak amplitude between the 6-4 path and the other paths. As will be shown below, the actual amplitudes have a large variance, so that some of the remaining difference may simply be an artifact of the finite sample size used in the average.

Average spring waveforms for the 4 paths are shown in figure 4-9b, normalized as above and plotted on the same vertical scale. The average waveforms for 5-4 and 1-4 remain very similar to each other, although the winter and spring averages are quite different. The final peak is greatly diminished, to about 30% of its previous amplitude, but the earlier part of

the waveform is unchanged (for 5-4) or even a little higher (for 1-4). The 6-4 waveform shows a reduction of the peak amplitude to about 50% of its previous value, but is now very similar to the 3-4 waveform whose change is fairly small and undramatic. During this spring period the array is largely ice-free. Source and receiver depths remain unchanged. Mean soundspeed profiles change in the spring due to the growth of a warm mixed layer. This will effectively move the channel axis downwards towards the source depth. Ignoring coupling losses, this would result in a small increase in the amplitude of the final peak. Since this is contrary to the observations, we conclude that there must be an large increase in coupling losses. The greater changes seen to the north occur because the northern paths are closer to the dynamically active frontal region. Since warm and cold surface waters will be mixing there, the magnitude of soundspeed variability will be larger, increasing the coupling losses.

One final view of this phenomenon is shown in figure 4-10. Here we show time series of the last peak amplitude before any averaging, as well as net surface fluxes at 3 hourly intervals from analyses of the United Kingdom Meteorological Office (UKMO) Fine-mesh Operational Forecast model, more details of which are given in Chapter 6. Dotted bars indicate the mean amplitude and ± 1 standard deviation about this mean. One can see clearly a noticeable change in the acoustic behavior near day 465 in all paths except 3-4, and a concurrent change in the sign of the net surface fluxes. Amplitudes in the winter tend to have a large variance, which is greatest for the shortest path (6-4), consistent with coupling losses or modal interferences due to mesoscale soundspeed variability along the path. Over longer paths the average will be more stable than over shorter paths.

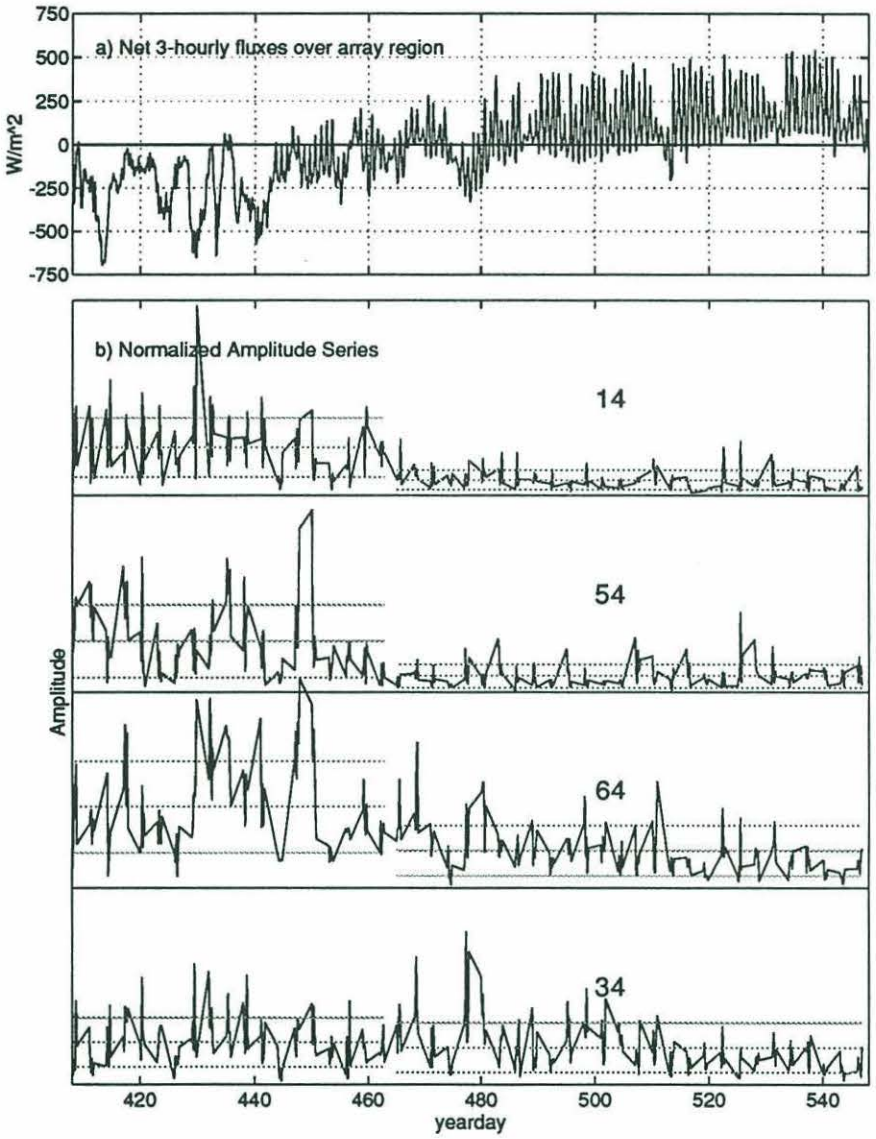

Figure 4-10: a) Net UKMO surface heat fluxes b) Amplitude of last peak for all 4 paths. Amplitudes have been normalized to remove range effects and small differences in source levels.

Chapter 5

Tomographic Inverses

5.1 Introduction

In this chapter we describe the computation and validation of tomographic slice inverses using observed eigenray travel-times to determine range-average heat content and temperature profiles. In the previous chapter general characteristics of acoustic propagation were discussed. We begin here by describing the generation of travel-time series for eigenrays and quantification of their errors. Next, we summarize mathematical aspects of the linear inverse procedure, and in particular the method by which estimates of the inverse error can be determined. To generate optimal results, *a priori* specifications of solution statistics are needed. These are stated and justified. A method for dealing with the sharp temperature gradients seen at the base of shallow cold mixed layers is described. These shallow cold mixed layers are very poorly resolved by the linear inverse. Other errors arising from acoustic interactions with surface ice, the soundspeed/temperature conversion, and higher-order terms in the perturbation expansion used to linearize the inverse problem are quantified and shown to be minimal in most cases. Finally we show some of the results, and verify their correctness by making limited comparisons with independent information. More detailed analysis of the results is deferred to chapter 7.

It should be emphasized that much of the previous theoretical and empirical experience with tomographic methods was based on observations and simulations of a mid-latitude deep sound channel. Many of the practical aspects of deriving tomographic inverses in a high-latitude surface ducted environment – some of which were quite new and hitherto unsuspected – were discovered during this analysis.

5.2 Eigenray Travel-time Series

Acoustic observations were discussed in the last chapter. From this data, ray travel-time series were computed for all paths. Different programs were used for data recorded by the WHOI/Webb receivers (moorings 4 and 5) and the SIO receivers (moorings 1 and 6). For the Webb receivers, data-windows were manually specified for each ray group using the dotplots. Windows were generally about 100ms wide for the first arrival, and narrower for later arrivals. However, the location of the window's center would vary as a function of geophysical time along a small number of user-specified line segments. A peak-picking program would then beamform the energy from all receiver elements to the nominal ray angle, searching for peak pairs separated by approximately the correct time interval by correlating with a pre-defined pulse replica. Once a peak pair had been located, parabolic interpolation was used to determine the ray arrival times and amplitudes. No tracking was done between receptions to remove the possibility that the tracking would drift. However, this sometimes resulted in the mis-identification of rays within the same group, especially when only one of the two rays arriving at the same angle actually appeared, and would also result in misidentifications which generated outliers when both rays failed to arrive. Quality control of the travel-time information, based on a combination of tests for peak signal-to-noise ratio (SNR) and amplitude comparison with other peaks in the data window, generally identified most of the outliers for subsequent processing.

Stable bottom-reflected arrivals were observed along most paths. These were not used in the inverses for several reasons. Their SNR was small (hence travel-time errors, especially those due to misidentification, were very large). There were some difficulties in resolving up- and down- arriving rays at high angles due to sidelobe aliasing in the receiver array. And finally, although bathymetry was measured along all tracks as part of the array deployment, successful prediction of the travel-time of these bottom-reflected rays occurred in only a few cases[1].

The last ray was tracked somewhat differently. In this case a threshold SNR was set (after some experimentation), and the last peak higher than this threshold in a coherent average across all hydrophones was selected. This guarded against the case when the largest peak did not correspond with the last arrival. A period when this occurs was discussed in

[1] although these rays *have* been used to estimate the bottom critical angle [*Lynch et al.*, 1993].

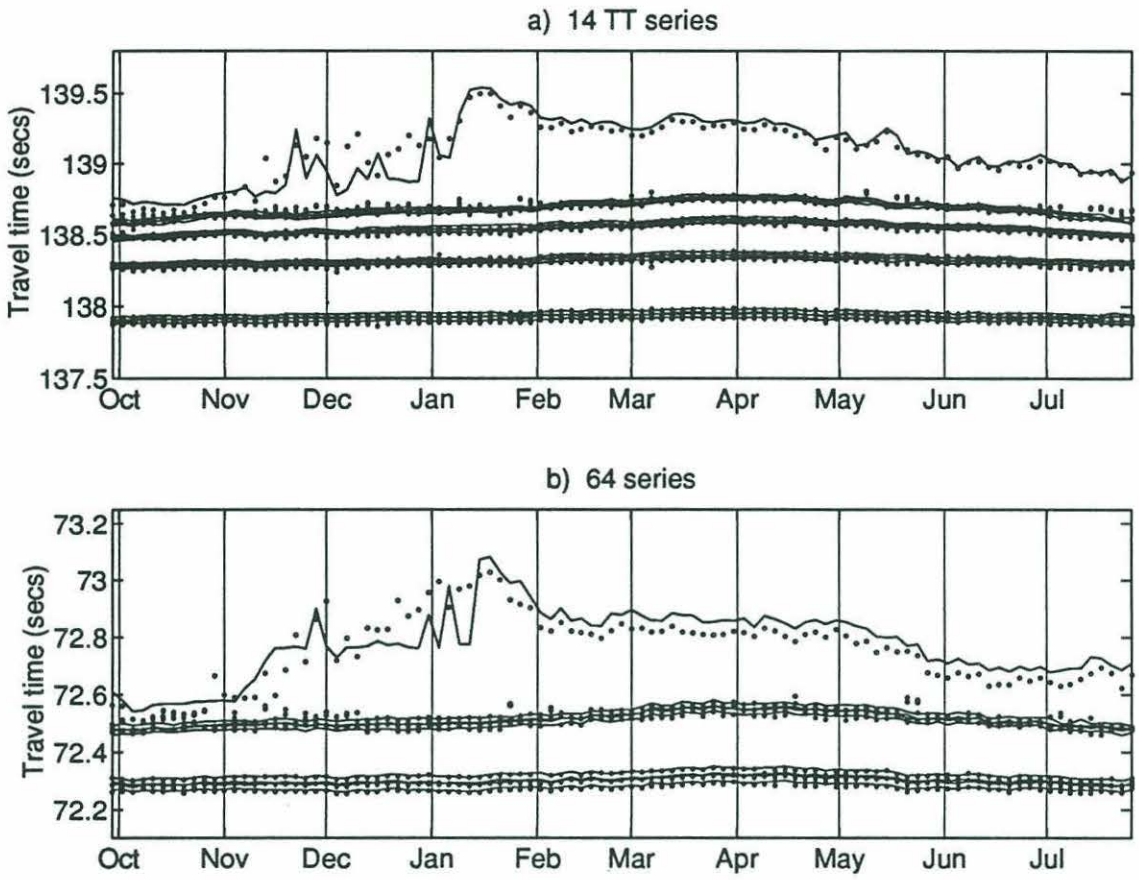

Figure 5-1: Travel-time series for a) long (1-4) and b) short (6-4) paths. Solid and dotted lines represent reciprocal series. Differences between reciprocal series are small (order 10ms) except for the last arrival during December and January. A small bias between the last arrival series at other times during the year is due to the use of different tracking algorithms and is not important for the inverses.

the previous chapter.

For the SIO receivers, a slightly more sophisticated algorithm was used. Correlations were performed in a 2-dimensional time-angle window, and some tracking was enabled. For these reasons, and also because these instruments had a sampling time of 4ms - double that of the Webb receivers - the resulting time series are qualitatively smoother. For comparison purposes one path was tracked using both programs. Resulting travel-time series were not significantly different (P. Worcester, pers. comm. 1992).

Travel times for all receptions in a given day were combined to form daily or 3-daily series (examples along two paths are shown in figure 5-1; compare with the dotplots of figure 4-7). This was done partly to remove tidal and inertial effects and improve the travel-time estimate, partly to overcome difficulties with erroneous/missing data, and partly to generate

regularly spaced time series. A median value was used to characterize one day's receptions because of its robustness with respect to outliers. Spectral analysis of the sum and difference time series indicated that features with periods of less than about 1-2 days were below a flat noise floor (except for tidal/inertial peaks in the difference series), so that not much information was lost in decimating the data in this way. On several occasions over long paths there were no good travel-times available during a day for a particular ray; time series were linearly interpolated over these gaps. Time series for reciprocal rays almost always agree within O(10ms). A notable exception is the last-peak series during December and January. During this period period frequency-dependent mode dispersion in the shallow cold near-surface mixed-layer causes problems with the ray paradigm [*Sutton et al.*, 1993; *Jin et al.*, 1994] and makes identification of a "last" ray more uncertain. The constant difference in reciprocal last-peak series seen during much of the year is due to a small difference in peak-tracking algorithms associated with the different instrument designs, and is not important in these inverses.

Travel-time observations for different rays are assumed to be independent (or at least uncorrelated). Standard errors for short paths are about ±3ms for the earliest ray arrivals and about ±15ms for the "last" ray, except during December/January when a value of ±200ms is considered more reasonable. For long paths the errors are about double this size. Errors are also in general slightly smaller for rays arriving at moorings 1 and 6 than for the reciprocal rays arriving at moorings 4 and 5. These short path values are about one-half those used in *Sutton et al.* [1993], and are roughly consistent with the level of a flat noise floor for periods less than about 1-2 days found in robust spectral estimates of the travel-times. They are thus estimates of the actual variability in travel-times, rather than estimates based on predictions about internal wave noise etc. Note that for two-way travel times clock errors are not important. For one-way travel-times these numbers will include the effects of short-term random errors in the mooring motion time series and clock corrections, but will not include the slowly varying bias (of order ±1 ms) remaining from the clock corrections described in Appendix A, which we assume are too small in relation to the other errors to have much effect on temperature inverses.

Since one expects purely instrumental errors to be similar for all rays, other effects must be important in producing this pattern of increasing error with increasing travel-time for a given path. In particular, later rays generally arrive closer together, and thus there is

a greater possibility of interference. Internal wave activity is probably also greater in the upper ocean, which would also increase variability in the later (and shallower) rays. Visual inspection of the travel-time series suggests that the stated errors are valid for the entire year after outliers have been removed.

The presence of surface ice can modify the travel-times of steeper rays. The travel-time changes induced by these effects are on the order of 1 ms [*Jin et al.*, 1993], and their effects on the inverse are discussed further in section 5.3.5.

An attempt was made to match the results of forward modelling with the observed travel-times using soundspeed profiles determined from the deployment CTD casts. At this point it was discovered that ranges based on the surveyed anchor locations were inconsistent with the data - in fact, the ranges seemed to be in error by up to several hundred meters. It is possible to estimate this error jointly with the sound-speed profiles in the inverse procedure. If the range error is small, making a "locally plane wave" assumption for the ray arrivals leads to an obvious extension to the linear inverse [*Cornuelle*, 1985]. Here we make the full (non-linear) correction by adjusting ranges so that the forward modelling predictions of travel-time and inverse estimates of temperature at deployment were consistent with observed values (see also section 5.3.5 below). Range adjustments were of order 200m, consistent with accuracy of LORAN-C, and are presumed to be accurate to within about 5m.

5.3 Range-Independent Slice Inverses

The simplest inverse to understand is the slice inverse - an inverse along a single mooring to mooring path. Computing slice inverses avoids the issue of differing biases along different paths due to range errors. The lower dimensionality of the problem also makes working with the results much easier. Range-dependent slice inverses are possible by exploiting the asymmetry in up- and down- going rays [*Howe et al.*, 1987]. However, the asymmetry is very weak here due to the source/receiver geometry. Range-independent slice inverses for range-average profiles, on the other hand, are relatively robust. It is also possible to easily plot the time evolution of the temperature profiles – again this is not necessarily a trivial issue when so much is unknown. Thus it was decided that range-independent slice inverses would be generated in this analysis. Combined ray/mode slice inverses to determine range-averaged

near-surface information during February/March for the 1-6 path have been generated by *Sutton et al.* [1993], and a fully 3-D inverse is being pursued by W. Morawitz (pers. comm. 1993).

The usual formulation of the inverse problem in terms of the ray paradigm is used here. Note that near-surface propagation is not really described by a single ray at all. Since it turns out that most of the variability (i.e. the temperature signal) occurs near the surface, some method must be used to deal with this problem. We have approximated the last arrival by a so-called "last" ray. Although such an approach is not strictly correct since the final peak is really due to the sum of a number of interfering rays, these rays all traverse approximately the same depth range of the water column and thus they contain little independent information. Also, as we shall show below, the smoothing inherent in the inverse tends to diminish the problem.

Inverse solutions generally proceed by estimating corrections to some background profile using a linear perturbation approach [*Munk and Wunsch*, 1979] although other methods are possible, e.g. the finite amplitude inverse using Abel transforms [*Munk and Wunsch*, 1983], or matched-field processing [*Tolstoy and Diachok*, 1991; *Tolstoy*, 1992; *Goncharov and Voronovich*, 1993]. As will be shown below, the lack of vertical resolution (especially near the surface), makes application of many sophisticated procedures somewhat pointless since they require much more information about the solution space than was known initially. Thus the linear inverse was used to produce consistent and useful solutions.

5.3.1 Linear inverse theory

A brief outline of the range-independent tomographic slice inverse problem formulation will be presented here. In general the travel-time T along some ray path Γ through a soundspeed field $c(x, z)$ can be represented by the path integral

$$T = \int_{\Gamma} \frac{ds}{c} \tag{5.1}$$

By Fermat's principle, small perturbations δc affect the travel time to first order only through the *argument* of the integral equation (5.1), and not through changes in the ray path Γ. The effect of path length changes are cancelled by the soundspeed changes along the perturbed paths, so that (to first order) we can consider the ray paths to be effectively

"frozen". This results in a considerable simplification since the perturbed integral equation is then approximately linear in the unknown soundspeed change δc:

$$T + \delta t \approx \int_\Gamma \frac{ds}{c + \delta c} \approx \int_\Gamma \frac{ds}{c} - \int_\Gamma \left(\frac{\delta c}{c}\right) \frac{ds}{c} \tag{5.2}$$

The perturbation part of this equation can be discretized by assuming constant range-independent soundspeed variations δc_i to the mean soundspeed c_i in adjoining depth bins $z_i < z < z_{i+1}$:

$$\delta t \approx -\sum_i \frac{\delta c_i}{c_i^2} ds_i \tag{5.3}$$

where the total length of the segments of the ray path Γ which lie in the ith depth bin is given by ds_i. More sophisticated discretizations in terms of modal expansions of the soundspeed perturbation are possible, but the main reason for using such expansions - efficiency in describing ocean processes - does not really apply here since we have very little idea as to what ocean processes must be included. The vertical discretization grid is chosen to be much finer than the resolution of the inverse (a 30m spacing was used between 0 and 3000m), so that (5.3) can be considered a finite difference approximation to the continuous perturbation part of (5.2) rather than a projection onto a finite set of modes, for example, the lowest order baroclinic modes of the shallow water equations.

We have neglected the effect of ocean currents in this derivation. Along-track currents result in an additional perturbation term in (5.2) whose effects can be exactly cancelled in principle by averaging travel-times for reciprocal transmissions. Since all transmissions in the array took place within an 8 minute window, non-reciprocal effects are minimized. In this experiment, the current effects on the travel-times are quite small, and there is little difference between inverses made with one-way and mean two-way travel-times.

By writing equations in the form of (5.3) for all rays, we form a linearized matrix equation (the "model")

$$\delta \mathbf{t} = \mathbf{A}\delta \mathbf{c} + \mathbf{n} \tag{5.4}$$

in which there are generally many more unknowns (elements δc_i of $\delta \mathbf{c}$) than there are observations (elements of $\delta \mathbf{t}$). An exact solution is not necessarily guaranteed, since there is no reason, *a priori*, to assume that travel-time observations are consistent with the model or even with each other to better than some measurement error $\mathbf{n}$. Higher order terms

neglected in the approximation (5.2) will also result in a misfit between the model and the observations. The importance of such terms can be determined by comparing the difference between observed ray travel-times and those computed for the inverse profiles with the *a priori* estimates of data errors. One can account for significant model misfit errors by artificially increasing $\mathbf{n}$; this is not done here. A number of different solution techniques for this type of problem have been used. Here we apply the singular value decomposition (SVD) approach of *Chiu et al.* [1987] to find solutions with the least mean square error, i.e. the optimal estimates of the Gauss-Markov Theorem. A summary of this method follows.

First, the system of equations (5.4) is transformed and normalized into a space of uncorrelated variables with unit variance to remove biases resulting from purely numerical effects (e.g. the dimensional units of the various parameters):

$$\delta\tilde{\mathbf{t}} = \tilde{\mathbf{A}}\delta\tilde{\mathbf{c}} + \tilde{\mathbf{n}} \tag{5.5}$$

where

$$\tilde{\mathbf{A}} = \mathbf{R}_{\mathbf{nn}}^{-1/2}\mathbf{A}\mathbf{R}_{\mathbf{cc}}^{1/2} \tag{5.6}$$

$$\delta\tilde{\mathbf{t}} = \mathbf{R}_{\mathbf{nn}}^{-1/2}\delta\mathbf{t} \tag{5.7}$$

$$\delta\tilde{\mathbf{n}} = \mathbf{R}_{\mathbf{nn}}^{-1/2}\delta\mathbf{n} \tag{5.8}$$

$$\delta\tilde{\mathbf{c}} = \mathbf{R}_{\mathbf{cc}}^{-1/2}\delta\mathbf{c} \tag{5.9}$$

A priori estimates of covariance matrices for the travel-time errors $\mathbf{R_{nn}}$ (discussed above) and for the soundspeed variations $\mathbf{R_{cc}}$ (discussed in the next section) are used in this transformation.

The singular value decomposition of $\tilde{\mathbf{A}}$ can be written as:

$$\tilde{\mathbf{A}} = \mathbf{U}\Lambda\mathbf{V}^{\mathbf{T}} \tag{5.10}$$

where Λ is a matrix whose diagonal elements are called the singular values λ_i, and $\mathbf{U}$ and $\mathbf{V}$ are matrices whose columns $\mathbf{u_i}$ and $\mathbf{v_i}$ are corresponding eigenvectors determined by the equations:

$$\tilde{\mathbf{A}}\mathbf{V} = \mathbf{U}\Lambda \qquad \tilde{\mathbf{A}}^{\mathbf{T}}\mathbf{U} = \mathbf{V}\Lambda \tag{5.11}$$

By convention the eigenvectors are normalized to have unit norm, i.e.

$$\mathbf{U^T U = I} \qquad \mathbf{V^T V = I} \tag{5.12}$$

Note that the dimensions of $\mathbf{U}$, $\mathbf{\Lambda}$, and $\mathbf{V}$ are not necessarily identical, and that $\mathbf{\Lambda}$ is not square. The λ_i are non-negative, and the number of non-zero λ_i are equivalent to the rank of $\tilde{\mathbf{A}}$ or alternatively the number of pieces of independent information in the problem. Formally we can write a solution to (5.5):

$$\delta\hat{\mathbf{c}} = (\mathbf{R_{cc}^{1/2}})\mathbf{V\Lambda^{-1}U^T}(\mathbf{R_{nn}^{-1/2}}\delta\mathbf{t}) \tag{5.13}$$

where it is understood that $\mathbf{\Lambda^{-1}}$ is a matrix whose diagonal elements are λ_i^{-1}. Problems arise when some of the singular values are zero (i.e. the problem is underdetermined), or are very close to zero[2]. Since the λ_i^2 are analogous to signal-to-noise ratios associated with the various eigenvectors, this is an indication that corresponding parts of the solution space are badly determined. In order to avoid the noise due to these badly determined components, we form instead the optimal Gauss-Markov estimate:

$$\delta\hat{\mathbf{c}} = (\mathbf{R_{cc}^{1/2}})\mathbf{V\Lambda}\left(\mathbf{I}+\mathbf{\Lambda^2}\right)^{-1}\mathbf{U^T}(\mathbf{R_{nn}^{-1/2}}\delta\mathbf{t}) \tag{5.14}$$

This tapering downweights those parts of solution with $\lambda_i^2 < 1$ and preserves those with $\lambda_i^2 > 1$. By substituting (5.4) and (5.10) into this solution, we can find a *resolution* matrix

$$\mathbf{R} = \mathbf{V\Lambda}\left(\mathbf{I}+\mathbf{\Lambda^2}\right)^{-1}\mathbf{\Lambda V^T} \tag{5.15}$$

which relates the actual perturbation $\delta\mathbf{c}$ to the expected value of the estimate $<\delta\hat{\mathbf{c}}>$. The ith row or column of $\mathbf{R}$ is the *resolution kernel* associated with a field perturbed only in the ith vertical box (although one should note that the actual data perturbations are governed by $\mathbf{R_{cc}}$ and that, in general, delta-function perturbations will not occur). Examination of the compactness and shape of these resolution kernels reveals the smoothing and accuracy inherent in the inverse.

[2]This is always the case in ocean acoustic tomography. In fact, the number of significantly non-zero λ_i is generally equivalent to the number of ray *groups* in the inverses computed here, rather than the number of rays, which is to be expected since ray paths within a group are very similar.

One advantage of linear inverse methods, other than their simplicity, is that estimates of the solution errors (called the solution uncertainty) can be made. In particular, the mean square error or total error of the solution can be written as

$$\mathbf{C}_e = < |\delta\hat{\mathbf{c}} - \delta\mathbf{c}|^2 > = \mathbf{R}_{\mathbf{cc}}^{1/2}(\mathbf{I} - \mathbf{R})\mathbf{R}_{\mathbf{cc}}^{1/2}. \tag{5.16}$$

Notice that as the resolution gets better ($\mathbf{R} \rightarrow \mathbf{I}$), the uncertainty will decrease. However, the total error of the solution will be similar to the *a priori* estimates in regions where there is no resolution ($\mathbf{R} \rightarrow \mathbf{0}$). We can separate the total uncertainty into two independent terms: a bias component $<\delta\hat{\mathbf{c}}> - \delta\mathbf{c}$ arising from the inherent resolution problems due to the finite number of rays, and a random component $\delta\hat{\mathbf{c}} - <\delta\hat{\mathbf{c}}>$ due to noise in the observations. The covariance of the random component is written

$$\mathbf{C}_{\delta\mathbf{c}} = < |\delta\hat{\mathbf{c}} - <\delta\hat{\mathbf{c}}>|^2 > = \mathbf{R}_{\mathbf{cc}}^{1/2}(\mathbf{V}(\mathbf{I} + \mathbf{\Lambda}^2)^{-1}\mathbf{\Lambda}^2(\mathbf{I} + \mathbf{\Lambda}^2)^{-1}\mathbf{V}^{\mathbf{T}})\mathbf{R}_{\mathbf{cc}}^{1/2}. \tag{5.17}$$

Usually when plotting results, the error bars shown are the diagonal elements of the uncertainty matrices. However, these are conservative estimates that ignore the effects of vertical correlations in the data.

In this thesis we shall generally speak of temperature and sound-speed interchangeably, since sound-speed changes are primarily temperature dependent within the ranges of temperature and salinity observed in this region. Specifically we will use the approximation

$$\begin{aligned} \delta\mathbf{c} &= \frac{\partial \mathbf{c}}{\partial T} \cdot \delta\mathbf{T} + \frac{\partial \mathbf{c}}{\partial S} \cdot \delta\mathbf{S} \\ &\approx 4.6 \cdot \delta\mathbf{T} \text{ ms}^{-1}\,^{\circ}\text{C}^{-1} \end{aligned} \tag{5.18}$$

By adding the temperature perturbations to the background profile, we form temperature profiles, which are converted to potential temperature Θ using a background salinity profile. In practise this amounts to little more than the addition of a depth-dependent offset $\chi(z)$:

$$\hat{\mathbf{\Theta}} = \delta\hat{\mathbf{T}} + \mathbf{T}_{\mathbf{background}} + \chi(\mathbf{z}) \tag{5.19}$$

The approximation (5.18) will be discussed at greater length in section 5.3.5 below.

Finally, we form heat content estimates by vertically integrating potential temperature

profiles to a depth close to the bottom and below which the temperature is assumed to remain constant, chosen here to be 3000m:

$$\hat{\mathbf{H}} = \int_0^{3000} \rho c_p \hat{\mathbf{\Theta}}(z) dz \approx \rho_0 c_p \sum_i \hat{\mathbf{\Theta}}(z_i) dz_i \tag{5.20}$$

The mean square error of this estimate can be found using (5.16-5.19):

$$\begin{aligned} \mathbf{C}_{\hat{\mathbf{H}}} &= < |\hat{\mathbf{H}} - \mathbf{H}|^2 > \\ &= (\rho_0 c_p dz/4.6)^2 < |\sum_i (\delta\hat{\mathbf{c}}_i - \delta\mathbf{c}_i)|^2 > \\ &= (\rho_0 c_p dz/4.6)^2 \sum_i \sum_j \mathbf{C}_\varepsilon(i,j) \end{aligned} \tag{5.21}$$

where we have assumed that $dz_i = dz$ is constant for simplicity. That is, the heat content uncertainty is equivalent to a double integral over the temperature uncertainty. If the mean square error of the inverse sound-speed profiles C_ε is diagonal, the heat content error is equivalent to the sum of uncorrelated errors with depth (i.e. a sum of squares), whereas if the errors are all perfectly correlated (i.e. $C_\varepsilon = \mathbf{s}\mathbf{s}^\mathbf{T}$ for some $\mathbf{s}$) the heat content error is equivalent to the square of the sum of the errors. Usually the structure of the errors will fall somewhere between these two extremes.

5.3.2 Background profile

For simplicity, the same background profile was used for all paths and for the whole year. Using the same background profile speeds up the inverse procedure immensely, since forward modelling through the background environment has to be done only once per path, and sensitivity analyses are carried out only once for each nominal path length. The gyre center of the Greenland Sea is characterized by very weak vertical stratification. There exists a surface mixed layer whose depth is about 50m and whose temperature is about 4°C by early September, but which cools to the freezing point (−1.8°C) and deepens somewhat during the winter (see chapter 3). Underneath the mixed layer from depths of 100-400m lies warmer more saline Arctic Intermediate Water (AIW) with temperatures in the range −1°C to 0°C (see figures 3-7 and 5-2). The AIW is very visible in fall profiles, but seems to disappear in March profiles. Below the AIW is a slight temperature minimum of −1.08°C at about 1500m. At depths of approximately 2000-3000m the *in-situ* – rather than potential

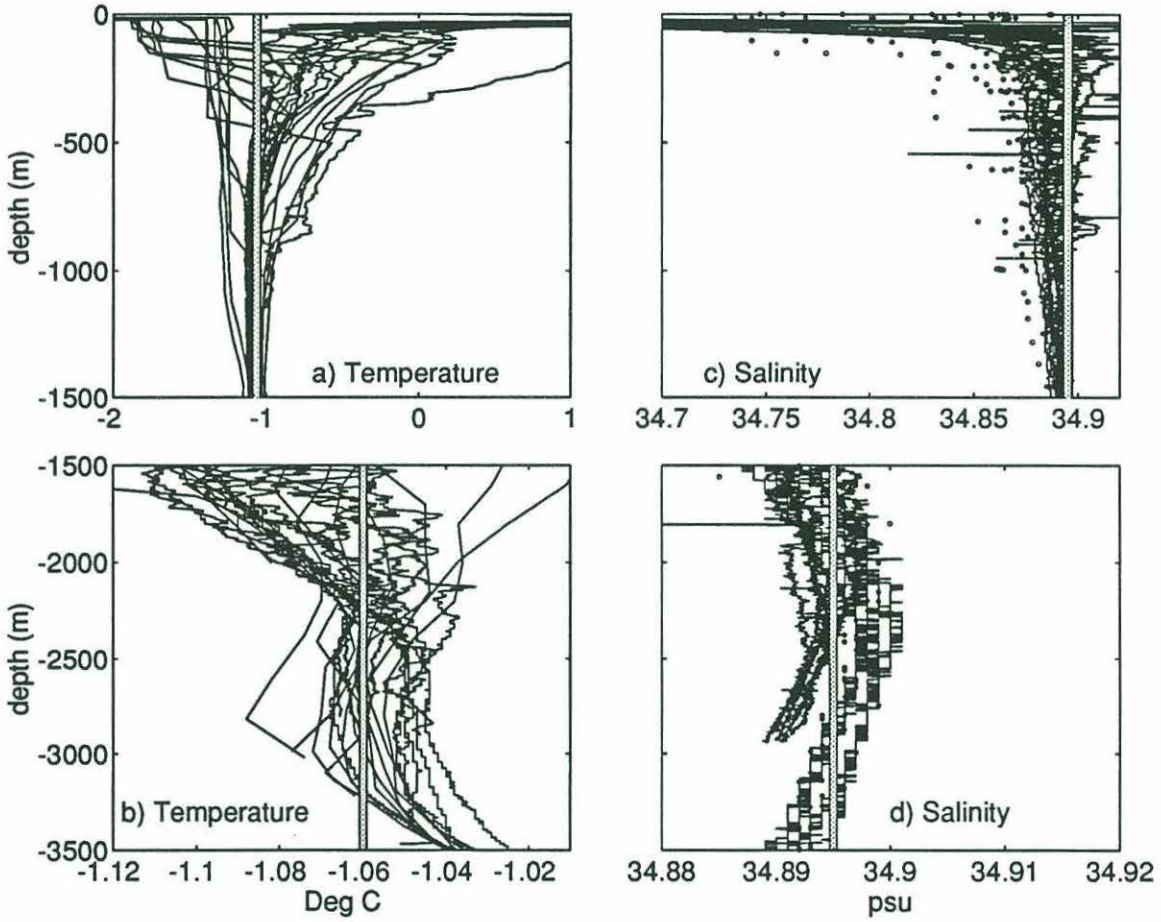

Figure 5-2: Background profile superimposed on CTD and Nansen bottle casts data taken during 9/88, 2/89, and 9/89 representing the hydrographic extremes. a) Temperature profiles in near the surface show most variability, but b) are fairly constant below 1500m. c) Salinity variations are greatest in the upper 100m, although small changes can be seen down to at least 1000m in winter. d) Deep salinity profiles show a slight maximum.

– temperature remains curiously constant, at about $-1.06°C$. This interesting phenomenon was also remarked on by *Bourke et al.* [1993]. Below 3000m, *in-situ* temperature increases slightly.

Salinity is generally low very near the surface (figure 5-2), and almost constant below 500m at a value of 34.895 (actually there seems to be a slight maximum at depths of 2500m; see also the discussion in *Aagaard et al.* [1985]).

The background profile was thus chosen to have a constant *in-situ* temperature of $-1.06°C$ to match the actual temperature profiles below 2000m, and a constant salinity of 34.895 psu (see figure 5-2). Above 2000m the choice of profile is not critical, as long as surface temperatures lie somewhere between $-1.8°$ and $4°C$. Figure 5-2 also shows that the temperature observations at depths of greater than 2000m have a scatter of some $\pm 0.01°C$ which is presumed to be due to instrumental biases and should be kept in mind when comparisons with inverse profiles are made. The background sound-speed profile is then calculated using the Del Grosso algorithm [*Del Grosso*, 1974], and is an almost linear function of depth.

When iterations of the inverse were performed, the new background profile was determined by averaging the original inverse profiles over roughly monthly intervals.

5.3.3 Model covariances and Inverse Uncertainty

It is in principle possible to estimate the model covariance matrix $\mathbf{R_{cc}}$ from actual data. However it is difficult to both estimate the errors in such a sample covariance matrix, especially one based on the somewhat sparse information available, and to determine the inverse sensitivity to these errors. Thus a simple analytic form was chosen for the covariance matrix, both to allow better control and understanding of the sensitivity of the result and because it was not clear that the "more sophisticated" approach would be any better. The depth dependence of sound speed variance was chosen to follow the simple exponential decay that seemed to characterize the available observations (see figure 5-3):

$$\sqrt{<\mid \delta c(z_i) \mid^2>} = \sigma_{ii} = \sigma_o \exp(-z/L_o) + M(z) \tag{5.22}$$

where $\sigma_o = 5$ m/s and $L_o = 450$m were chosen to match the profiles over the whole year, and $\sigma_o = 3$ m/s and $L_o = 600$ where chosen for detailed views of the deep mixing period.

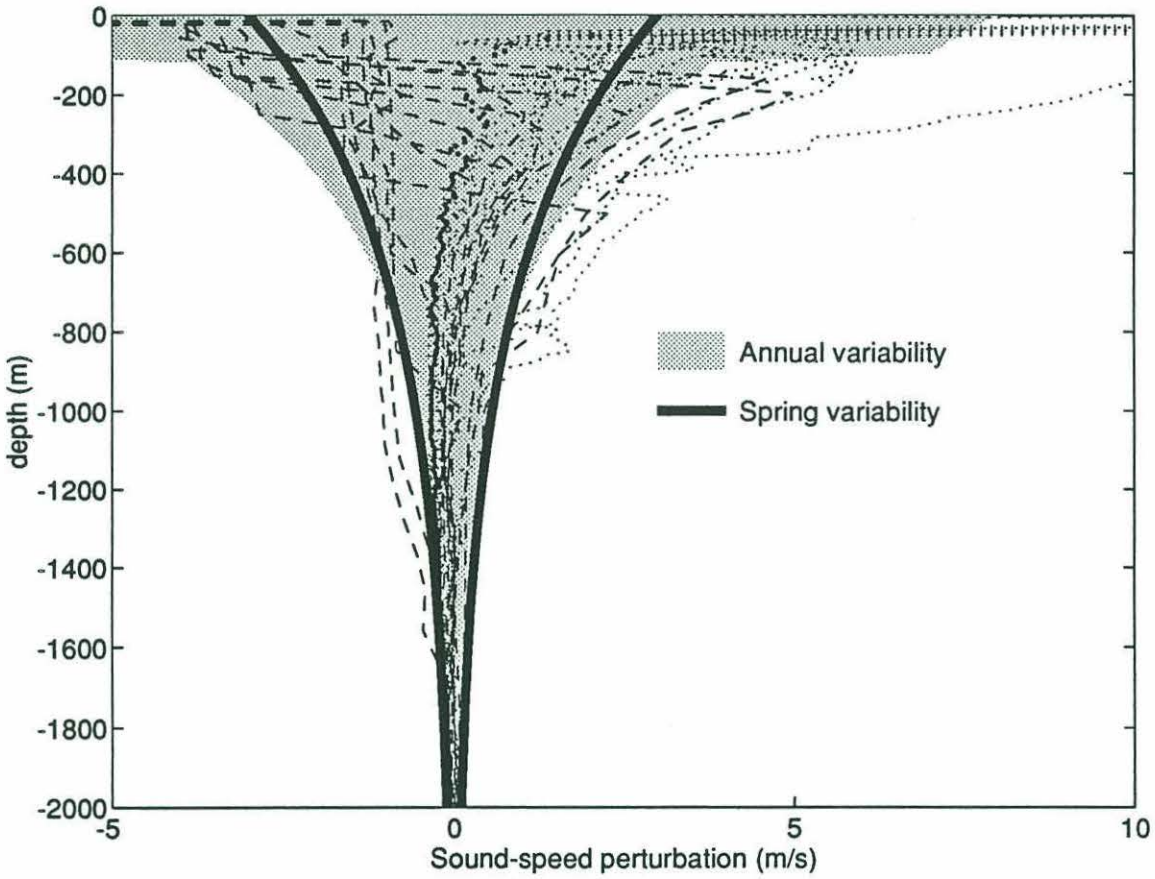

Figure 5-3: Depth dependence of soundspeed variance. Available T,S profiles were converted to soundspeed and the background profile subtracted to give perturbation profiles shown by dotted lines (fall) and dashed lines (winter). Parameters of the exponentially decaying variance were chosen as shown.

This has the effect of reducing variance near the surface but leaving it almost unchanged below 500m. $M(z)$ is a function used to parametrize the highly variable mixed-layer; it is set to 3 m/s for depths $\leq$ 100m for inverses during the fall and summer. The covariances were set according to

$$< \delta c(z_i)\delta c(z_j) >= \sigma_{ii}\sigma_{jj} \exp(-(\Delta z/\bar{L})^2) \tag{5.23}$$

where $\Delta z = z_i - z_j$, and $\bar{L} = (L(z_i) + L(z_j))/2$. The covariance length scale (or equivalently the smoothing scale) L was set in a number of ways. Solutions were not particularly sensitive to the choice as long as L was greater than several hundred meters, implying that the inverse pictures are indeed data-driven. However, the structure of the inverse error estimates *are* quite sensitive to the choice of L. Soundspeed errors increase by a factor of almost 10 as L decreases from 2000m to 500m, although heat content errors change by only a factor of 3 since the increase in error at a particular depth is matched by a decrease in the vertical correlation of these errors. When producing time series covering the entire year, we use $L = 1500 - 1450\exp\{-z/800\}$m. However, during February and March, the inverses show that temperature perturbations are smaller and are apparently of larger vertical extent, so for detailed analysis during this period, we use $L = 1500 - 1100\exp\{-z/800\}$m. It should be emphasized that the major features of the solutions are rather insensitive to this change, although error estimates are greatly reduced. Estimated uncertainty is shown in figure 5-4a for a short path. During most of the year the total (random) uncertainties are almost ± 1°C (± 0.5°C) in the upper 60m, about ± 0.2°C (± 0.07°C) from 60-400m, ± 0.05°C (± 0.02°C) from 400-1200m, and ± 0.02°C (± 0.015°C) at 1500m. During February to April the bias is small, and total and random errors are almost the same. Note that the uncertainties are correlated vertically; this is not shown here. In fact, although uncertainties are smaller in the spring period they are more correlated vertically, and it turns out the the heat content uncertainty is approximately 10×10^7 Jm^{-2} at all times. Since the observational errors are larger for longer ranges, it turns out that the structure and size of error estimates for longer paths is very similar.

To investigate the smoothing inherent in the inverse, which is related to the depth error for a particular isotherm, we examine the resolution kernels (see figures 5-4b and c). The kernels are in general well localized with the median of the kernel coinciding with the depth

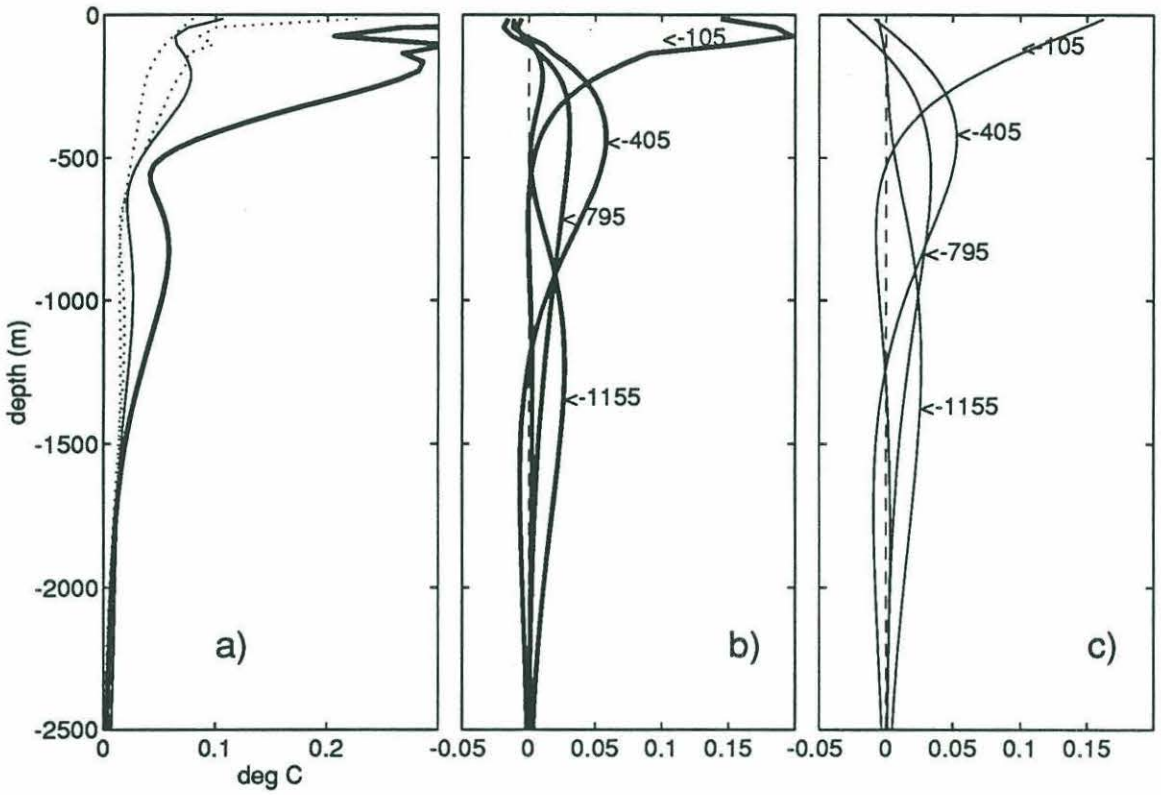

Figure 5-4: Uncertainty and resolution kernels. a) Root Mean Square Error estimates for the inverses during the February/April period (thin line) and during the rest of the year (thick line). The random component is indicated by dotted lines, and is similar in both cases. During the deep mixing period the error is mostly due to observational error, during the rest of the year inverse bias is significant. b) Resolution kernels of the inverse at selected depths for most of the year, and c) during Feb/Mar. Curve labels are located at kernel median points (arrows). These estimates are for a short path, those for longer paths are very similar.

of the perturbation over the range 0-1500m, although the mode is too shallow for depths of 500 to 1500m, and the mean too deep (by up to 200m) over the same depth range. Simulations show that isotherm depths can be in error by order 200m for profiles similar to those observed during February-March, but that this error is a smooth function of depth, i.e. small *relative* changes in isotherm depths are more accurately determined.

When iterations are performed, the variance terms are sometimes reduced, but in magnitude only. The decay scale L_o and the correlation structure as determined by L are not changed. Iteration changes the structure of the errors in small ways but broadly speaking they remain similar to those shown in figure 5-4a.

5.3.4 Corrections during ice-covered period

During December and January a cold shallow mixed layer covers the array region. Although the inverses show this feature, the smoothed nature of the inverse tends to average out sharp gradients, resulting in a spurious warming at intermediate depths (this was also found in simulations). On the other hand, the heat content (i.e. the *mean* temperature), is a relatively robust measurement as along as travel-times can be determined.

It is possible to restate the inverse problem from first principles in such a way as to account for this shortcoming but the extremely uncertain quality of the last ray travel-time series during this time make such an investment difficult to justify. Even if the last ray travel-time was more accurate, the small number of rays make it impossible to generate profiles as correct as those that occur at other times during the year. During the fall and summer, the last ray travels underneath the mixed-layer and hence the mixed-layer depth can be found through iteration, whereas last ray paths are quite insensitive to the mixed-layer depth in December/January. In fact, it is shown in *Sutton et al.* [1993] that the final ray travel time tends to ignore the cold mixed-layer while it is shallower than the source/receiver depth. Inverses with a number of different correlation structures and background profiles were performed and iterated until convergence had occurred, but the resulting profiles had little in common other than a colder surface layer with warmer water underneath.

Instead we shall use the robustness of the heat content to fit a temperature profile with one free parameter - the depth of the mixed layer. Figure 5-5 shows the model used. The background profile is representative of those seen in bottle casts at the end of November. This model is applied to heat content estimates during December and January in all inverses. Actual mixed-layer depths are not correct because the heat content estimates on which this procedure is based have errors, because the mixed-layer temperature is not known exactly, and because the deeper waters may in fact be warming slightly at this time (increases in the temperature of the AIW can be seen in the thermistor data of *Schott et al.* [1993], and as will be shown in Chapter 7 the heat content curves also imply a warming). For actual data, a smooth transition with the original inverses at the beginning of December and the beginning of February is made by using a tapered weighting function.

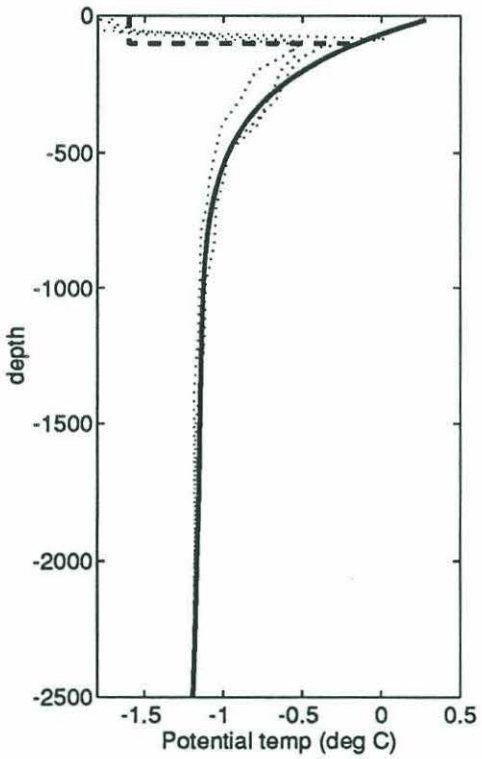

Figure 5-5: One-parameter model used to form temperature profiles in December and January. The background profile (thick solid line) is similar to profiles observed at the end of November (dotted lines). In order to match heat content with the observations, the depth of a mixed layer with temperatures near the freezing point (dashed line) is varied.

5.3.5 Nonlinearity and Other Errors

The inverse procedure outlined above is capable of estimating errors in the solution based on the *a priori* estimates of errors in the input variables and the assumptions of the model. If the model is incorrect, then the error estimates will be flawed, so that one must test for consistency with the assumed *a priori* statistics. A first test is to retrace rays through the inverse profiles, and compare their travel-times with the observations. If the travel-time differences between the data and retraced rays (the residual errors) are consistent with the assumed data errors, we have a consistent solution (although not necessarily a *correct* one). A full analysis was carried out for several paths, and the results extrapolated to all paths. In general a linear inverse resulted in consistent solutions for the deep rays at all times. The "last" ray was consistent with the obervations during the deep mixing phase (i.e. February-May), during December and January (recall that the assumed errors were extremely large during this time), and was marginally consistent in the summer (June and July). During fall (October and November) the retraced last ray for short paths was about 50ms later than the observations. A single iteration was enough to generate a fully consistent solution during the fall and summer for short paths, but 2 or 3 iterations were needed in the long paths before solutions converged. In the iterated inverse, the last ray, which reflected from the surface in the original background profile (similar to that shown in figures 4-4b and 4-5b) becomes trapped underneath the surface mixed-layer (see figures 4-4a and 4-5a). Iteration changes the temperature profiles very little (in fact, even the greatest changes during the fall are within a factor of 2 of the estimated uncertainty). Thus although the details of the profiles change slightly, the basic results are unchanged. Iteration did not significantly reduce the residual errors in the deeper rays. It is important to note that the residual errors in the last ray can probably be reduced to zero by repeated iteration since this ray is largely independent of the other rays, whereas errors in the travel-times for deeper rays will appear as irreduceable inconsistencies in the model equations.

Heat content time series remained essentially unchanged by the iteration, which just redistributes heat over the water column. The heat content is most influenced by the deeper rays which average the entire water column, and is only marginally affected by the last ray. Thus for heat content computations, iteration is not necessary.

However, we are not interested in travel-times as such, nor even in sound-speed – the product of the inverse – rather we would like to observe temperature. Although the two are

approximately related (cf. equation 5.18), salinity effects exist. Figure 5-6 shows contours of soundspeed perturbation as a function of salinity and temperature near the surface and at 1500m. In both cases the sensitivity is almost identical. Isovelocity contours are almost horizontal, indicating that salinity effects will be small. The most extreme temperature errors will occur in the fall. In the fresh water that exists in the mixed-layer at this time, warm temperatures in the upper 50m can be underestimated by (5.18) by as much as 0.25°C, giving a cold heat content bias of about 5×10^7 Jm^{-2}. However, the salinity dependency of soundspeed is almost linear, and so in terms of relative heat content changes throughout the year it is the changes in the salinity averaged over the water column that are important. From figure 3-8 we can deduce that the maximum change will be less than two thirds this value, i.e. the bias will vary from about 2×10^7 to 5×10^7 Jm^{-2}, implying a seasonal uncertainty of $\pm 1.5 \times 10^7$ Jm^{-2}. Since the surface waters at mooring 6 were least fresh in the fall compared with the other moorings, the bias is probably even smaller for paths through the center of the array. This value is about 6 times smaller than the inverse estimated uncertainty.

A surface ice cover can affect travel-times for deeper rays in two ways: first, the level at which the reflection occurs moves below the surface to the base of the ice, thus decreasing the path length. Secondly, acoustic beam displacements and time delays can occur during the reflection. However the exact characteristics of the ice (draft and acoustic shear and compressional wave speeds) on which these effects depend are unknown. Further problems arise since we do not know the exact geometry of the ice field; at most a statistical representation is available. An exhaustive analysis was carried out by *Jin et al.* [1993] over a number of cases presumed to cover all possibilities.

When shear velocities in the ice are greater than the soundspeed in water, total internal reflection occurs and travel-times decrease. However, in the opposite case acoustic energy can penetrate into the ice, and significant energy losses and increases in travel-time can result especially at ice thicknesses for which resonance conditions occur. However, very low shear speeds are generally associated with newly-formed keels and it is unlikely that these will be found in the central Greenland Sea. For path distances typical of the tomography array, the travel-time changes are of the order of 1 ms for ice thicknesses less than 1 meter. This bias is well below the travel-time uncertainties, and hence has little effect on temperature inverses. Although the changes are positively correlated across all rays and hence may

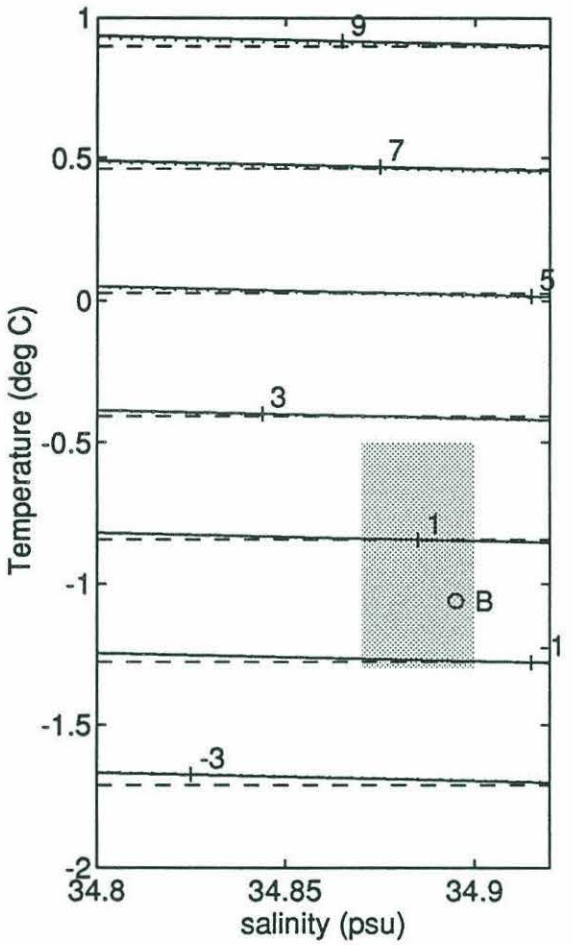

Figure 5-6: Errors in the conversion of soundspeed to temperature. Contours of soundspeed velocity as a function of temperature and salinity are shown for the surface (solid lines), at 1500m (dotted lines) and using the approximation (5.18) (dashed lines). Vertical bars near numerical labels indicate inverse-estimated errors. The background profile is indicated by the circle labelled "B". The shaded square indicates the range of T,S observed at 500m. Errors are greatest for the fresh surface water (of the same order as the inverse estimated errors), but are negligible below 500m.

have a greater effect on heat content, simulations extending the results shown in *Jin et al.* [1993] show that the resulting bias is probably somewhat less than that predicted by the inverse. We will therefore ignore this effect.

Although range-independent inverses can determine the exact range-average profile to first order, they can suffer from biases in comparison to the actual range average due to quadratic effects of range variations. [*Mercer and Booker*, 1983; *Munk and Wunsch*, 1985; *Munk and Wunsch*, 1987]. This is of greatest importance during the February/March, where (as we shall show in Chapter 7) the tomographic result is an average though a large number of plumes. However, simulations showed that travel-times through a soundspeed field with large wavenumber variations typical of the plume structures presumed to exist were almost exactly the same as travel-times through the mean field (differences were somewhat less than 1 ms) so this effect is also assumed to be negligible.

5.4 Some Results

Inverses for some paths are shown in figures 5-7 and 5-8, along with time series of ice concentration above each endpoint (a discussion of the ice concentration estimates follows in Chapter 6) and a comparison of inverse temperatures with thermistor records at a depth of 95m. The 6-4 and 1-5 paths are shown and described in greater detail in Chapter 7. Inverses have been slightly smoothed in time using a 3 point filter with relative weights of 1-4-1 giving a 3dB point 0.09 cpd. The period during which the one-parameter fit to heat content has been made is indicated by hatching. It is useful to compare these results with the monthly climatology in figure 3-7a.

First we show the 1-4 path (figure 5-7), which cuts through the center of the gyre. The temperature evolution here is quite smooth - no large temperature fluctuations are evident. The warm fall mixed-layer slowly cools, and possibly slowly deepens during the winter (due to resolution problems at this time the details are not clear). During March the mixed-layer deepens to perhaps 1000m in the range average. Finally, April-June is marked by variability at intermediate depths, probably the result of inflowing AIW replacing the products of winter cooling. Comparison with thermistor data is good.

Figure 5-8 shows the 4-5 path. This path is somewhat similar to the 1-4 path, but the mixed layer deepens to only about 700m or so. At mooring 5 the thermistor observations

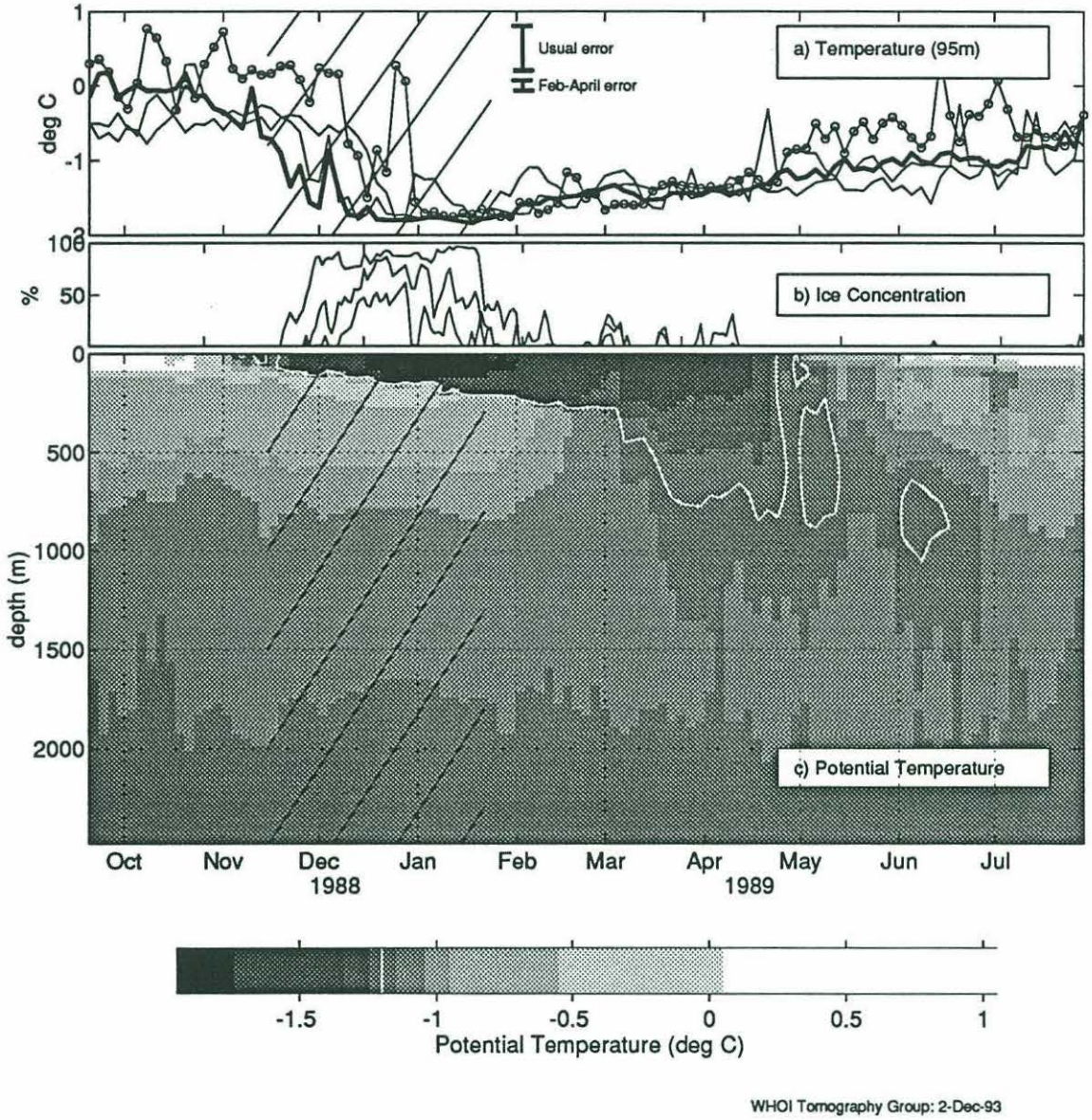

Figure 5-7: Temperature Inverse for 1-4 path. a) Comparison with thermistors at 95m (tomographic estimate is thick line) b) Ice concentration at endpoint moorings c) Potential temperature profiles. Hatched region is of uncertain quality, although consistent with the travel-time data. The white line marks the -1.2°C contour.

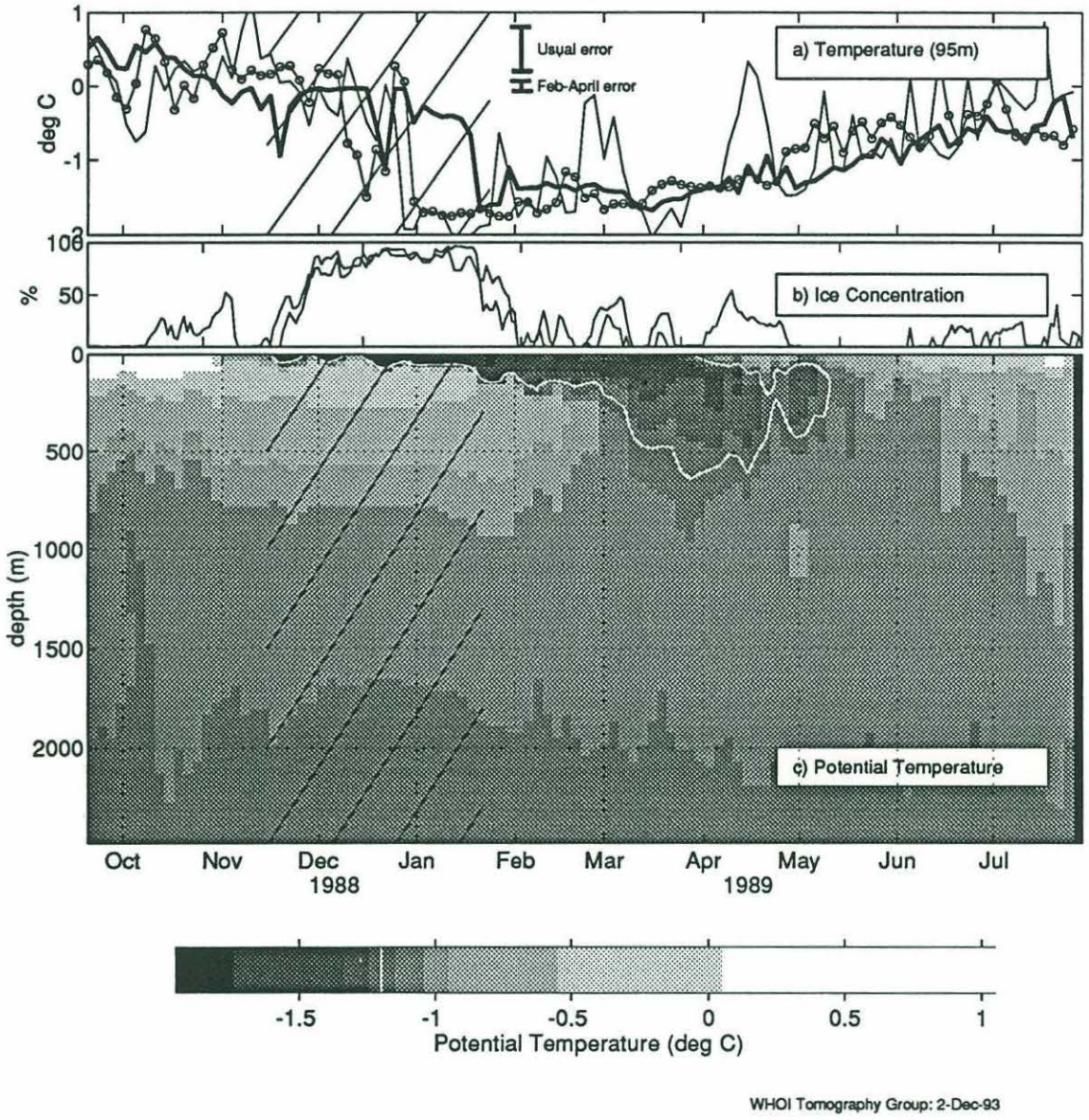

Figure 5-8: Temperature Inverse for 4-5 path. a) Comparison with thermistors at 95m (tomographic estimate is thick line) b) Ice concentration at endpoint moorings c) Potential temperature profiles. Hatched region is of uncertain quality, although consistent with the travel-time data. The white line marks the $-1.2°C$ contour.

show large fluctuations at the beginning of March and in April. The warm event in April barely appears in the inverse; the March event may appear as a warm anomaly superimposed on a linear cooling at this time (so that its presence is marked by the sudden temperature drop near March 7th). Again, comparisons with thermistor records are good.

It is instructive to compare some of the tomographic profiles with CTD observations. During the deployment of the tomography array, CTD stations were occupied near each mooring [*Bader et al.*, 1991]. These have been used to adjust the range error, both through forward modelling and inverse comparison. During February and early March, a number of bottle of bottle casts were made in and around the Gyre Center by the R/V Valdivia (J. Swift, pers. comm. 1991), and in the middle of March a comprehensive series of CTD casts and SeaSoar tracks along some of the paths were made as part of SIZEX (O. Johannessen, pers. comm. 1991). Figure 5-9 shows a comparison of profiles from the 6-4 path. The inverse profile from the beginning of the experiment compares well the deployment profiles. The iteration of the inverse at this time "cools" the intermediate waters and "warms" the surface mixed-layer. Also shown is a comparison with SIZEX profiles from the eastern half of the 6-4 path on the 16th of March 1989 and a bottle cast taken near mooring 4 on the 3rd of March. The mixed-layer base on this cast is near 600m, in good agreement with that shown by the 4-5 inverse at this time (figure 5-7). The dot-dashed line shows a bottle cast taken along the 3-4 path. Note the large amount of warm AIW and the much colder mixed-layer in this profiles, which is fairly typical for those near moorings other than 4 and 6 and for the periphery of the array region.

Although the 6-4 path seems to show little range dependence, this is not true for other paths that cross the center of the array. Figure 5-10 shows similar comparisons made with the 1-4 path. At deployment the range variation is not too severe, but in March we see profiles at mooring 1 with a very cold shallow mixed-layer above warm AIW as well as the deeply convecting profiles near the 6-4 path. The range average does appear to be accurately determined.

Heat content calculations are discussed in Chapter 7.

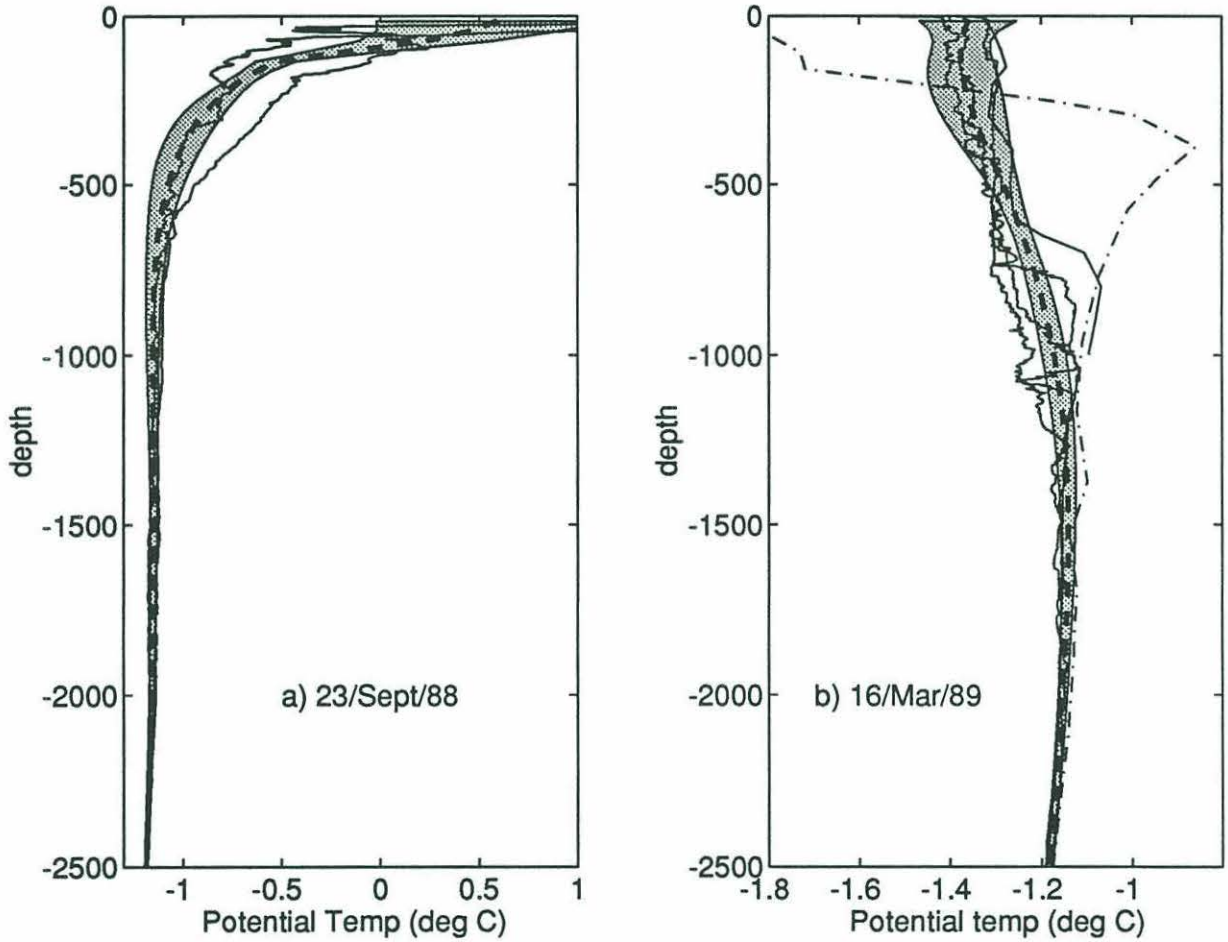

Figure 5-9: Comparison of point profiles with inverse profiles for the 6-4 path. a) At deployment. b) during the deep mixing period. Dot-dashed curve is a profile typical of those found near moorings 1, 3, and 5, and at other point at the periphery of the array region. Shaded region indicates inverse uncertainty.

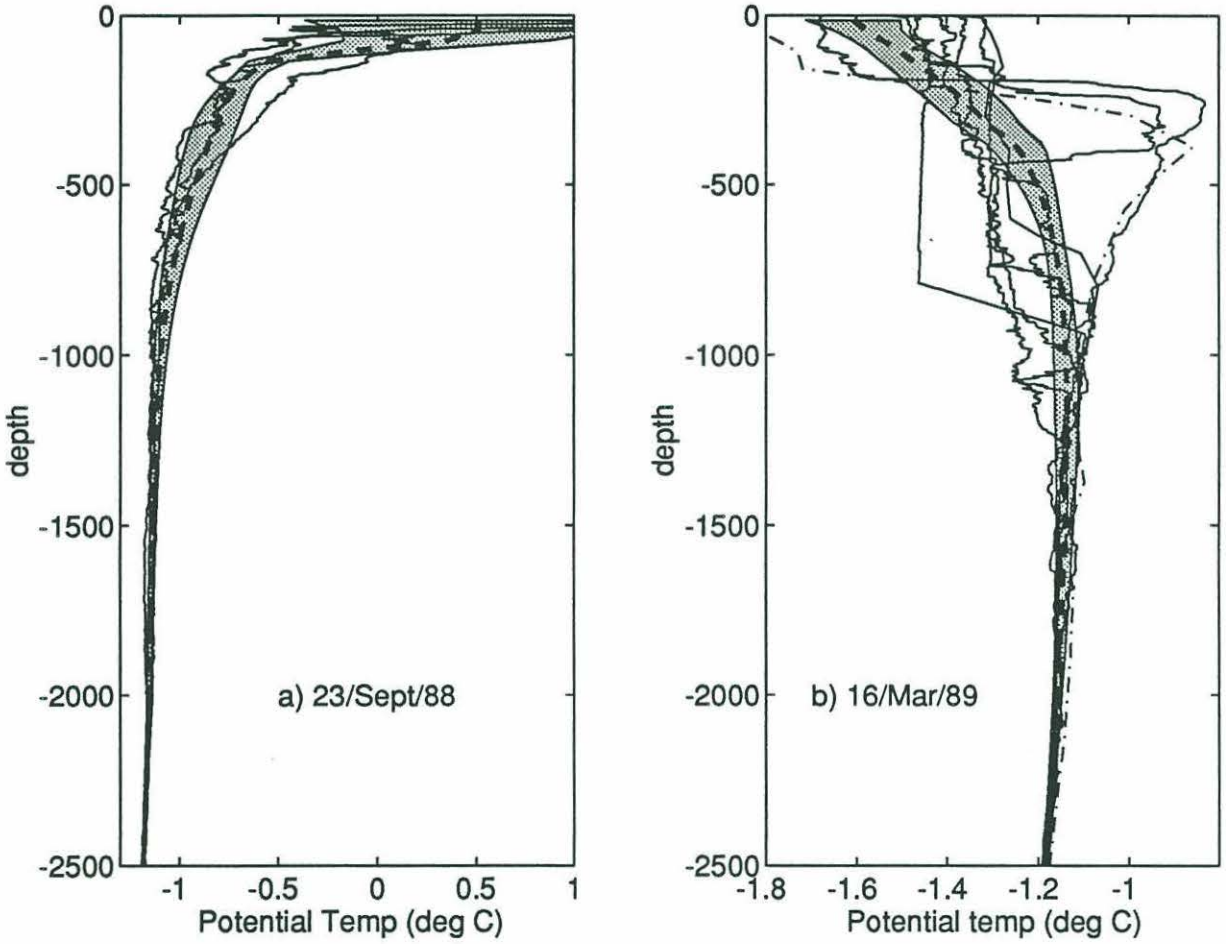

Figure 5-10: Comparison of point profiles with inverse profiles for the 1-4 path. a) At deployment. b) during the deep mixing period. Near mooring 1 large amounts of warm AIW can still be seen at intermediate depths. One cast shows a 700m deep mixed-layer of temperature -1.45°C. The accuracy of this cast is questionable.

5.5 Conclusions

The linear range-independent inverse is capable of capturing the essential thermal behavior of the Greenland Sea gyre. Iteration is necessary in the fall to produce consistent profiles, although the results without iteration are qualitatively correct. Temperature inversions match thermistor and point profile observations fairly well. Paths traversing the center of the array show that mixed-layers deepen rapidly in March. The 6-4 in particular seems to show only small along-track temperature changes so that inverse results for this path are most easily interpreted. Other paths originating at mooring 6 or crossing the array center seem to capture the range mean adequately, but larger along-track temperature changes make interpretation of this mean more difficult.

Although the inverses are less accurate during December and January because of modal dispersion of the broadband acoustic pulse in the near surface and inadequacies of the model structure, qualitatively correct results are shown obtained, improved by a non-linear fit of the robust heat content estimates to a one-parameter model of the temperature profile. From February to April, the temperature perturbations are small, and of deep extent, and iteration of the inverse is not required. Finally, the surface warms again in the summer. Because the deeper rays still pass through this part of the water column the heat content calculations are accurate within the uncertainty predicted by inverse theory.

It seems clear that tomographic methods can be applied successfully in high-latitude regions although resolution problems occur when shallow cold mixed-layers exist. For the instruments used, it is unlikely that tomography can be used for ranges greatly in excess of 200 km unless the transmissions times are greatly increased. The heat content remains a fairly robust measurement, as long as travel-times can be accurately determined.

Chapter 6

Validation of Surface Parameters

In order to correctly explain the tomographic results, we must consider them in relation to surface heat fluxes, winds, and changes in the ice cover. Estimates of these parameters were obtained from several sources, and it soon became clear that errors and ambiguities in this data would have to be resolved before useful results could be derived. In this chapter we describe the correction and validation of surface meteorological parameters (wind stresses and heat fluxes), as well as a sea ice concentration product derived from satellite observations.

6.1 Surface Ice

Daily estimates of surface ice concentration with a 25km resolution were derived from DMSP SSM/I (Defense Meteorological Satellite Program Special Sensor Microwave Imager) measurements. This is a satellite microwave radiometer in a polar orbit that provides brightness temperatures in 4 channels. There are a number of semi-empirical algorithms for determining ice concentration of consolidated first- and multi-year ice using a cluster analysis of the observed brightness temperatures (or derived quantities) in several microwave frequency bands and polarities [*Steffen et al.*, 1992]. This data is archived by the National Snow and Ice Data Center (NSIDC) and has been released on CD-ROMs including both raw data and ice products using the NASA-Team [*Cavalieri et al.*, 1984; *Gloersen and Cavalieri*, 1986] and Comiso [*Comiso*, 1986; *Comiso et al.*, 1989; *Comiso and Sullivan*, 1986] algorithms. For convenience the NASA-Team algorithm product is used here (it is similar to, although spatially smoother than, the Comiso algorithm product for the Greenland

Sea during the 1988-89 winter). Daily observations are very important, especially between February and April when significant changes can occur very quickly (see figure 7-6).

A fairly extensive validation has been carried out for the NASA-Team algorithm [*Steffen and Schweiger*, 1991; *Cavalieri et al.*, 1991] in regions of consolidated first- and multi-year ice. Estimated errors in the satellite product are of order 5% for the first-year ice concentration and 10% for the multi-year ice concentrations, with a "concentration" of about 15% corresponding to the ice edge. We will consider "concentrations" of less than 10% to be open water. However, the microwave characteristics of first-year and newly-formed ice are quite different, and as shown in *Grenfell et al.* [1992] the "concentration" product of the NASA-Team algorithm seems to correspond with the *thickness* of newly formed ice (i.e. ice less than perhaps 20cm thick) as well as its concentration. For example, a first-year ice "concentration" of 70% could also indicate a 100% ice cover of 10cm thick pancakes. Spurious "concentrations" of multi-year ice can also appear in regions of newly-formed ice. During March and April the changes in the microwave characteristics of the ice in the central Greenland Sea are rapid enough that it is likely much of the ice is being locally formed. During December and January the region is also covered by ice "concentrations" close to 90%, but as will be discussed in the next chapter, this ice is again probably of local origin. In any event, non-zero "concentration" values usually signify the presence of *some* kind of ice, and concentration values near 100% (seen in December and January) seem to be unambiguously correct. The apparent presence of low concentrations of multi-year ice is probably completely spurious, and is related to the presence of newly-formed ice, and so the multi-year concentration estimates will not be used or discussed further.

6.2 Meteorological Variables

Meteorological variables were obtained from analyses (assimilated hindcast rather than the forecast fields) of the United Kingdom Meteorological Office (UKMO) fine-mesh operational forecast model at 3-hourly intervals on a 0.9375° lat×0.75° long grid (a spacing of about 105km meridionally and 22km zonally in the array region). Surface heat fluxes and wind stresses in these analyses were obtained through bulk parametrizations involving surface and atmospheric quantities and Richardson number-dependent dimensionless exchange coefficients [*Bell and Dickinson*, 1987]. We have compared UKMO surface winds with those

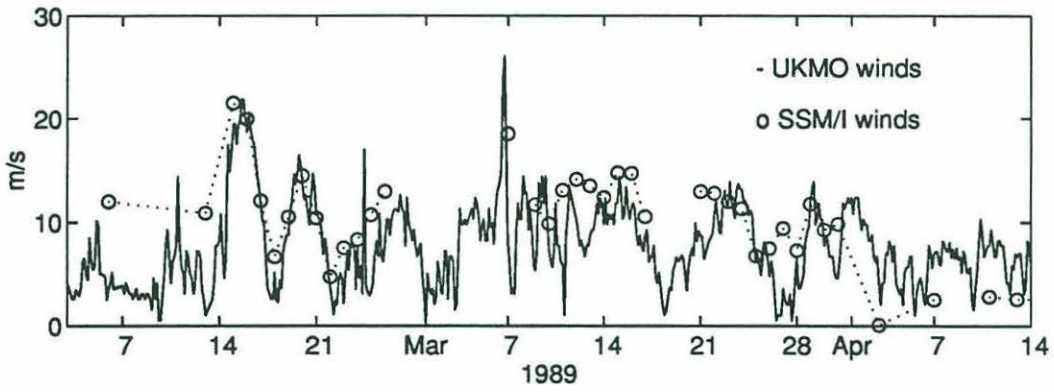

Figure 6-1: Comparison of 3-hourly UKMO and daily SSM/I winds during the deep mixing period

derived from SSM/I observations (R. Shuchmann, pers. comm. 1990) and found reasonable agreement (see figure 6-1). Comparisons of wind speed and air temperature with observations from two ships working in the Greenland Sea during February and March 1989 were also quite favourable, with UKMO air temperatures biased about 0.5 ± 2°C above ship temperatures over a range of about 25°C (see figure 6-2). UKMO surface winds were about 1 ± 3 m/s larger than ship winds over a range of 0-16 m/s, and directional differences were small. These results are consistent with those found in more extensive comparisons with ship observations in the North Atlantic [*Kent et al.*, 1991]. Efforts have been made to estimate the quality of the UKMO surface fluxes [*Alves*, 1992; *Taylor and Kent*, 1992], but generalization of these results to the Greenland Sea is difficult since there are strong regional and temporal dependencies even in mid-latitude oceans. The additional complication of a marginal ice zone results in some problems which apparently have not been considered before. We will therefore examine the fluxes in some detail. Since quantitative comparisons with the tomographic inverses will involve the time-integral of surface fluxes (the amount of heat energy transferred), we are concerned more with long-term (weekly to monthly) biases in the fluxes rather than short-term (hourly to weekly) random errors which will tend to average out. Two different sources of error and a procedure used to correct for them are now described.

6.2.1 Corrections for Erroneous Ice Limits

The most obvious error arises when examining the parametrization of ice effects. Ocean grid points in the UKMO model are classified as either ice covered or open (this classification will

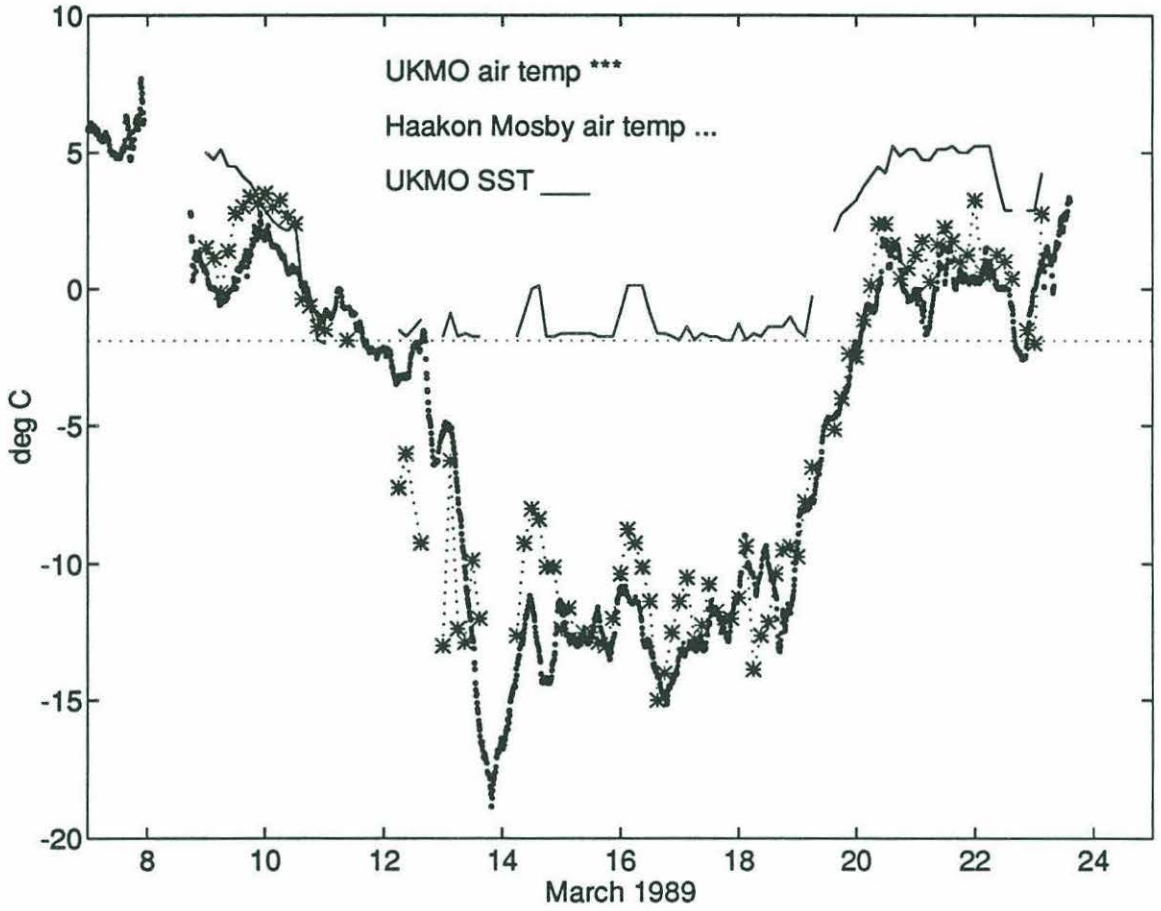

Figure 6-2: Comparison of daily observations of air temperature on the R/V Haakon Mosby during SIZEX 89 in the Greenland and Barents Sea with analyzed 3-hourly UKMO air/sea surface temperatures at the grid point nearest the current ship position. Data gaps indicate periods when the ship entered regions classified as ice-covered by the UKMO. Solid line is UKMO sea-surface temperature. Dotted horizontal line marks freezing point of seawater

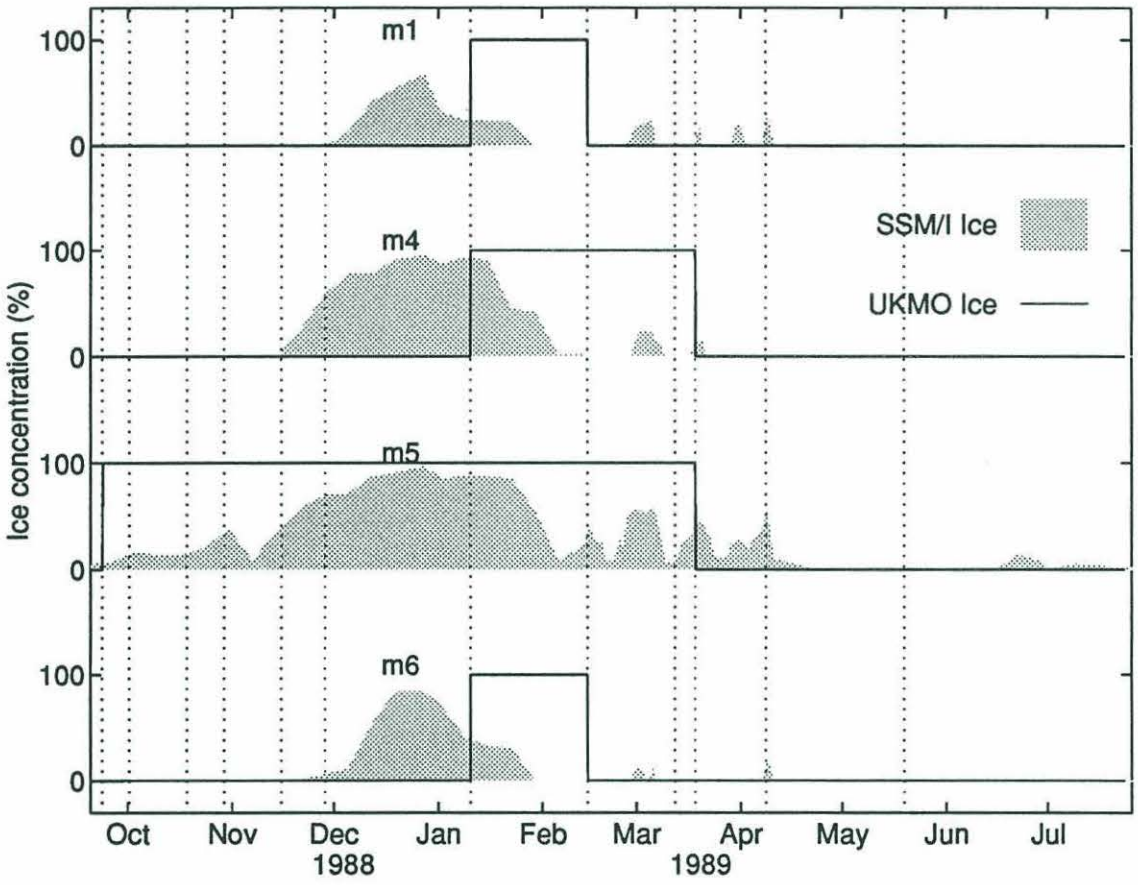

Figure 6-3: Comparison of UKMO ice classification and SSM/I observed concentrations at 4 moorings of the tomography array. UKMO ice limits are updated at times indicated by the vertical dotted lines

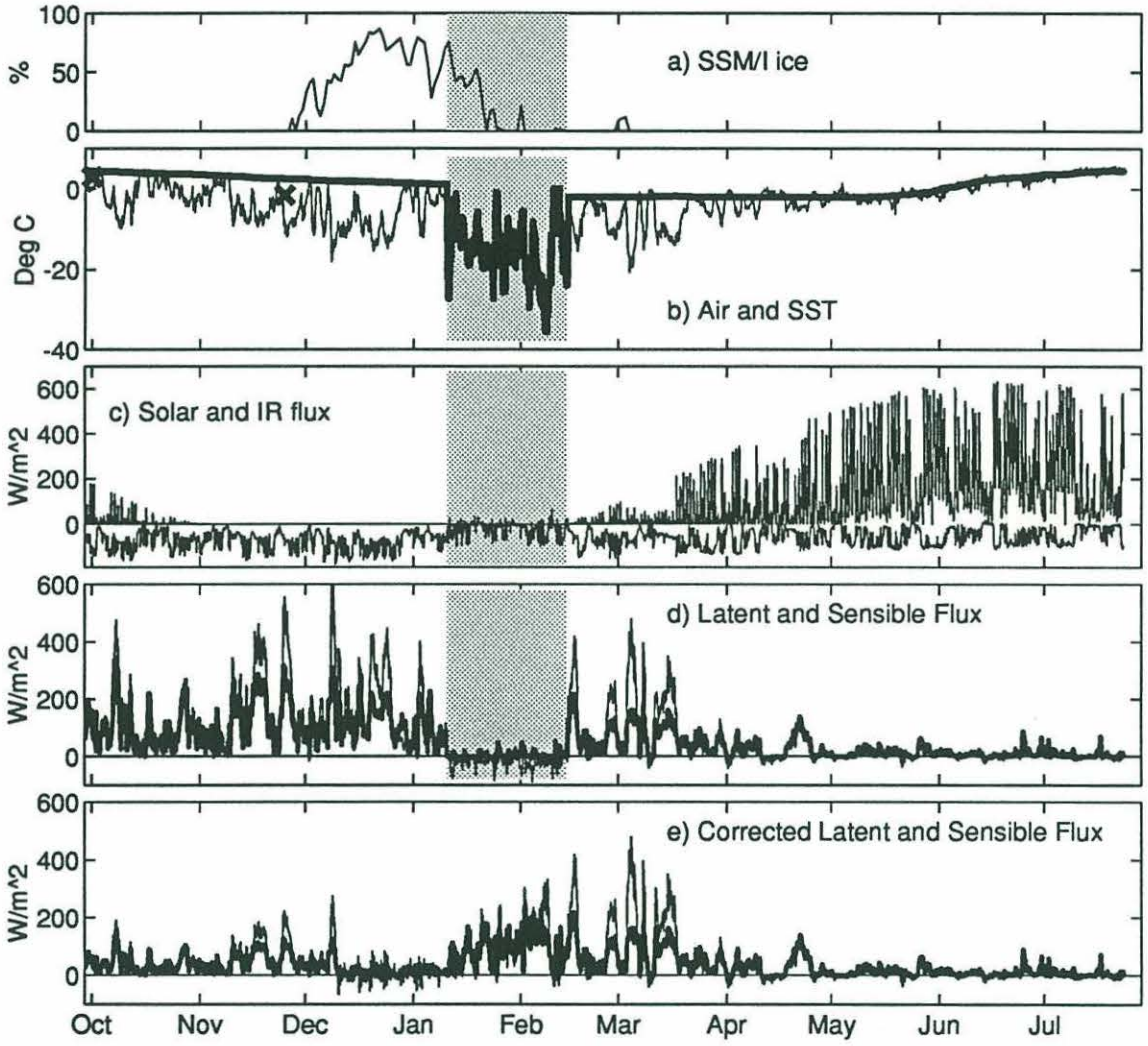

Figure 6-4: a) SSM/I (solid line) and UKMO ice (shaded region) classifications at m6. b) UKMO Air temperature (thin line) and SST (thick line) at m6. SST from oceanographic station data are shown by crosses in October and November. c) Net solar and IR fluxes at m6. Note the small decrease in IR fluxes due to the ice. d) Raw sensible and Latent fluxes at mooring 6. e) Sensible and latent fluxes after correction for incorrect ice and fall SST.

be called "UKMO ice" in the following discussion). UKMO ice limits are updated roughly every two weeks, although this is not always the case, and thus ice limits are usually two weeks out of date. It is also not clear what concentration the given ice limits represent. In any event, ice classifications at a given point in the array region (see figure 6-3) do not always agree with the far more accurate satellite observations (called "SSM/I ice" here, see also section 6.1 above). Although a 200km error in ice limits is probably not important in terms of large-scale atmospheric behavior, it *is* quite important for local heat budgets! For open ocean points the Sea Surface Temperature (SST) is apparently externally specified at daily intervals. For ice-covered grid points surface temperature changes depend on the residual of a surface energy budget divided by a volumetric heat capacity of $1.32 \times 10^5 \mathrm{Jm}^{-2}\mathrm{K}^{-1}$. If temperatures are below the freezing point of seawater, they are relaxed towards that point with a two day time scale to crudely model the upward flux of heat through the ice [*Bell and Dickinson*, 1987], however this effect is not very noticeable and surface temperatures are usually close to air temperatures over ice (see figure 6-4b), whereas the difference can be very large over open water. Thus there can be a very great difference in over-ice and over-water fluxes. Luckily, the fluxes have large spatial scales over ice or open-ocean regions (but can vary greatly *between* these regions), and after careful examination of these spatial characteristics, a correction for the erroneous ice limits was attempted.

For every grid point, *equivalent over-ice* (F_{EOI}) and *equivalent open-water* (F_{EOW}) flux series were created from the UKMO fluxes F using the following algorithm:

- If the grid point was classified as open water in the UKMO analysis, F_{EOW} was set to F, and F_{EOI} was set to the F of a nearby ice-covered point.
- If the grid point was classified as over ice in the UKMO analysis, F_{EOI} was set to F, and F_{EOW} was set to the F of a nearby open-water point.

In this context, "nearby" was assumed to be the closest relevant point on the same line of latitude, which in many cases was also the closest relevant point. The two series were then combined to form an ice-corrected flux series F_c using the SSM/I ice fractional ice concentration I. On physical grounds, a linear weighting may seem reasonable

$$F_c = I \cdot F_{EOI} + (1 - I) \cdot F_{EOW} \tag{6.1}$$

however the UKMO model has presumably been tuned somewhat to generate reasonable

flux values in ice-covered regions where I is usually less than 1, so it is perhaps more reasonable to use a threshold weighting

$$F_c = \begin{cases} F_{EOI}, & I > I_0 \\ F_{EOW}, & I \leq I_0 \end{cases} \tag{6.2}$$

for some threshold value I_0 that marks the transition between open-water to ice-covered classifications. A value of 0.4 was used for this purpose since that seems to be a standard definition of the ice edge. Both weighting functions were considered, and resulted in similar corrections; we shall take the difference between the two corrections as representing the uncertainty of the result. Heat fluxes in the UKMO model are divided into 4 components: net short-wave, long wave, sensible, and latent fluxes. Each component was investigated separately.

Corrections to the net short-wave flux (solar radiation modified by clouds and surface albedo) were very small, because ice effects are generally limited to periods in which the sun is near or below the horizon. However, cumulative fluxes exhibit almost no zonal dependence (as one might expect), so that taking "nearby" points to be on the same latitude is a good approximation.

Changes to the net long-wave flux (black and grey-body radiation from the surface, atmosphere, and clouds) are also small, on the order of 10-30%, since there does not seem to be a large difference between over-ice and open-water values. The long-wave flux is never the dominant term in the heat budget (see figure 6-4).

The latent fluxes Q depend on the difference between the specific humidity q_a and the saturation-specific humidity q_s of the surface potential temperature θ_s, the wind speed $\mathbf{v}$, the latent heat of evaporation L, the air density ρ_a, and a dimensionless exchange coefficient C_E that depends on a bulk Richardson number:

$$Q = -\rho_a L C_E |\mathbf{v}| \{q_a - q_s(\theta_s)\}. \tag{6.3}$$

Latent fluxes can be large over water, but are almost invariably quite small (in fact, almost non-existent) over ice (see figure 5.4c). In the vicinity of the tomography array, annual mean latent fluxes are more constant meridionally than zonally. However, examination of the raw data indicates that latent fluxes are correlated with storms (i.e. $\mathbf{v}$ is important),

and so we generally want to use the *nearest* point when making the equivalent-flux series. This usually turns out to be a point with the same latitude. Corrections to these fluxes can be large (more than 100%), but in many cases they are of opposite sign during different periods of the year and tend to cancel out in long-term means.

Sensible fluxes H are most affected by the incorrect ice limits, since they depend crucially on the difference in air and surface potential temperatures (θ_a and θ_s respectively):

$$H = -\rho_a c_p C_H |\mathbf{v}| \{\theta_a - \theta_s\} \tag{6.4}$$

(c_p is the specific heat capacity and C_H an exchange coefficient). Air-surface temperature differences are usually quite small over ice (a few degrees), but can be 20°C or more over open-water. However, fluxes are well-correlated zonally so taking "nearby" points on the same latitude yields reasonable results.

Overall, the annual mean net fluxes are changed by 0-60 Wm^{-2} through this procedure. There is an uncertainty of 0-15 Wm^{-2} depending on whether (6.1) or (6.2) is used to form the corrected flux series.

6.2.2 Corrections for Erroneous Sea-surface Temperature

During other parts of the year, the fluxes sometimes suffer from less obvious problems. In September–November, the UKMO sea-surface temperature (SST) seems to be too high by several degrees (see figure 5.4b). During this period winds are from the north, i.e. from the icepack. The temperature of the air over the array is therefore mostly determined during its residence over the ice field and is quite low. It is in any case usually much colder than the SST. It is therefore likely that air-sea temperature differences are significantly overestimated during this time, leading to a probable overestimate of the latent and sensible fluxes which dominate in the fall. Using CTD observations made during September and November (J. Swift, pers. comm. 1991) we find the change in mixed-layer heat content to be about 9×10^8 Jm^{-2}. Assuming that no net advection of heat occurs in the mixed-layer, this change implies a net surface heat flux of about 145 Wm^{-2} compared with the UKMO mean value of about 270 Wm^{-2} over the same time period (after the ice corrections described above have been applied). It should be noted that the net salt content of the array region does not change substantially during this period, suggesting that advection is

not important. Open-ocean latent and sensible heat fluxes during this period are therefore scaled by 0.4 so that net fluxes match the observed changes in mixed-layer heat content (see figure 5.4d). Net infrared and solar fluxes are not sensitive to surface temperature (they are affected more by cloud cover and albedo) and so are not modified.

During February-March, the SST in open-ocean areas was nearly correct, and as shown above air temperature and surface winds compared favourably with ship observations. The net heat flux is dominated by sensible and latent fluxes, which each average about 100 Wm^{-2} at this time. Flux accuracy is probably mostly determined by the correctness of the bulk formulae. *Taylor and Kent* [1992] found that large sensible and latent fluxes were underestimated by about 20% in a comparison with ship observations in the North Atlantic, but it is not clear to what extent their conclusions hold in the Greenland Sea given the spatial variability of the biases. As the authors point out, it is also not clear to what extent this difference represents shortcomings in the ship data.

After April, surface winds are light and although the sea surface temperature is incorrect (being too cold by about 1°C) it is very close to the model air temperature and thus latent and sensible fluxes are small. The net heat flux is dominated by incoming solar radiation. Although this can be affected by clouds, integrated fluxes are probably fairly accurate during this period (i.e. bias due to cloud cover is not large). It is interesting to note that the solar heat flux is not significant until April, although the sun is above the horizon long before that. Presumably this is because the low angle of the sun, combined with cloud cover, effectively reduces the incident radiation to a very small value.

6.2.3 Long-term biases

Since we will be concerned with energy budgets, it is of interest to identify any long-term biases in the heat fluxes. The net mean (corrected) UKMO flux out of the array region from the middle of September 1988 to the end of July 1989 lies in the range 55–73 Wm^{-2} depending on ice cover, compared to annual mean values over open water of about 100 Wm^{-2} [*Häkkinen and Cavalieri*, 1989], 80 Wm^{-2} [*Gorshkov*, 1983], and 73 Wm^{-2} [*Esbensen and Kushnir*, 1981]. Although the annual mean of the UKMO fluxes will be slightly smaller than the 10.5 month mean since net fluxes are *into* the ocean during the other 1.5 months, this reduction is partially compensated by ice effects during December and January which tend to reduce the net UKMO fluxes *out* of the ocean under ice cover relative to open-ocean

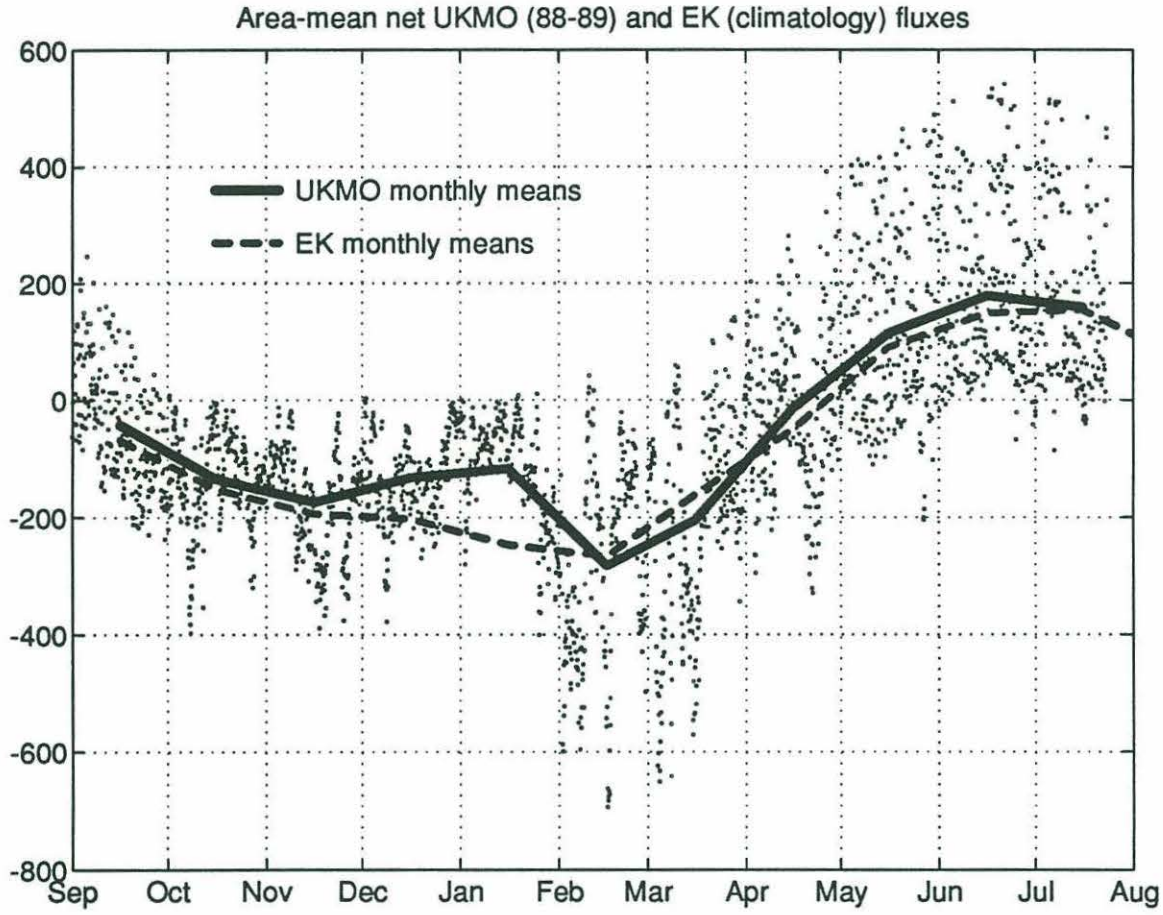

Figure 6-5: Comparison of corrected net UKMO fluxes averaged over the array region at 3 hourly intervals (dots) and their monthly means (solid line) with the climatology of *Esbensen and Kushnir* [1981] (dashed line).

fluxes, and so the agreement is quite good. It is also possible that annual means vary greatly; mean annual fluxes over a 30 year period at Ocean Station Bravo in the Labrador Sea were found by *Smith and Dobson* [1984] to vary between 7 and 87 Wm^{-2}. Finally we compare the monthly means of the corrected UKMO fluxes averaged over the array region with the monthly climatology of *Esbensen and Kushnir* [1981] (figure 6-5). Monthly means differ by about 20 Wm^{-2} before December, and by up to 40 Wm^{-2} from February onwards. During the ice-covered period the climatology estimates are of open-ocean fluxes which are clearly inappropriate here.

Although the above analysis indicates that flux errors vary greatly in type and size over the seasonal cycle, for comparative purposes it is useful to make a rough estimate of the "usual" uncertainty, which seems to be of order 50 Wm^{-2} on monthly scales. In view of the surprisingly good agreement between net surface heat fluxes and the heat content changes inferred by tomography which are discussed below, it should be emphasized that both series (after all corrections have been applied) are *entirely* independent of one another.

Chapter 7

Thermal Evolution of the Gyre

In this chapter we combine material from the previous chapters in order to describe and explain the seasonal changes in the Greenland Sea Gyre in 1988-89. We show that deep mixing occurred in a well defined region that contained the 6-4 path in the center of the gyre. This region can be identified in satellite maps of the surface ice as a large opening of hole in the icepack. Within this hole, large surface fluxes resulted in the downward convection of cold water in a field of plume events that lasted only a few days. During successive cooling events the depth of mixing increased to at least 1500m, while around the edges of this region mixed layer deepening proceeded more slowly in a stepwise fashion in which surface ice appeared several times. Finally, mixed-layers to the north and west in the region permanently covered by ice appear to deepen very little; profiles from these regions were seen episodically in the 1-5 path due to horizontal advection.

7.1 Seasonal Cycle of temperature and heat content

Heat content of the water column – and in particular its changes – is the most robust product of tomography in this region (more details about this and other aspects of the inverses are given in chapter 5). Consider a box of water with potential temperature Θ covering unit area between the surface and some fixed depth below which the temperature remains constant (chosen here to be 3000m). We can define the heat content H of this volume as

$$H = \int_0^{3000} \rho c_p \Theta dz \tag{7.1}$$

where for practical purposes we take the density ρ and heat capacity c_p to be constant. We write a conservation equation for heat content in this box:

$$\frac{\partial H}{\partial t} - \iint F_s dA_s = -\sum_i \iint u_i \rho c_p \Theta dA_v + \textit{diffusion and mixing terms.} \qquad (7.2)$$

The first term represents changes in the box heat content, the second term represents the energy exchange via surface heat fluxes F_s, and the right-hand side represents the advection u_i of heat and lateral mixing through the i sides of the box. Collectively the right hand side thus represents the horizontal divergence of heat. For our purposes it will be more convenient to use the time integral of (7.2),

$$H(t) - \left[H(t_0) + \int_{t_0}^{t} (\iint F_s dA_s) dt\right] = -\int_{t_0}^{t} (\textit{horizontal divergence terms}) dt \qquad (7.3)$$

since tomography measures $H(t)$ directly, and integration of the surface flux terms makes the resulting series much smoother. Note that the constant $H(t_0)$ has been lumped with the surface flux term here, so that time series of surface heat loss will lie close to time series of heat content in figures. The extent to which the difference between the first two terms (called the "heat residual") changes during various times of the year is a measure of the importance of heat advection, but is also affected by uncertainties in the observed quantities. The uncertainty in the inverses is composed of a random component which has no temporal correlation, and a bias which will vary on a monthly scale but which has no cumulative effect. In contrast, the time-integration of surface fluxes will effectively eliminate the random error associated with day-to-day inaccuracies, making the longer-term biases the dominant error in the comparison. These errors *are* cumulative, and are probably greatest during the ice-covered period.

At this point we must briefly digress to discuss the effect of other terms in the heat balance. In the following discussion, we outline a theory that relies explicitly on the formation of sea ice to precondition the surface waters in the early winter. However, the heat content calculations presented as evidence for this theory compare water column heat content with surface fluxes, ignoring the thermal properties of the ice cover. Modifications to the heat balance (7.2) incorporating ice effects consist of three terms: heat content changes due to changes in ice temperature, the latent heat flux associated with ice formation and melting, and the heat content of advected ice.

A complete discussion of these effects would necessarily be quite complicated. First, the presence of brine makes the thermal properties of sea ice heavily dependent on salinity and temperature. Specific heat capacity alone can vary over several orders of magnitude at near-freezing temperatures [*Schwerdtfeger*, 1963]. Secondly, parameters such as the rates of ice formation/advection and ice thickness which appear in these terms are basically unknown (although as we shall show later, their *combined* effects over the winter can be determined). However, a simple analysis of the relative magnitudes of these various terms shows that their effects are close to or smaller than the errors in the estimates of the other terms. For our purposes, we choose representative values for the various constants: latent heat of formation $L \approx 3 \times 10^5$ Jkg^{-1}, and heat capacity $c_i \approx 3 \times 10^3$ Jkg^{-1}K^{-1}. Then the energy per unit area required to change the temperature of $h = 50$cm of ice by $\Delta T = 10°C$ is

$$\Delta H = \rho c_i h \Delta T \approx 1.5 \times 10^7 \text{ Jm}^{-2} \tag{7.4}$$

and the latent heat per unit area associated with the formation of that ice is:

$$\Delta H_f = \rho L h \approx 1.5 \times 10^8 \text{ Jm}^{-2} \tag{7.5}$$

(see also the indicated bar in figure 7-1). Changes in the surface ice concentration due to ice formation or advection will result in a net gain or loss of energy associated with latent heat changes.

Although the first of these is far smaller than the uncertainty in tomographic heat content estimates, the second is somewhat larger. However, the possible monthly biases in the heat fluxes were estimated in chapter 6 as being of order 50 Wm^{-2}, or 1.3×10^8 Jm^{-2}, and it is likely that the errors in the fluxes during the ice covered period are even larger. Thus we do not include these terms in equation (7.2).

Figure 7-1 shows the heat content of the 6-4 path and the surface heat losses averaged over that path (i.e. the two terms on the left hand side of (7.3)) compared with a climatological monthly heat content for the array region based on the analysis of Chapter 3. The 6-4 path shows the seasonal cycle best since it seems to lie almost entirely within the region in which deep mixing occurred. Other paths lie outside this region, either totally (e.g. 4-5 and 1-5), or partially (e.g. 1-4 and 6-5) which makes interpretation of the range averages more difficult. The observations are entirely consistent with the climatology, although this

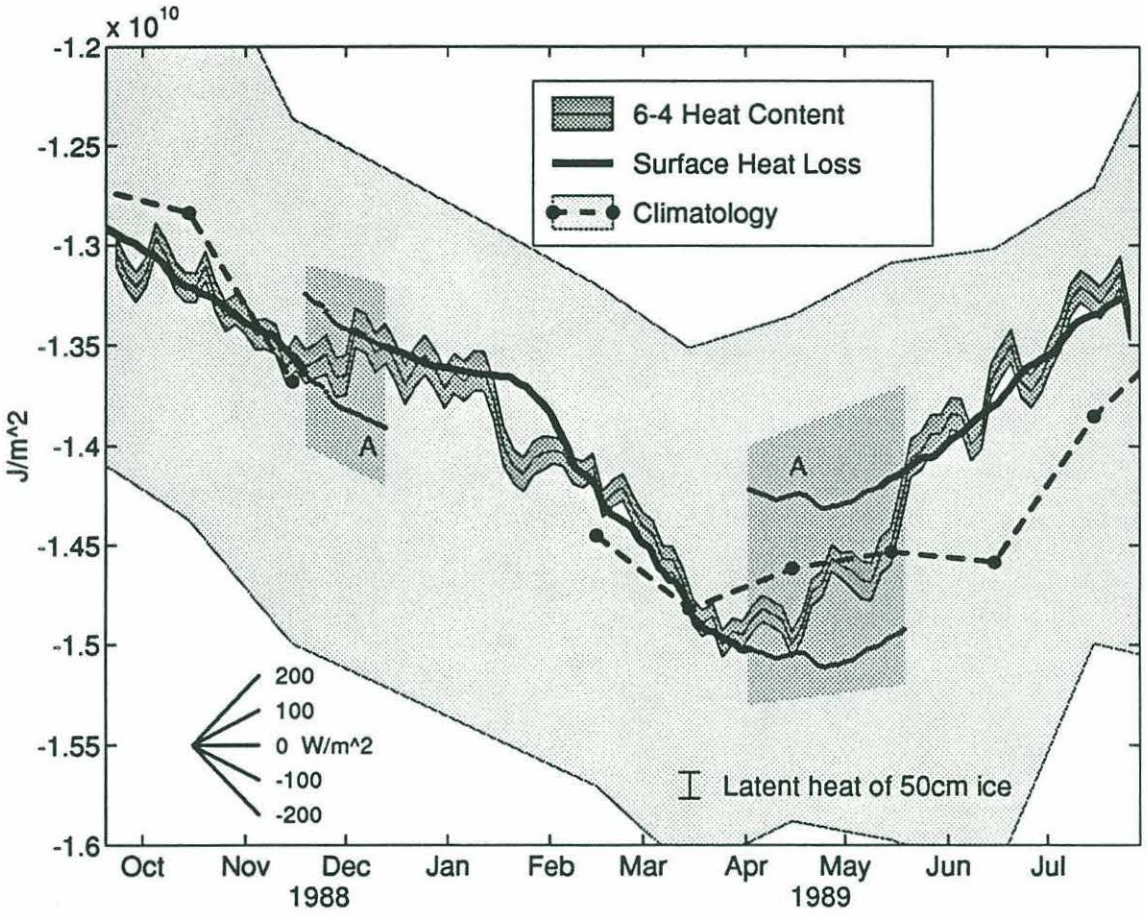

Figure 7-1: Tomographic Estimates of heat content at 3 day intervals for the 6-4 path (dark shaded region) are consistent with monthly mean heat contents for the array region from the climatology of Chapter 3 (dots connected by dashed line) within the range of historical data estimated with a median absolute deviation statistic (lightly shaded portion). Surface heat losses (thick line), track the heat content changes very well, except during the end of November and April/May when significant advection occurs (these time periods are indicated by shaded regions labelled "A"). A transient cold advective feature also appears in late January. The surface heat loss curve has been broken and re-offset during each advective period to show the degree to which relative changes match those of the heat content at other times. The latent heat of formation of 50cm of ice is shown; this value is smaller than other errors and is therefore neglected in the analysis. For comparative purposes, slopes corresponding to various heat fluxes are indicated in the lower left corner. The estimated bias errors in heat fluxes are of order 50 Wm^{-2} on monthly scales.

path appears to be warmer than expected at the end of the experiment. The surface heat loss can explain all changes in the water column heat content except during the end of November and during April/May (marked by the shaded regions labelled "A"), implying that significant inflow of heat occurs only during those two periods, and that over most of the year heat content changes can be explained through local surface fluxes alone. The large but transient cold feature that occurs near the end of January appears in some other paths, but its origin is unknown. The surface heat loss curve has been broken during each advective event (i.e. a different $H(t_0)$ term is used in the second term of (7.3)) so that the close agreement can be shown during other times. The most rapid cooling occurs in February and March, and the least rapid seems to occur during December and January when a surface ice cover insulates the mixed layer from the atmosphere and reduces the latent and sensible fluxes. The water column begins to warm slowly in April, and warms steadily in June and July.

We can more easily see advective effects by examining the heat residuals. Figure 7-2 shows the heat residuals for both the 6-4 and 1-5 paths. Overall they show an upwards trend, indicating that there is a net loss of heat to the atmosphere. During periods when the heat residual series are level, there is no horizontal divergence of heat, i.e. no advection. This characterizes the 6-4 residuals for most of the year, except (as discussed above) during November and April/May. In contrast, the 1-5 path shows large amplitude fluctuations with a period of about 50 days superimposed on a gradual increase. Although these paths are separated by less than 100km, they obviously lie in very different dynamical regimes.

In figure 7-3 we see the evolution of the potential temperature profile of the 6-4 path. Temperature series in this and the following figure have been slightly smoothed in time using a 3 point filter with relative weights of 1-4-1 giving a 3dB point at about 0.09 cpd. In general the steady changes indicated by the heat residual series are evident in the simple structure of this time series. The most striking detail is the very cold, shallow mixed layer that occurs under large concentrations of ice during December and January (during which the net heat fluxes are very small due to the insulation provided by the surface ice). This mixed layer warms slightly and rapidly deepens in the latter half of February and the first few weeks of March down to about 1500m. During this time net fluxes over the largely ice-free surface are large, reaching peaks of 500 Wm^{-2} during periods of strong northerly winds. Complete vertical homogeneity of the range-averaged potential temperature profiles does

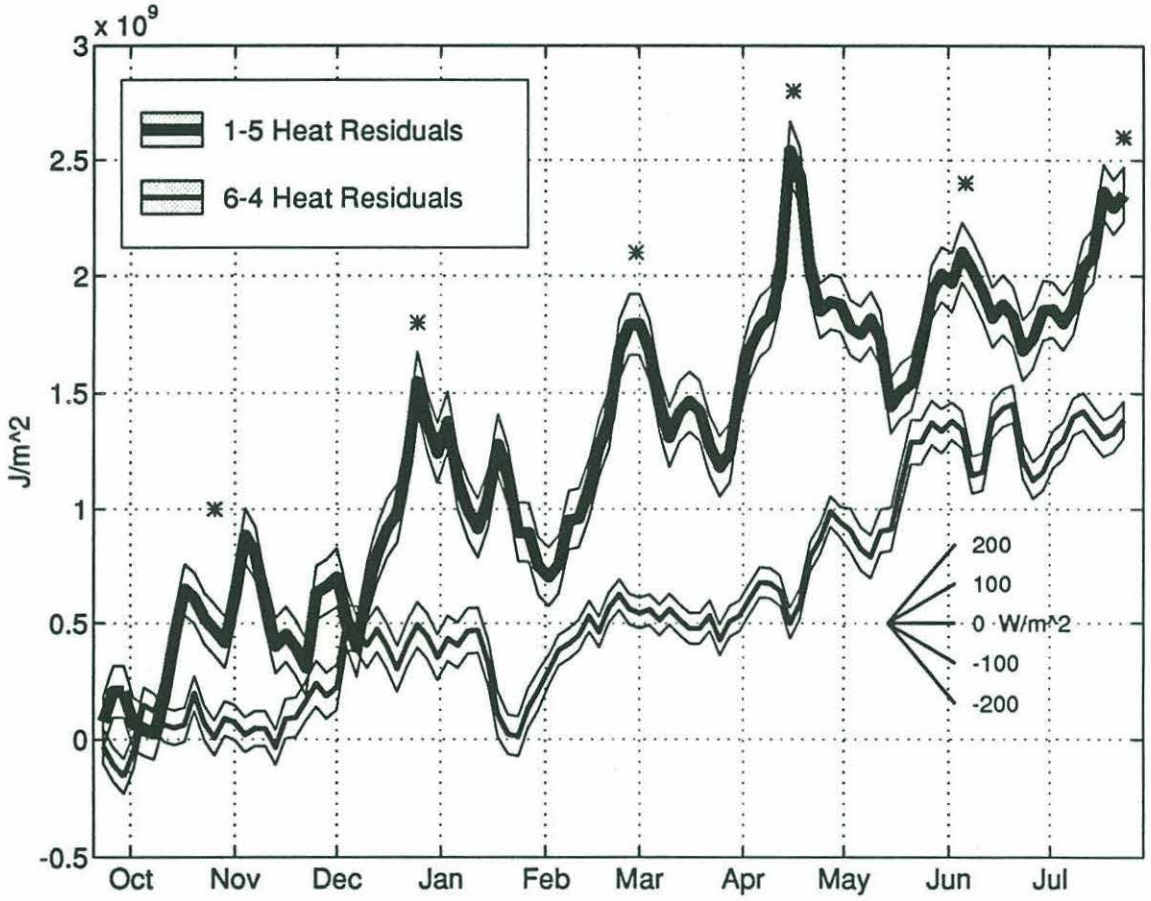

Figure 7-2: Heat residuals for the 6-4 and 1-5 paths. Because the 1-5 path is generally warmer than the 6-4 path its heat residual curve appears slightly above that for the 6-4 path. The 6-4 residual series is mostly flat except during November and April/May, however the 1-5 path shows large fluctuations (with peaks marked with '*') at approximately 50 day intervals, superimposed on a gradual increase. Uncertainty of the tomographic estimates are shown by the thin lines. The net change in these curves corresponds to a mean heat loss of about 50 Wm^{-2}. Slopes corresponding to other values of heat flux are shown by the diagram in the bottom left, bias errors in heat fluxes are of order 50 Wm^{-2} on monthly scales.

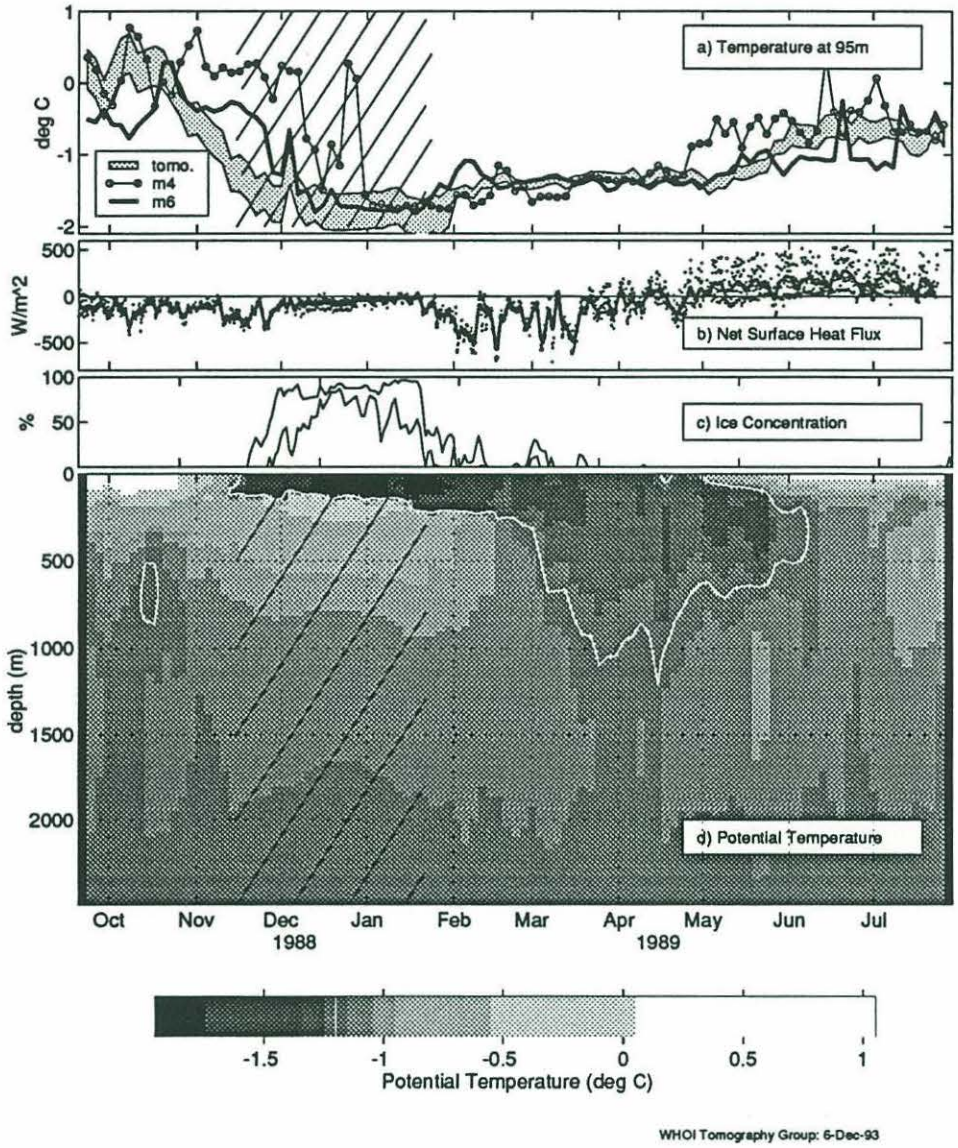

Figure 7-3: Seasonal temperature cycle for 6-4 path. a) Comparison with thermistor records at 95m. b) Path-averaged net surface fluxes (a three-day smoothed series is shown with a thick line). c) Ice concentration at endpoint moorings. d) 3-daily range-averaged potential temperature profiles for the 6-4 path. Total (random) inverse uncertainty is about $\pm 1°C$ ($\pm 0.5°C$) in the warm mixed-layer, about $\pm 0.2°$ ($\pm 0.07°$) above 400m, $\pm 0.05°C$ ($\pm 0.02°$) at 500m, and $\pm 0.02°C$ ($\pm 0.015°$) at 1500m; isotherms may be in error by up to 200m vertically near 1000m. During the deep mixing period total uncertainty is similar to random uncertainty. White contour line indicates $-1.2°C$. Diagonal hatching indicates the period when temperature profiles were determined by a one-parameter fit to heat content estimates (see Chapter 5 for details).

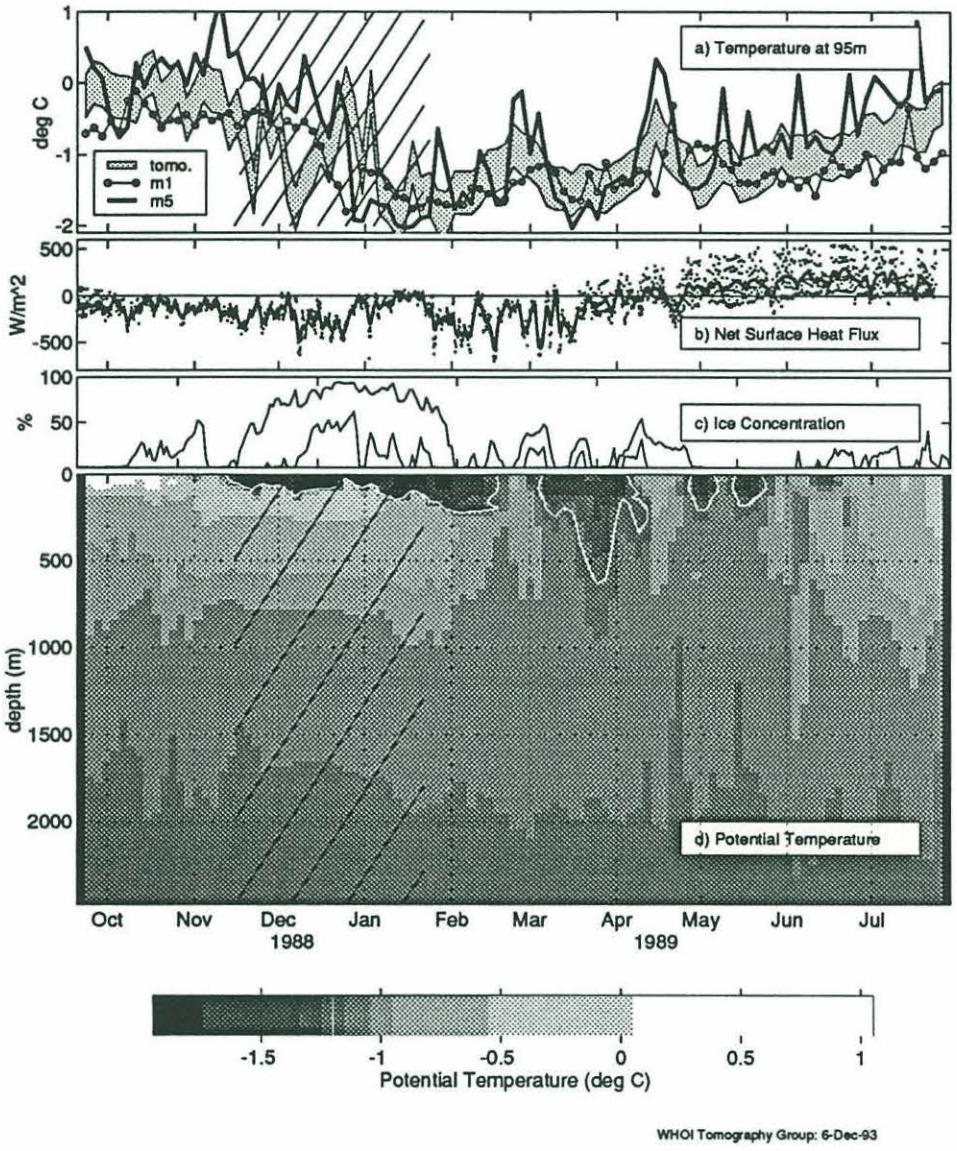

Figure 7-4: Seasonal temperature cycle for 1-5 path. a) Comparison with thermistor records at 95m. b) Path-averaged net surface fluxes (a three-day smoothed series is shown with a thick line). c) Ice concentration at endpoint moorings. d) 3-daily range-averaged potential temperature profiles for the 1-5 path. Total (random) inverse uncertainty is about $\pm 1°C$ ($\pm 0.5°C$) in the upper 30m, about $\pm 0.2°$ ($\pm 0.07°$) above 400m, $\pm 0.05°C$ ($\pm 0.02°$) at 500m, and $\pm 0.02°C$ ($\pm 0.015°$) at 1500m; isotherms may be in error by up to 200m vertically near 1000m. White contour line indicates $-1.2°C$. Diagonal hatching indicates the period when temperature profiles were determined by a one-parameter fit to heat content estimates (see Appendix A for details).

not occur during the deep mixing period - surface waters are colder than deeper waters, with a slight potential temperature maximum appearing at a maximum depth of about 1500m. Above this level potential temperatures slowly decrease towards the surface. Thus this is not a canonical well-mixed mixed layer. The deepening stops near the end of March when surface heat fluxes become quite small and/or positive. During May and June the deep temperature profiles show significant fluctuations, before settling down to a steady warming.

The seasonal evolution seems to divide itself naturally into three distinct phases: 1) A preconditioning phase (October-January) during which the mixed layer cools due to local fluxes, remains fairly shallow, and is covered by dense ice at least part of the time, 2) a deep mixing phase (February-March) during which the mixed layer rapidly deepens under the influence of local surface fluxes, and 3) a restratification (April-June) in which significant advection occurs.

Temperature inverses for the 1-5 path appear quite different. Figure 7-4 shows that the heat content fluctuations seen in figure 7-2 are associated with vertically coherent changes in the thermal structure. The warm events are correlated with the presence of surface ice at mooring 5, so that there must be a layer of water near the surface at the freezing point. This does not appear in the tomographic profiles (nor does it appear in the mooring 1 and 5 thermistor records at 95m) - it is likely that this cold layer is too thin to be resolved by the inverse, although the freezing point *is* within the uncertainty of the tomographic estimate of *surface* temperature. Mooring 5 is very close to the ice edge and fluctuations in the ice cover above it can be seen over the whole year, however the other endpoint (mooring 1) remains fairly ice-free even during December and January. Thus the path-averaged fluxes do not show the effects of insulation quite as dramatically as do those of the 6-4 path (figure 7-3b). Although the March heat losses are just as large, neither do we see a rapid deepening of the mixed-layer to 1500m. Instead we see a mixed-layer depth of no greater than about 900m, and this does not appear until the second half of March. Horizontal displacements of the water column apparently result in observations of either the mixed-layer at the edge of the gyre (which deepens but not as much as that in the gyre center), or the waters underneath the permanent ice edge, where the mixed layer appears to be always shallower than 95m.

We shall now examine the details of each phase of the thermal evolution in the gyre center in more detail.

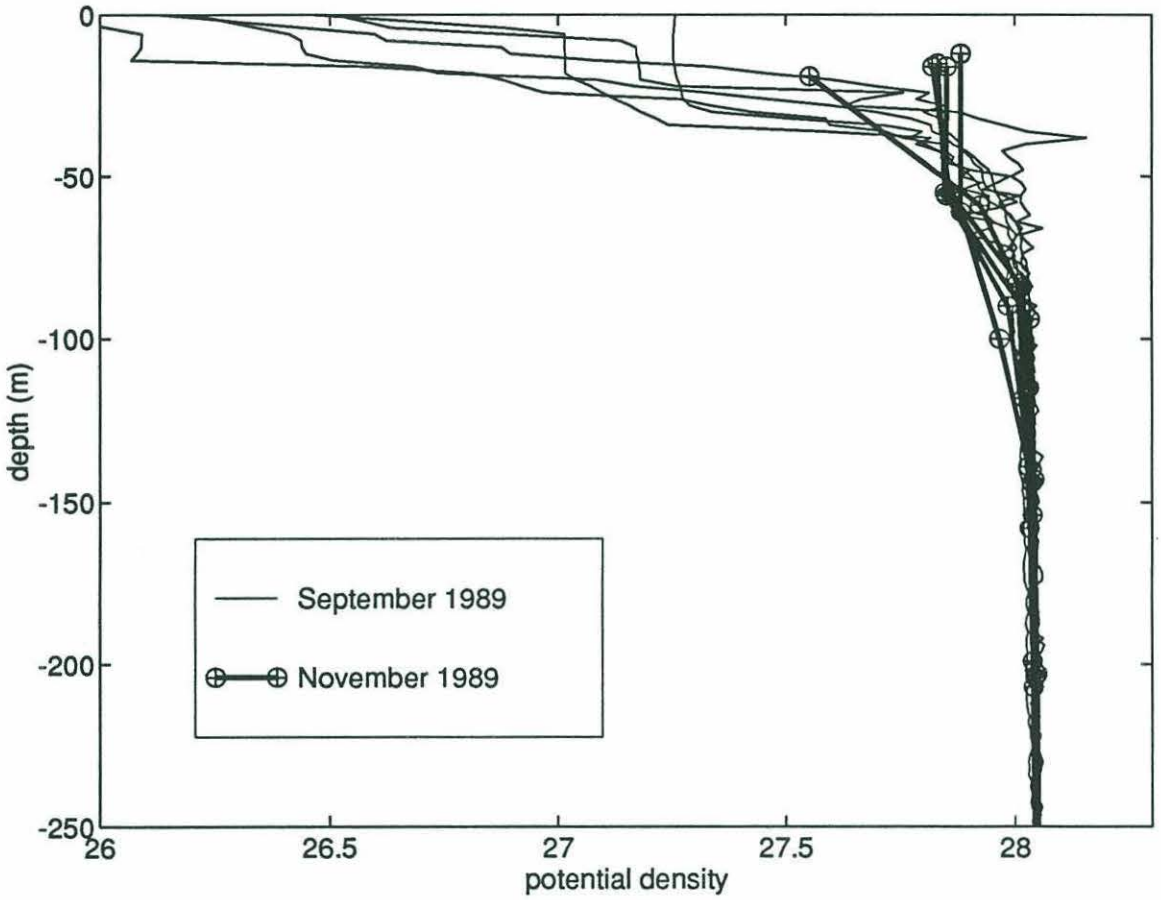

Figure 7-5: Density profiles for September and November 1989 from hydrographic stations. Mixed layer depth is about 30m in September and about 70m in November. The density increase in the mixed layer is due to cooling from 4°C to the freezing point, as well as entrainment of salt from below.

7.2 Preconditioning phase

CTD observations made during the deployment indicate that the surface mixed layer in September is quite fresh compared to the underlying AIW, with salinities of about 33-34 compared with deeper values of 34.89 at most stations, although at mooring 6 surface salinities are about 34.3. Negative surface fluxes then cool only the shallow mixed layer. Towards the end of November, mixed layer temperatures approach the freezing point, however a substantial density jump still exists at the base of the mixed layer (see figure 7-5). During this period there is no change in net water column salt content and so the increase in mixed layer salinity to about 34.65 at mooring 6 is due to wind-driven entrainment alone as the mixed layer depth increases from about 30m to about 70m.

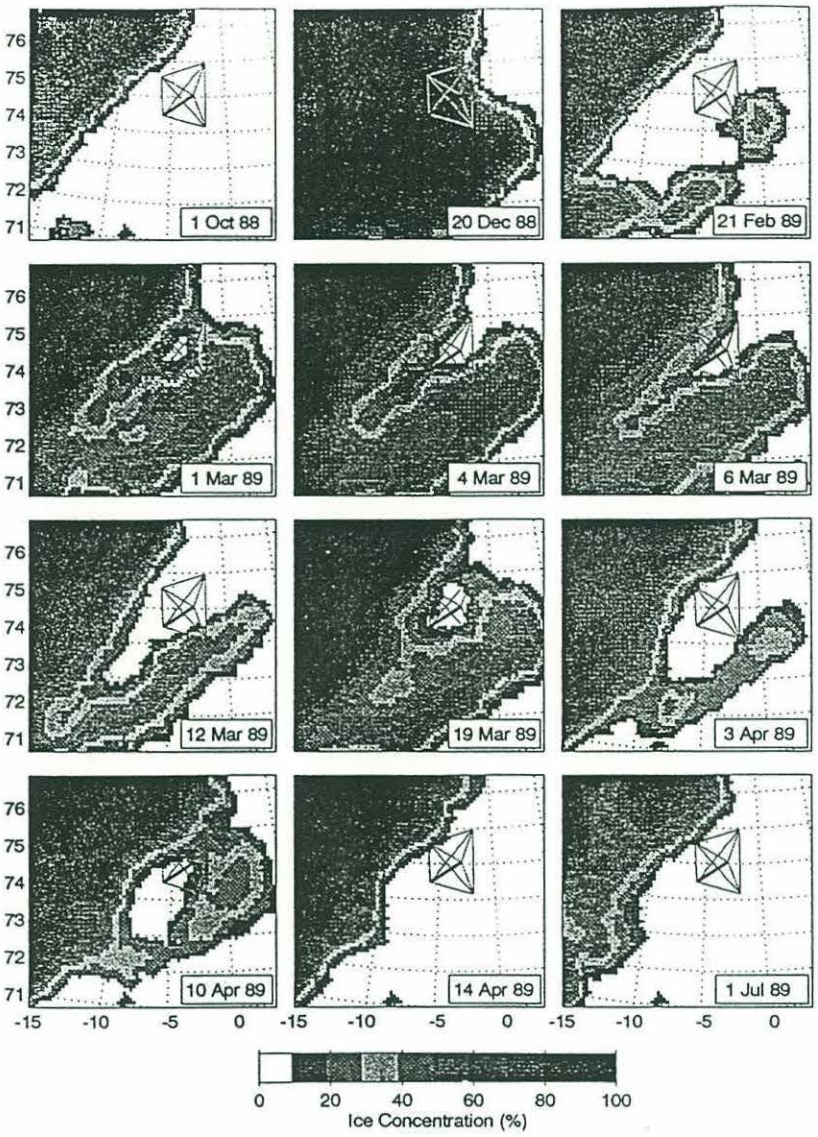

Figure 7-6: Ice concentrations over array region during 1988/89. Dates of successive minima and maxima of the areal coverage are shown. Although contours are labelled as concentration, they also depend on ice thickness in the odden tongue (the large diagonal feature along the south-east edge of the ice pack) through February-April. Concentrations below 10% are shown as open water (see 6.1 for details). Array paths for which temperature inverses are available are shown as thin lines; the 6-4 path is indicated by a thick line. Note the small region that always remains ice-free over the array center after February. Ice exists only to the west of the "permanent" ice edge from April to October (first, and last two panels).

At this point dense concentrations of ice appear over the entire array region, as shown in figure 7-6. The irregularly spaced dates shown correspond roughly with successive maxima and minima in the areal coverage of ice over the array region.

It is unfortunately not possible to distinguish between newly formed ice and advected first year ice using the standard concentration algorithms (see the discussion in section 6.1), so that it is not possible to tell from these satellite images alone whether ice is forming locally. Animations of the daily ice concentration estimates indicate that the ice edge seems to advance about 400km in a north-easterly direction in about a month (about 15 cm/s) in the face of northerly winds of about 8 m/s which would cause a *south-westerly* drift of about 15 cm/s (using the generally accepted rule-of thumb that ice drifts at about 2% of the wind speed at about 20° to the right of geostrophic winds [*Gow and Tucker*, 1990] or 40° to the right of surface winds [*McPhee*, 1990]). Surface currents in this region are not well known, but the wind driven model of *Legutke* [1991] shows mean currents at a depth of 37m to be less than 5 cm/s towards south-east. Finally, there seems to be a net increase in salinity in this region between November 1988 and February 1989, consistent with the formation of about 50 cm of ice with a bulk salinity of 7 [*GSP Group*, 1990]. Although the formation of ice would result in a release of latent heat (the approximate magnitude of this release is indicated in figure 5), the corrected heat fluxes and the heat content time series are not accurate enough to allow measurement of this number. Most of this ice will probably be formed in December during the time when the ice edge is advancing. Assuming a slab-like mixed layer above a deeper water with a salinity of 34.89, we find that the November surface salinity of 34.65 will increase by about 0.07 due to brine rejection from ice formation. This does not eliminate the density jump across the base of the mixed layer, but does reduce it from about 0.1 to about 0.06 σ units.

In spite of the density gradient between the mixed layer and the underlying AIW, the mixed layer continues to deepen after November, reaching depths of about 150-200m by the end of January (this can also be seen in the thermistor string data reproduced in figure 7-7a and b), presumably due to turbulent entrainment processes. Using the quasi-steady state bulk Richardson number scaling for stress-driven entrainment [*Price*, 1979]

$$R_v = \frac{g\delta\rho h}{\rho_0 V^2} \approx 1 \tag{7.6}$$

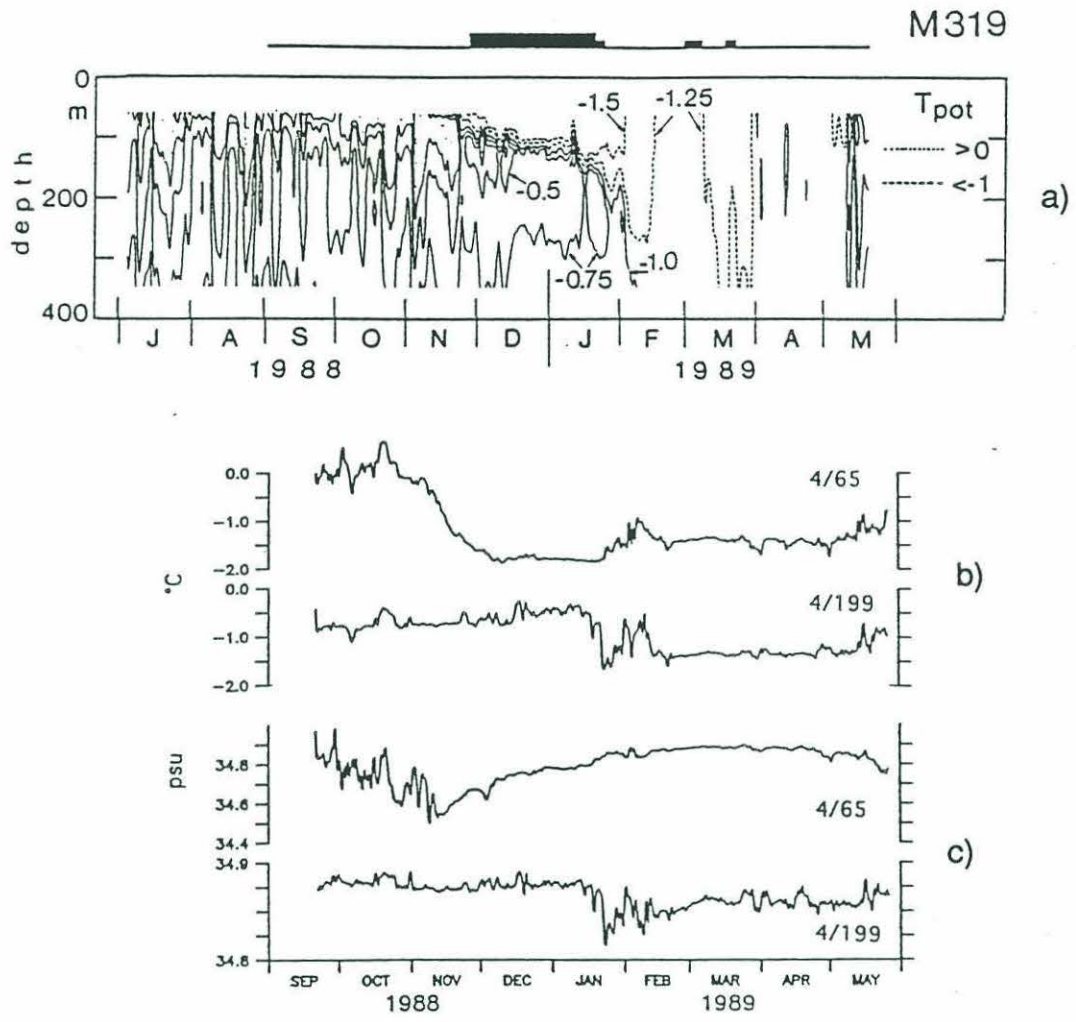

Figure 7-7: Time series of temperature and salinity in the mixed layer. a) Contour plot of thermistor records from mooring M319 about 60km to the west of mooring 6 [*Schott et al.*, 1993]. b) Temperature records at 65m and 199m, and c) Salinity records at the same depths from mooring 6 (adapted from *Roach et al.* [1993], in which work this mooring is numbered 4).

where $\delta\rho$ is the density jump and V the vertical shear across the base of a mixed layer of thickness h, we find that the vertical shear V must be of order

$$V \approx \sqrt{\frac{g\delta\rho h}{\rho_0 R_v}} \approx \sqrt{\frac{10 \cdot 0.06 \cdot 100}{1028 \cdot 1}} \approx 0.25 m/s \tag{7.7}$$

to drive entrainment. This is plausible for inertial motions. Entrainment will increase the mixed layer salinity to about 34.83-34.86, and consequently the density difference will vanish. Salinity changes of this magnitude are seen in a time series of measured at 65m at mooring 6 (figure 7-7c).

Thus it seems likely that ice is being formed locally, and blown to the southwest, resulting in a net export of fresh water from the array region. This fresh water flux combined with wind-driven entrainment act to decrease the vertical stability of the mixed layer. The preconditioning phase will end when the surface waters become saline enough so that the density jump at the base of the mixed layer is removed, i.e. when the surface waters are at point A in figure 7-8. Because the waters below the mixed layer are much warmer, there will still be a temperature and salinity jump across the mixed layer base when this occurs. The question of whether or not wind driven entrainment alone could destabilize the water column is discussed in the next section.

Finally, note that ice formation probably takes place primarily near the ice edge, where the water is still ice free. The almost completely ice-covered region further to the southwest will be insulated from the atmosphere, and ice growth rates will be much smaller, making removal of the fresh anomaly more difficult. Surface waters immediately to the south are apparently much fresher (see chapter 3), which again means that removal of the fresh anomaly will take more time.

7.3 Deep Mixing phase

Once the density barrier has been removed, surface waters can mix easily with the warmer more saline AIW below. Mixed layer temperatures will immediately rise, possibly melting any remaining ice and certainly inhibiting subsequent formation. This marks the moment at which the schematic evolution of the surface waters shown on the T-S diagram of figure 7-8 changes from movement along the freezing curve towards point A to movement upwards and rightwards towards point B and at least initially towards the characteristics of the

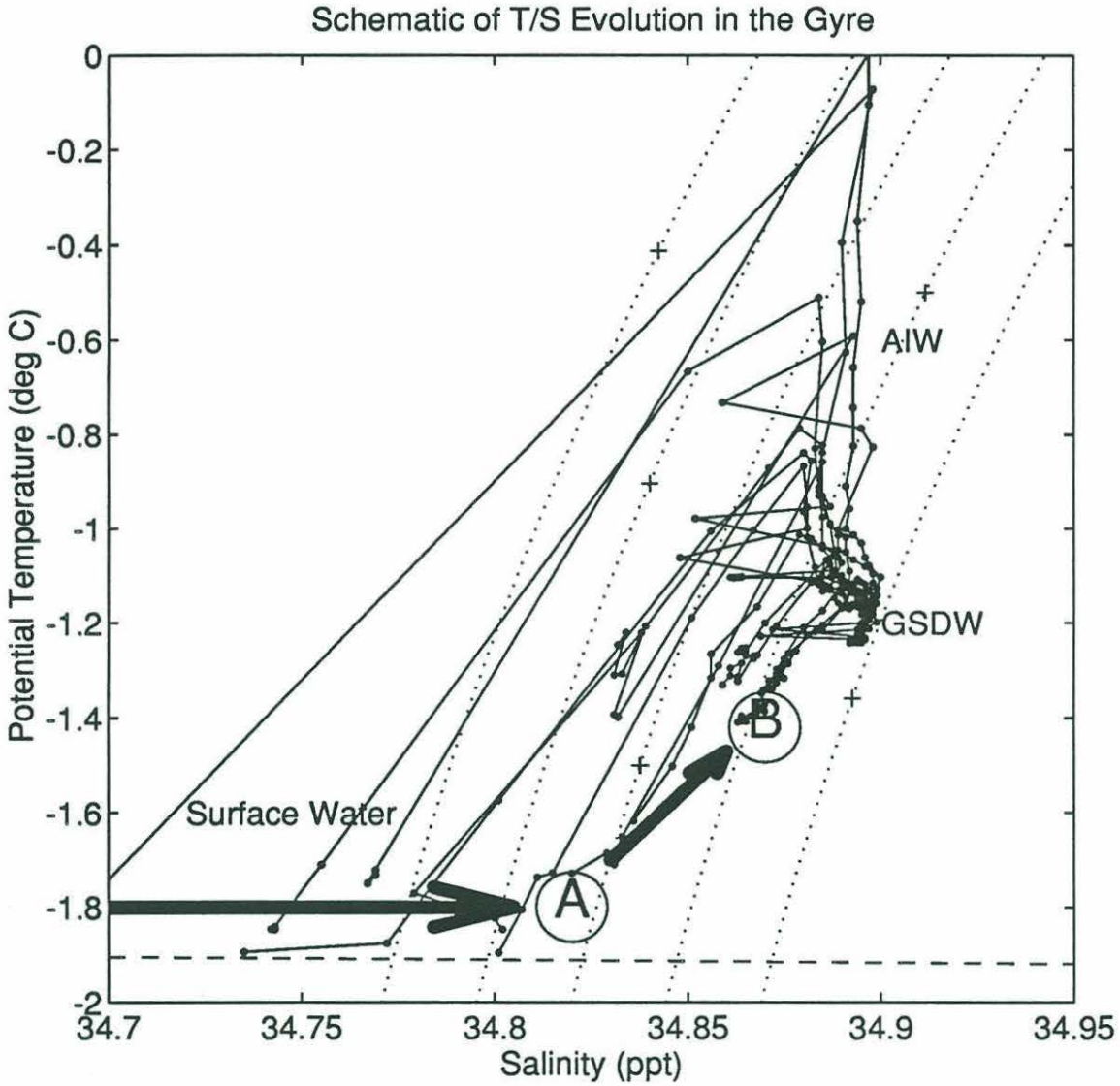

Figure 7-8: TS diagram showing schematically the evolution of the surface waters. In fall, the surface waters are fresh (33-34 psu) but cold ($\approx -1.8°C$), overlying warmer more saline Arctic Intermediate Water (AIW) which in turn overlies the colder Greenland Sea Deep Water (GSDW). Solid dots are T-S values from various winter bottle casts, and show different stages in the evolution. Through December and January, surface salinity gradually increases, until the density equals that of the AIW below (evolution towards point A). When the density jump has been eliminated, the mixed layer can rapidly warm and deepen by entraining AIW (evolution towards B). Surface temperatures are now too warm to allow the formation of ice, and surface heat losses further deepen the mixed layer.

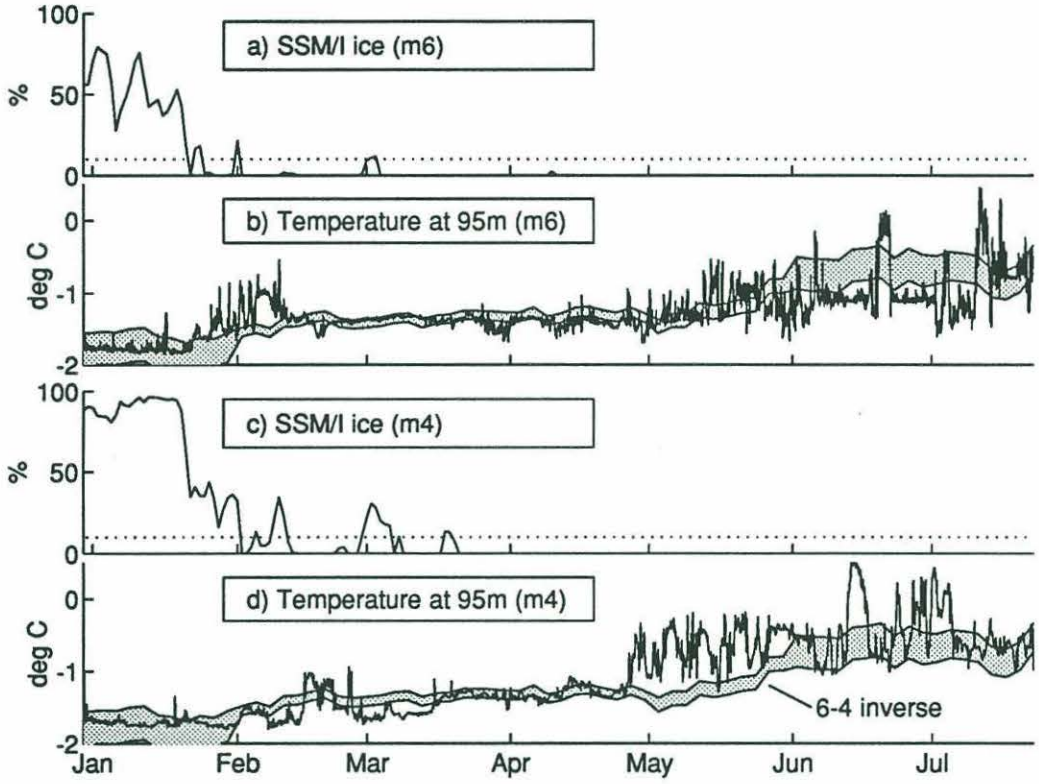

Figure 7-9: a) Ice concentration and b) Temperature records at 95m at mooring 6. c) Ice concentration and d) Temperature records at mooring 4. Ice "concentrations" below 10% (the dotted line in a and c) are not significantly different from open water. The shaded region in b and d represents the tomographic estimate of temperature at 95m for the 6-4 path and its uncertainty. Note the sudden rise in temperature at mooring 6 coinciding with the total disappearance of surface ice, in contrast to the step-like changes and recurring ice cover associated near-freezing temperatures seen at mooring 4 which is outside the deep mixing region.

deep water. However, the rate and direction of this movement will be determined by the balance between surface fluxes and the amount of warm underlying AIW being entrained, and hence will depend on the exact details of the temperature and salinity profiles and the surface fluxes and winds. Thermistor records at moorings 4 and 6 (see figure 7-9) show sudden temperature rises coincident with the disappearance of surface ice, but the subsequent evolution is different at each mooring.

At mooring 6 the change occurs around the beginning of February and is very well-defined. Following this rise, temperatures remain mostly constant as the surface forcing cools the warm water being continually entrained by mixed layer deepening. That is, the density continues to increase as salt is entrained, but the temperature does not necessarily vary. At mooring 4 the rise occurs in several steps interspersed by periods of ice formation, implying a slower deepening process in which overturning occurs in several steps, requiring brine rejection to destabilize the water column after each step. That is, there is an initial warming of the mixed layer at the beginning of February. However, the underlying stratification is strong enough that cooling alone will not further destabilize the water column, and so there is another period of ice formation in the second week of February. Finally, a third period of ice formation occurs at the beginning of March.

The tomographic results are more similar to the observations at mooring 6 than to those at mooring 4 during this period. In particular, the surface waters along this path are not cool enough to allow the formation of any more ice. A thermistor at 95m on mooring 3 (not shown) did not measure a sudden temperature rise at any time during the winter, consistent with the continual presence of ice at that location (see figure 7-6). At moorings 1 and 5 the thermistor records (figure 7-4a) did not show a sudden rise associated mixed layer deepening, but interpretation of those records is difficult due to the importance of advection at those sites.

Figure 7-6 shows that although the odden grows and decays several times in February-April, there always appears to be a hole or opening in the gyre center, roughly coincident with the 6-4 path. Although it cannot be stated unequivocally on the basis of the SSM/I data alone that ice formation in this opening is nonexistent (ice concentrations and/or thicknesses could merely be quite low) as was shown by the thermistor and tomographic temperature records the near-surface water is about 0.5°C too warm for that to occur. A similar ice free (but very foggy) region within the main pack was found during March 1982

(A. Clarke, pers. comm. 1993), suggesting that this is not an unusual occurrence. Since the surface stratification is weakest in this region (recall that the surface waters were least fresh at mooring 6 in the fall; see also chapter 3, figure 2 of *Clarke et al.* [1990], and figure 10 of *Carmack and Aagaard* [1973] for other years), the fresh anomaly will be removed earliest in this region, and the subsequent warming of the mixed layer will prevent further ice formation here while ice is still being formed in the surrounding waters. The long narrow bay known as *nordbukta* extends south-westwards from the array downwind from this warm pool, and is presumably a manifestation of the wind forcing. Ice being blown to the south-west will be continually replaced by fresh ice in the odden region, but is not replaced in the array region since the surface waters are too warm. The depth to which mixing will occur now depends on the amount of warm AIW. In the gyre center, near the top of the "dome" usually seen in temperature sections, the amount of AIW is least and the depth of mixing will reach a maximum. Indeed figures 7-3 and 7-4 indicate that the depth of mixing in the gyre center was almost double that seen at the northern edge, and that during the critical early March period when large negative fluxes exist over open water mixed layer depths near the 1-5 path were no deeper than 300m.

In contrast, *Killworth* [1979] found that the entire Weddell Gyre would overturn at about the same time, and thus he reasoned that upwelling inside eddies was necessary to preferentially precondition a small region for convection. We will use his quasi-static model to investigate the propensity of the gyre waters in 1988-89 to overturn. A brief summary of the model follows.

We begin with an initially ice-free profile $T(z)$ and $S(z)$. A mixed-layer depth h is specified, above which salinity S_m and potential temperature T_m are uniform. By assuming non-penetrative convection, we have

$$\rho(T_m, S_m, h) = \rho(T(h), S(h), h) \tag{7.8}$$

where $\rho(T, S, h)$ is the full, nonlinear, equation of state [*Millero et al.*, 1980]. Initially we choose S_m to be the mean salinity for depths less than h. We then solve (7.8) for T_m. If T_m is below the freezing point, we fix it at the freezing point and solve instead for the salinity S_m. The excess salt is assumed to come from the formation of a thickness δ of ice, which is

Station	Overturn	Q_0 (Jm^{-2})	ice	March depth	March depth	incremental
	-				fresh water export.	
1	300m-500m	2.4×10^9	0.4m	250m	700m	1100m
2	600m-B	3.5×10^9	0.8m	200m	200m	250m
3	900m-B	4.4×10^9	1.6m	200m	200m	250m
4	600m-B	3.8×10^9	1.1m	200m	200m	250m
5	150m-300m	2.1×10^9	0.4m	150m	500m	600m
6	500m-B	2.8×10^9	0.5m	250m	500m	1100m

Table 7.1: Results of the quasi-static model. Columns 2-5 show the depths affected by overturning, the heat loss required for overturn, the thickness of ice formed, and the mixed layer depth at the end of March (assuming heat losses of $2.0 \times 10^9 Jm^{-2}$ by that time) when no fresh water export occurs. A "B" signifies that the water column overturns to the bottom. Column 6 shows mixed layer depths at the end of March when up to 50cm of ice is removed from the surface. The last column shows mixed layer depths after heat losses of another 10%.

assumed to be about $\sigma = 30$ units fresher than the seawater. Thus

$$hS_m - \int_0^h S dz = \sigma\delta \tag{7.9}$$

Finally, we determine the heat loss to the atmosphere Q_0 through the conservation equation

$$hT_m - \int_0^h T dz = \frac{1}{\rho_0 c_p}[\rho_i L\delta - Q_0] \tag{7.10}$$

where ρ_0 and c_p are the mean density and heat capacity of seawater, ρ_i the density of ice, and L its latent heat. The above procedure is then repeated for all possible mixed layer depths, yielding a collection of points (Q_0, h).

This is the so-called *rapid* limit with least ice cover and shallowest mixed layer depth for a given heat loss, and corresponds well with the results of more sophisticated time-dependent models also discussed by *Killworth* [1979]. By comparing the heat loss Q_0 with the observed heat content time series in figure 7-1 we can compute a crude time scale. For example, by the end of January heat losses were 1×10^9 Jm^{-2}, and by the end February about 1.5×10^9 Jm^{-2}. At the end of March, heat losses reached about 2×10^9 Jm^{-2}. By searching the values of Q_0 found above, we infer the approximate mixed layer depth at those times.

The model was applied to the CTD profiles taken during the deployment in September

1988. In this discussion we will refer to the stations by the number of the mooring near which they were taken, but it is important to bear in mind that there is a mean southwestward flow in this region. Results are summarized in table 7.1. At all stations, ice was formed, roughly during the November/December period. Ice formation was least for stations 1, 5 and 6, and greatest for station 3. The water column for stations 2, 3, 4, and 6 could overturn to the bottom, however the heat losses required to do so were somewhat greater than the observed seasonal changes. Station 6 is most susceptible to overturning, requiring a heat loss of only 2.8×10^9 Jm^{-2} to do so, but as was shown in figure 7-1 the water column heat content for the 6-4 path decreased by only 2.0×10^9 Jm^{-2} before April. Similar values were found for other paths. Station 5 overturns to only 300m, and Station 1 does not overturn at all, but rather has a mixed layer that continually deepens. Converting the heat losses into a time scale, we find that at all stations mixed layer depths at the end of January are about 50m, increasing to only about 200-300m by the end of March. Since there is no fresh water export in this model, the results are similar to those that could be attained with wind driven entrainment and surface cooling alone. It therefore seems unlikely that the water column could overturn in this way, since even if the mixed layer deepened to 500m it could only do so by remaining quite warm.

The predicted mixed layer depths do not match the observations very well. However, the effects of advection have not been included. In particular, the ice that forms when mixed layer depths are shallow eventually melts as warm water is upwelled, thus reducing the salinity and increasing the stability of the mixed layer. To investigate the effects of the fresh water export as ice is blown away, we increase the salt content of the mixed layer in the original profiles by the amount rejected in the formation of 50cm of ice (40cm at stations 1 and 5). For stations 2, 3 and 4 the heat loss required to overturn the water column is reduced, but is still far too great to allow overturning in 1988-89. Thus mixed layer depths are similar to those predicted without the removal of fresh water. Stations 1, 5 and 6 do not overturn, but the rate of mixed layer deepening at those stations increases greatly. By the end of March these stations have mixed layer depths of 700m, 500m, and 500m respectively. The rate of deepening is greatest for station 6 at this time. The loss of an additional $0.2 \times 10^9 Jm^{-2}$ increases mixed layer depths to 1100m for stations 1 and 6, but only to 600m at station 5. These values are still somewhat less than those actually observed (1500m). The quasi-static model will underestimate the maximum depth of convection because a)

the CTD stations may not have sampled the region most susceptible to overturn, b) the "rapid" limit is inherently a lower bound on the depth of mixing (an upper bound results when surface heat losses primarily form ice rather than cool the water column), and c) only non-penetrative convection is allowed. Although the amount of ice actually formed was not much different from that predicted by the model, sensitivity to this parameter can be large for deep mixed layers. For example, increasing the amount of ice formed (and removed) to 60cm at mooring 6 increases the March mixed layer depth from 500m to 800m. Penetrative convection will result in an erosion of the sharp gradients at the base of the mixed layer assumed here, also increasing the depth at which temperature and salinity changes can be observed.

It seems clear that although the fresh water export was found in the previous section to cause less than half of the observed winter salinity increase in the mixed layer, it is crucial in determining the overall depth of convection. The depth of convection also depends on the underlying stratification. Although the exact effects of advection are unknown, in general currents are towards the south and west which would bring stations 1 and 6 towards the 6-4 path.

For this reason, as well as for the reasons discussed previously, deep mixing is best seen in the 6-4 inverse. Figure 7-10 is an expanded view of figure 7-3 during the deep mixing phase (1-way travel-time series are used to get daily temperature profiles). Several striking events can be seen. Following a storm in the third week of February, the mixed layer (tracked using the $-1.17°C$ isotherm) deepens to about 400m (note that there is an uncertainty of order 100m in this value, and that this uncertainty at least doubles for depths of 1000m or more). Another period of prolonged heat loss at the beginning of March results in ice covering the endpoints of the 6-4 path, although not its center (see also figure 2), before disappearing on March 7th at which point deepening to approximately 900m is observed. During the next two storm events (March 17 and 25) similar deepening spikes are seen, reaching a maximum depth of about 1500m. The $\approx$1000m depth of the mixed layer on the 15-16th March is less than that seen in CTD observations near mooring 6 on those days, which showed maximum mixed layer depths of almost 1500m [*SIZEX Group*, 1989], probably due to the range-averaging nature of the inverse. A comparison of the inverse profile for the 16th of March with various point temperature profiles was shown in figure 5-9. Profiles are similar down to 700m. Below this depth, a remnant of the original AIW core (shown by

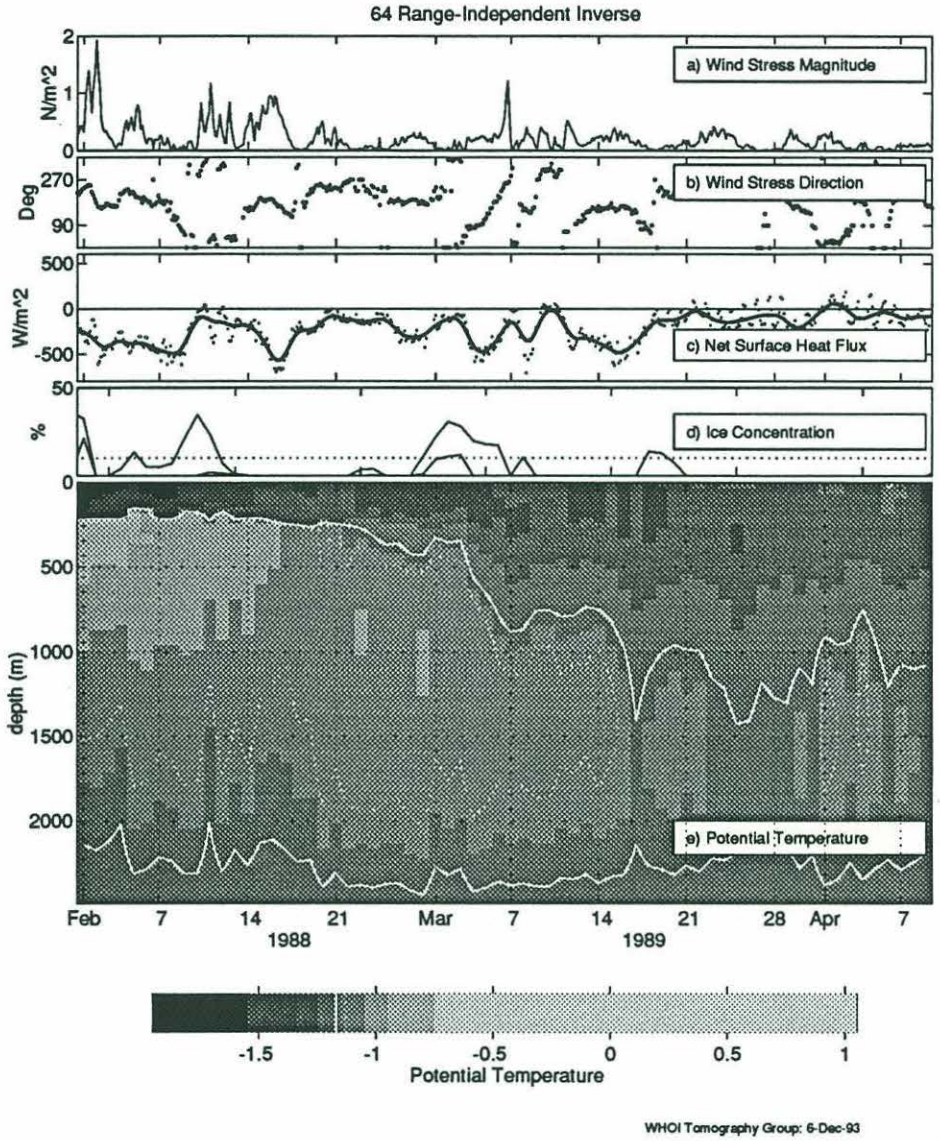

Figure 7-10: Deep Mixing along 6-4 path. a) Wind stress. b) Wind direction. c) Path-averaged net surface fluxes (a 3-day smoothed series is shown with a thick line). d) Ice concentration at endpoint moorings. Concentrations lower than the dotted line are not significantly different than open water. e) Daily range-average potential temperature profiles for the 6-4 path. Deep mixing seems to occur in discrete events in the third week of February and around the 7th, 17th, and 25th March. Inverse uncertainty is about $\pm 0.08°$ near the surface, $\pm 0.03°$C at 500m, and $\pm 0.015°$C at 1500m; isotherms may be in error by up to 200m vertically near 1000m. White contour lines are drawn at $-1.13°$C and $-1.17°$C.

the dashed profile which was observed on the 27th of February along the 3-4 path) is still visible in profiles that were taken near the edges of the ice hole, however profiles along the eastern half of the 6-4 path which were well within this opening have been cooled to greater depths. The inverse thus provides a lower bound to the maximum depth of mixing. By March 28th the deepening appears to have ended. This coincides with a levelling off in the heat content series (figure 7-1).

Note that during this time the tomographically observed heat content changes are basically consistent with surface fluxes to within the error bounds (cf. figures 7-1 and 7-2). The deepening events are not well correlated with the presence of small amounts of surface ice. Although ice cover at mooring 4 increases and decreases before the deepening event of March 7th, this seems related more to conditions at the edges of the deep mixing region than to a general freezing/melting cycle (see figure 7-6).

Numerical studies [*Jones and Marshall*, 1993] and observations of deep convection in the Mediterranean [*Schott and Leaman*, 1991] suggest that convection takes place within small (diameter $<$ 1km) plumes that collectively homogenize a large-scale chimney whose horizontal scale can be estimated here from the size of the hole in the ice cover. Within each plume dense water sinks. Individual plumes are separated by larger regions of slower upwelling. There is little horizontal exchange with waters outside the chimney during convection. The tomographic observations measure mean properties through the chimney, but by comparison with point observations we can derive some statistics for these plumes. Figure 7-11 shows a comparison of temperature time series derived from the 6-4 inverse with those measured by deep thermistors on mooring 6 (adapted from *Schott et al.* [1993]). These thermistor records, in conjunction with ADCP current profiles, have been interpreted as showing thin plumes of diameter approximately 350m in which cold water with a temperature about 0.15°C lower than ambient is convecting downwards. The tomographic series show temperature decreases of about 0.03°C in 2 days at 1400m during each event, about double the predicted inverse uncertainty (decreases are smaller in the first event and larger in the second), and thus only marginally significant at that depth. Accepting the results at face value, and assuming that most of the path is within the chimney, this implies that plumes fill about 20% of the horizontal cross-sectional area of the chimney. More usually a plume separation distance is used to characterize the geometry of the convecting flow. Simply dividing the plume diameter by the areal fraction will result in an overestimate of

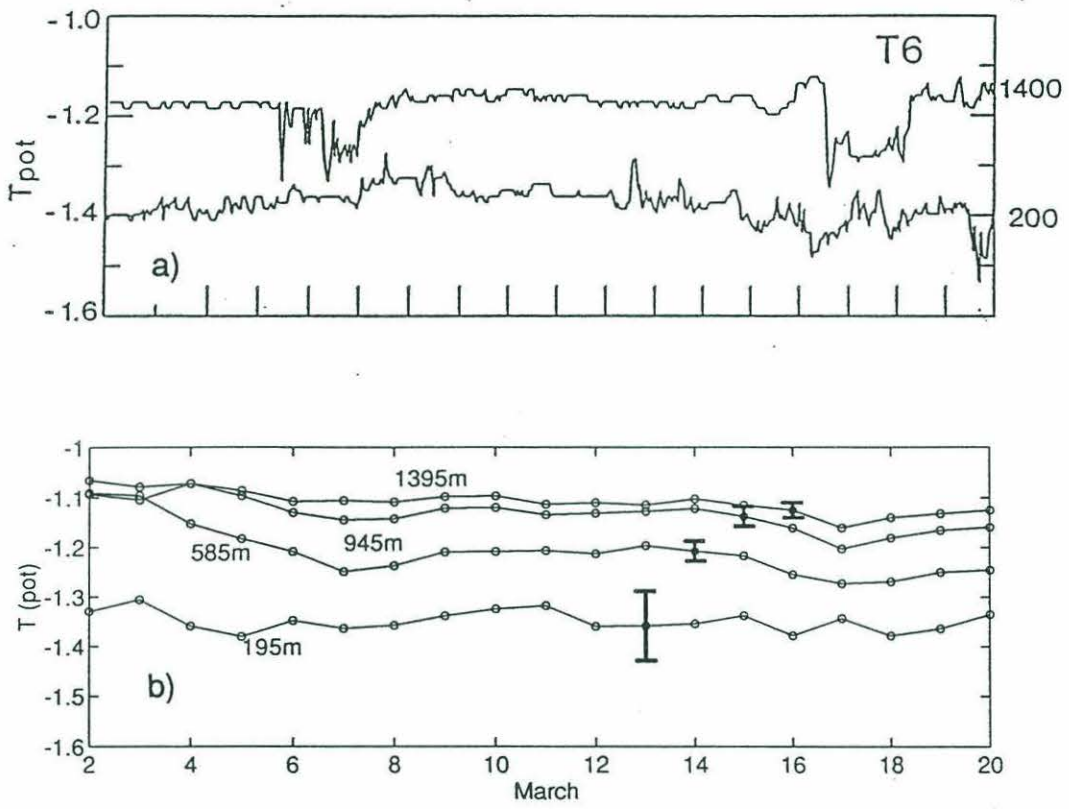

Figure 7-11: a) Thermistor records at 200m and 1400m on mooring 6 (adapted from *Schott et al.* [1993]) b) Daily temperature series from 6-4 one-way inverse at selected depths with estimated uncertainties (largely due to random errors). The deep events that can be seen in the thermistor record on March 6th and 17th also show up in the tomographic series, albeit with smaller magnitudes and more smoothly in time. Note that both series sample slightly different regions of the gyre.

this distance, since the acoustic path will not, in general, pass through a plume's nearest neighbours, nor will it invariably pass through plume centers. Assume for simplicity that the plumes have a hexagonal horizontal cross-section and are packed most efficiently at the vertices of a hexagonal grid. Then we find using geometrical arguments that the ratio of plume separation distance to plume diameter for an areal fraction of 0.20 is about $\sqrt{0.75/0.20} \approx 2$. Most reasonable geometries give similar ratios, so it is likely that this is a good description of the actual plume field. Thus plumes with diameters of order 350m are located at horizontal spacings of about 700m. Also note that since the depth of convection is of order 1400m, the ratio of plume separation to plume depth is ≈ 0.5, in good agreement with the values found in laboratory and numerical studies of rotating convection which are generally in the range 0.1–1 [*Boubnov and Golitsyn*, 1986; *Klinger and Marshall*, 1993], providing some independent confirmation of the correctness of the tomographic results.

The "spikey" appearance of the deepening events may indicate a partial adjustment of the chimney. During the 3 weeks in which the mixed layer depth increases from ≈400m to ≈1500m, we estimate a vertical velocity from the rate at which $-1.17°$ isotherm drops of about 0.5 mm/sec or 50 m/day (see figure 12). During the deepening events mean isotherms can drop at rates of order 2 mm/sec (200 m/day) near 1000m (compare with the vertical velocities of order 3 cm/sec inside plumes found by *Schott et al.* [1993]), although no measureable change seems to be occurring near the surface. More rapid sampling would be useful for future tomographic observations of deep convection.

7.4 Restratification phase

As soon as the large negative surface fluxes cease, the deep mixing period ends. We can better understand this period by examining heat content changes using equation (7.3). The heat residuals resulting from subtracting the surface heat loss from the tomographic heat contents for all paths are shown in figure 7-12. Also shown is an interpretation of these residuals, divided into periods when the residuals are level and heat advection is unimportant, and periods in which the residuals slope and significant heat transport is occurring. Note that in the following discussion heat fluxes (energy changes in the water column) are expressed per unit horizontal area, even when they refer to the effects of horizontal transport. Once again we emphasize that the heat flux and heat content time

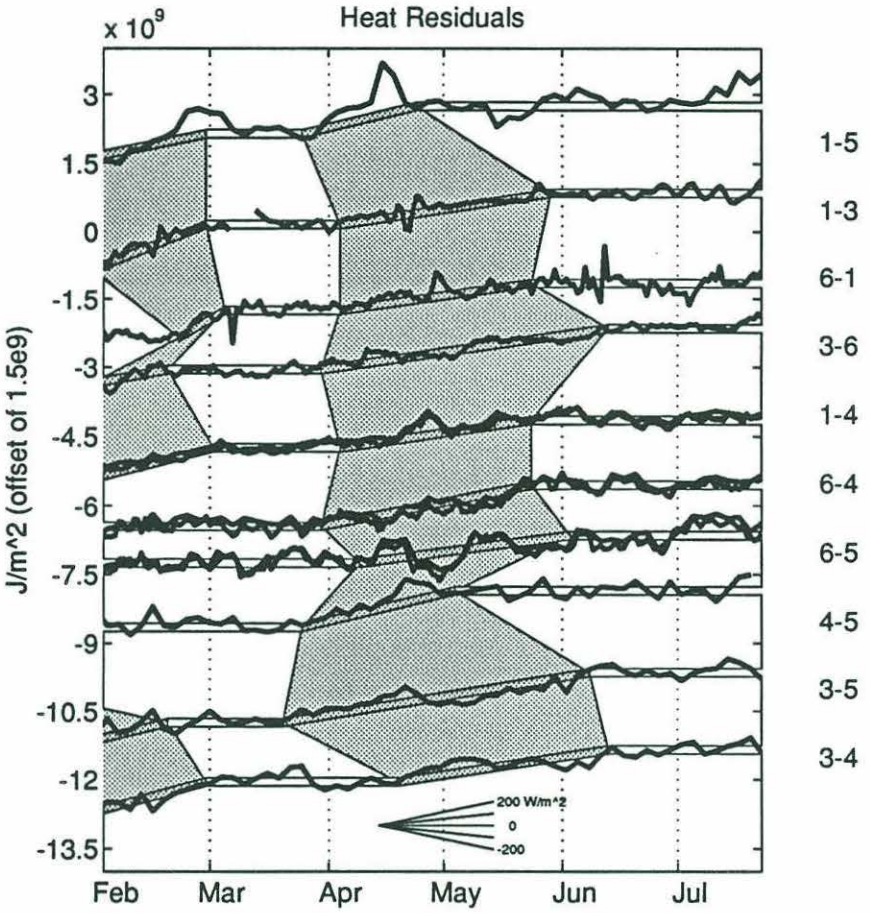

Figure 7-12: Heat residual series for all paths in 1989 (thin lines). Some paths have 2 lines, indicating daily (one-way) and 3-daily (two-way) inverses are being shown. Superimposed on these curves are sloped (grayshaded) and level (blank) bars indicating periods in which heat advection is and is not important respectively. The thickness of these bars indicates the tomographic heat content uncertainty of $\pm 9 \times 10^7$ Jm^{-2}. Biases in heat fluxes are estimated to be of order 50 Wm^{-2} and will result in slope errors. Equivalent fluxes for some slope values are indicated at the bottom of the figure.

series were computed entirely independently.

Horizontal heat advection occurs at two times in the period shown. During February there seems to be an inflow of warm water through the northern and eastern edges of the array. Presumably this is just a slight movement of the temperature dome in the direction of the prevailing currents. Following this, the residual series are level during March (the deep mixing period). Although surface waters everywhere are cooling, deep mixing (as discussed above) only occurs in the gyre center. Then there is a two month period in which about 10^9 Jm^{-2} enters the edges of the array region, implying an advective heat flux of about 200 Wm^{-2}, and at least double this for paths 4-5 and 1-5. Note that the change is quite rapid for the 4-5 and 1-5 paths, which are perpendicular to this inflow, whereas changes are much slower on paths more aligned with the inflow, and that the magnitude of these advective fluxes are much greater than the biases in the surface heat fluxes, which were estimated in Chapter 6 to be of order 50 Wm^{-2} on monthly timescales. During the restratification period, temperature profiles vary on short spatial and temporal scales. This spatial variability can also be seen in a closely-spaced CTD section through the Greenland Sea in June 1989 [*Budéus et al.*, 1993, figure 8]. It is well-known that a large homogenous chimney will become baroclinicly unstable and break up into a number of eddies [*Barnier et al.*, 1989; *Hermann and Owens*, 1991; *Legg and Marshall*, 1993], and this is presumably occurring here. Following this inflow, the residual series are again flat. This does not imply that eddy activity instantly ceases, merely that heat transported out of the array region by eddies is now being matched by that returned in other eddies. An large scale equilibrium in heat content has been reached so that the mean horizontal divergence of heat becomes insignificant. In fact, figure 7-2 shows an increased level of heat residual variability over the 6-4 path on time scales of less than one month from April onwards, compared with the generally smooth changes seen earlier. This is consistent with the existence of an eddy field. Thus mean water column warming from June onwards occurs entirely within the surface mixed layer and can be explained solely by local fluxes. However, one must be careful not to conclude that no advection is occurring. The seasonal climatology of the upper waters in the array region computed in chapter 3 shows that a freshening of the mixed layer usually occurs beginning in June and reaching a maximum in August/September. Thus the apparent absence of heat advection is due to small or non-existent horizontal gradients in the surface temperature field, or alternatively due to a large-scale homogeneity in the

surface fluxes which are primarily solar at this time.

7.5 Conclusions

The tomographic time series of temperature discussed here represent the first set of measurements resolving temporal aspects of the large-scale thermal evolution of the deep convection region of the Greenland Sea Gyre. The timing of this experiment was particularly fortunate, since wintertime convective activity in the Greenland Sea over the period 1986-1990 reached depths of 200m, 1300m, 1600m [*GSP Group*, 1990], and 250m [*Budéus et al.*, 1993], so that the tomographic observations took place during a maximum. Description of the tomographic series falls naturally into three periods: a preconditioning phase, in which the fresh surface waters are slowly salinated by entrainment and by brine rejected during local ice formation, a deep mixing phase in which local heat fluxes deepen the mixed layer to approximately 1500m in a collection of small plumes which partially homogenize surrounding waters to form a cold chimney under a region of low ice cover, and a restratification phase in which the cold chimney breaks up into a large number of eddies which transport the newly formed cold intermediate water away and replace it with the warm AIW. Mixed layer temperatures fall to the freezing point in the preconditioning period, rise sharply by about 0.5°C at the beginning of the deep mixing period, and thereafter slowly warm. Although this picture is not new, and similar ideas for various parts of this seasonal cycle have already been proposed [*Roach et al.*, 1993; *Schott et al.*, 1993; *Budéus et al.*, 1993], the tomographic observations are the first direct evidence for this behavior.

The large scale temperature changes in the gyre region can thus be explained solely by thermodynamic effects, without the necessity of introducing dynamical explanations for bringing AIW to the surface. Instead the surface waters are modified by the addition of salt through entrainment and brine rejected during ice formation until they match the density of the underlying AIW. However, the small-scale details of convection are not identified here - it is not possible to say whether or not thermobaric effects will be important in generating deep water (if for no other reason than that none seems to have been formed). Comparisons of the tomographic mean temperature changes with those measured by thermistors imply that downward-convecting plumes occupy about 20% of the horizontal area of the chimney in vertical cells whose horizontal/vertical aspect ratio (or plume separation to plume depth

ratio) is ≈ 0.5. Although this result has a large uncertainty since the tomographic changes are close to the margin of error, it in good agreement with the aspect ratios found in numerical and laboratory studies.

The local formation of ice and its removal by the wind are necessary to increase the salinity of the upper waters in December and January, since wind-driven mixed layer deepening alone cannot destabilize the water column. However once the density gradient has been eliminated the surface will remain largely ice free as heat mixed up from below will keep temperatures above the freezing point. Cycles of ice formation and melting do not seem to occur in the center of the deep mixing region, although they do appear around its periphery where the underlying stratification is stronger, and are linked with periods of large negative fluxes.

There are a number of important implications of this scenario. First, deep mixing does not occur early in the winter, underneath the ice that covers the whole Greenland Sea. Presumably this will depend to some extent on the amount of fresh water that enters the gyre in the previous summer. *Aagaard and Carmack* [1989] estimate that only about 3% of the fresh water in the East Greenland Current enters the convective region of the gyre. Such a small fraction can have large interannual changes. If too much fresh water enters the gyre, or the winter is not particularly severe, then the density gradient will not be eliminated early enough to allow deep mixing to occur before the surface fluxes change sign. The rate of deepening can further be affected by the amount of underlying AIW, which will depend on the strength of the cyclonic circulation, which in turn may depend on the mean wind stress curl over the Greenland Sea [*Meincke et al.*, 1992]. Thus the details of the ice cover on scales of 20km upwards may act as a proxy for the strength of deep convection. Because the ice-free region occurs inside the ice edge and can change rapidly, it is unlikely that ice charts made before the operational use of high-resolution satellite imagery became common will be accurate enough to reveal historical correlations; however this is a tool that can be used in the future.

Secondly, downward convection occurs in a series of very rapid events lasting only a few days, covering only a small percentage of the convective region before homogenizing with the neighbouring waters. Thus it will be difficult to observe these processes with conventional ship observations. During February and March of 1989 at least 2 different ships made observations in the array region, but each cruise missed a deepening event by

several days. Standard moorings can provide rapid sampling, but it is difficult to predict in advance the exact location in which deep mixing will occur. We demonstrate here that the areal coverage provided by tomographic methods is useful in locating deep mixing, however future tomographic experiments observing convection should be designed to resolve events lasting at most several days. It should also be noted that a complete homogenization of the mixed layer was not observed, and also that deep mixing does not appear to be linked directly to surface ice formation either on large scales as shown by the SSM/I data, or on smaller scales since the surface waters are about 0.5°C above the freezing point during March.

Thirdly, the presence of deep mixing is marked by spatial and temporal variability in the April-June period as the cold chimney breaks up into eddies. This variability can also be seen in closely-spaced CTD sections [*Budéus et al.*, 1993], and in variability of moored temperature records at intermediate depths in the gyre center (*Schott et al.* [1993]).

Chapter 8

Future Directions

In previous chapters we considered in detail the analysis of the Greenland Sea Tomography Experiment. To conclude this thesis, we will summarize the important results and outline a few of the broader research issues that can now be more profitably addressed in light of this understanding.

8.1 Summary of Important Results

An analysis of historical data was performed to determine the seasonal cycle of temperature and salinity in the Greenland Sea. Although the available data is scarce, and effects of interannual variability can not be completely removed, the results seem to be fairly robust and are useful as a baseline with which to compare observations for any particular year. By combining this climatology with the more detailed results from the Greenland Sea Tomography Experiment (chapters 4-7), we can describe the thermal evolution of the gyre in the following stages (dates are approximate):

Aug-Oct: Gyre surface salinity decreases due to the inflow of a thin layer of very fresh water, presumably meltwaters from the EGC.

Nov-Jan: The surface mixed layer cools to the freezing point, and ice begins to form, increasing the salinity of the mixed layer. Removal of ice by surface winds results in a net fresh water export from the gyre.

Feb-Mar: The surface mixed layer attains the density of the underlying AIW, and deep convection ensues. In spite of large surface heat losses, temperatures in the rapidly

deepening mixed layer rise due to the entrainment of the warm, salty AIW.

April-July: Incoming solar radiation forms a shallow warm mixed layer. Underneath this layer, AIW flows in to replace the products of the winter cooling.

Ice forms in the Greenland Sea Gyre because the surface waters are far too light to sink below the underlying AIW even when cooled to the freezing point. On the other hand, when this density barrier has been removed, mixing with lower waters will raise the temperature of the surface water above the freezing point so that the region of convection is ice free. The point at which the surface waters attain the density of the underlying AIW is marked by a sudden temperature rise, and is associated with the sudden disappearance of the surface ice. The weak remaining stratification can sometimes be overcome purely by surface heat loss, and vigorous downward convection proceeds during periods of strong negative fluxes. These periods are not long enough to completely homogenize the convective region, so that standard oceanographic stations do not, in general, observe a well mixed chimney. In surrounding waters, where the underlying stratification is stronger, mixing will proceed in a step-like fashion, with cycles of ice formation and melting, and in the region of permanent ice the insulation provided by the surface ice cover appears to prevent any deepening at all.

Over much of the year, the changes in heat content in the gyre center occur solely in the mixed layer, and can be explained by purely local surface fluxes. The apparent contradiction with the earlier statement that a significant inflow of fresh water occurs in the summer can be explained by noting that the surface fluxes at this time (dominated by the incoming solar radiation) are similar over a wide geographical region. The exception occurs during the April-July restratification period. At this time the cold chimney formed by the deep convection becomes baroclinicly unstable and breaks up. Equivalently one can consider the restratification to occur via an eddy flux, which will produce a net convergence of heat for a period of about two months. After this period the large-scale statistics of the eddy field are uniform over the entire region, so that no more mean warming effect can be measured, although fluctuations in heat content can still be seen.

We conclude that cooling of the AIW occurs during a brief winter period as a result of surface forcing alone. Characteristics of the surface waters are changed, allowing convection to proceed from the surface downwards. There is no reason to assume that dynamical

processes (for example, ice-edge upwelling), or complex advective/diffusive balances are necessary to cool the AIW. The short time scales of the forcing events (and the severity of the meteorological conditions at that time) makes observation of the convective events from ships unlikely - during March 1989 at least two different ships were working in this region; each missed a rapid deepening event by only a few days. On the other hand, the signature of mixing appears during the restratification as significant spatial or temporal variability in the temperature and salinity fields.

We now consider some of the questions raised by this analysis.

8.2 Convective Variability and Climate

As was illustrated by figure 3-10, there appears to be a correlation between the depth of convection and the details of the surface ice cover, at least during the 1980s. Convective depths were greater during the 1988-89 winter than in most of the rest of the decade (excepting possibly the 1983-84 winter). However, during 1988-89, convection was observed down to only about 1500m in the gyre center, and the modified waters were still not quite cold enough to replace the bottom water (excluding possible thermobaric effects as proposed by *Garwood* [1991]). In fact it is generally accepted on the basis of interpretations of transient tracer observations [*Schlosser et al.*, 1991; *Rhein*, 1991] that DWF did not occur to any great extent during the 1980s. Thus the applicability of these results to the general question of DWF can be questioned. To determine the plausibility of the scenario outlined above, we must consider climatic changes in all the factors governing convection. Unfortunately, questions about climate remain highly speculative due to the irregular nature, variable quality, and low availability of long oceanographic time series. However, the results presented in this thesis are not incompatible with the available data.

In figure 8-1a we have reproduced the time series of GSDW temperature originally discussed in Chapter 3. Making the not unreasonable assumption that the *density* structure has remained unchanged over this time (as was shown in chapter 3 the historical salinity data is not accurate enough to falsify this assumption), the variations in GSDW temperature will presumably be linked with salinity changes, which can be traced back through the source AIW and (eventually) to inflowing Atlantic Water (AW). If the AW becomes fresher, we might expect to see a colder GSDW. Conversely, a saltier AW might eventually appear as a

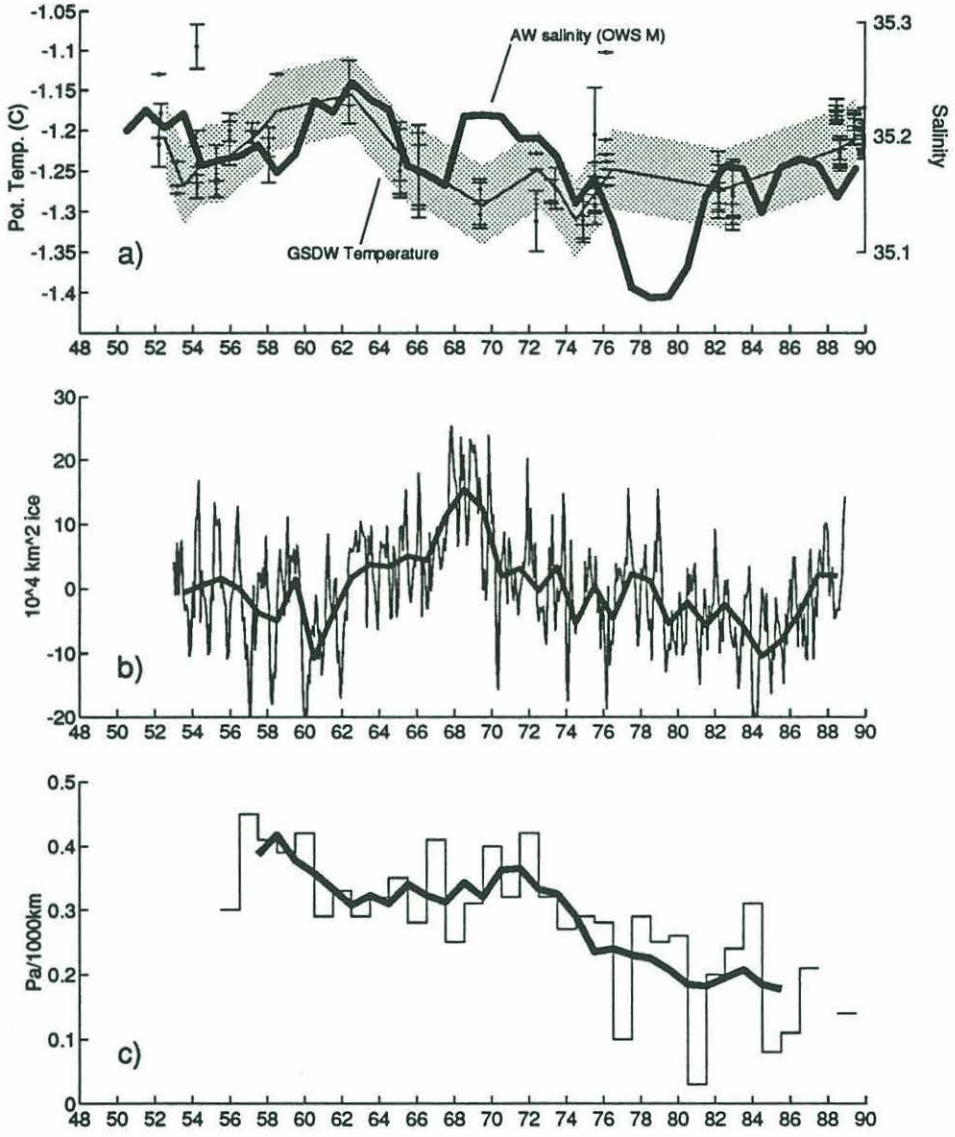

Figure 8-1: Climatic indicators in the Nordic Seas. a) GSDW temperature (error bars show actual data, shaded region links available yearly median values - see Chapter 3 for details). The thick solid line shows median yearly salinity in the upper 100m of the Norwegian Sea measured at Ocean Weather Station M, shifted by one year. b) Monthly (thin line) and yearly (thick line) anomalies of ice cover for the Greenland Sea. Note the all-time maximum in ice cover during 1968-1970, associated with the GSA. c) Mean annual wind stress curl over the Greenland Sea (after *Meincke et al.* [1992]). The thick line is 4 year running mean.

warmer GSDW. Although the required salinity variations in the GSDW are too small to be determined from the historical record, an excellent record of the inflowing Atlantic Water salinity is available from the 40 years of weekly stations taken at Ocean Weather Station (OWS) M in the Norwegian Sea (at approximately 65°N, 2°E). From this data a time series of yearly median salinity in the upper 100m was computed, and is shown superimposed on the GSDW temperature series. In order to account for the time taken for water to travel from OWS M to the bottom of the Greenland Sea during years of DWF, the salinity curve was shifted horizontally until the agreement was best. The resulting shift of one year can be taken as a crude estimate of the propagation time scale for salinity anomalies to travel from the weather station into the gyre deep water. This estimate is interesting, since it is similar to the propagation times of anomalies between OWS M and the waters off Svalbard found by other methods but several years less than the time taken before these anomalies appear in the EGC near 75°N [*Livingston et al.*, 1985; *Dickson et al.*, 1988], implying that the source of AIW in the Greenland Sea gyre may lie to the south of the Fram Strait. Also note that the vertical scale of OWS M salinity has been adjusted for best agreement - the salinity variations seen there are about 5 times larger than those needed to keep GSDW density constant.

The salinity curve overlies all available temperature measurements almost exactly, with two exceptions: 1969 and 1988-89, implying that during other times DWF was a regular occurence. During the period 1968-1972, the salinity time series would seem to predict GSDW temperatures of about -1.2°C. However, observations in 1969 show that temperatures were close to -1.3°C (a similar value was found in February of 1971 by *Malmberg* [1983][1]). This could occur if, for example, deep convection last took place in March 1967, and did not occur again until at least March of 1971. It was during *precisely* this period that areal coverage of ice in the Greenland Sea was at an all time maximum. Strong negative correlations between sea ice extent and surface salinity were found by *Marsden et al.* [1991] in the Iceland Sea. Figure 8-1b shows a time series of monthly and yearly areal anomalies of ice cover for the Greenland Sea computed by subtracting 36 year means from the Walsh dataset (see section 3.2 for a discussion of this ice product). The freshwater anomaly in the

[1]Although this paper concluded that convection to the bottom was seen, comparison of the published temperature, salinity, and oxygen profiles with those from the 1980s suggests that the depth of mixing was in fact somewhat less than 1000m.

EGC associated with southward passage of the "Great Salinity Anomaly" (GSA) [*Dickson et al.*, 1988; *Mysak et al.*, 1990] in 1968-1971, apparently results in gyre waters becoming extraordinarily fresh, increasing the ice cover and preventing convection during this time. Note that the return of the GSA in the late 1970s (visible in the time series of Atlantic Water salinity) may have resulted in a very cold GSDW (with potential temperatures of about $-1.4°C$) for several years, with temperatures returning to about $-1.3°$ in March of 1981. GSDW temperature was not measured during this period. However in 1901 the GSDW potential temperature was found to be $-1.39°C$ [*Aagaard*, 1968], and although the weather station data is of no help for this early date, a salinity time series of North Atlantic Water in the Faeroe-Shetland channel beginning in 1902 [*Dooley et al.*, 1984] indicates that the salinity of the inflowing Atlantic Water at that time was similar to that seen during the return of the GSA in the late 1970s.

Thus it seems likely that much of the change in GSDW temperature is not related to the intermittency of convection, rather it appears that (until the 1980s) convection happened during most winters and that the temperature changes are due merely to salinity changes in the source water.

It seems therefore that the fresh water "cap" can have a large influence on deep convection, and that the intermittency of this deep convection cannot be seen solely though examination of the GSDW temperature. Only about 3% of the fresh water in the EGC actually enters the gyre [*Aagaard and Carmack*, 1989]. Since changes in this amount can have drastic effects on convection, a better understanding of the fresh water transport across the East Greenland Front is needed in order to understand convective variability.

However, the statistics of the ice cover during the 1980s are very similar to those of the previous decades (excepting the GSA period), implying that the fresh water cycle of the gyre remains reasonably steady. Thus we cannot explain the cessation of DWF in 1980s through a possible excess of fresh water. As was discussed in chapter 7, the strength of the underlying stratification will determine whether or not surface cooling will mix rapidly downwards in convective plumes, or slowly in a series of steps requiring further buoyancy loss from ice formation to overcome successive density barriers. Thus the amount of AIW underneath the surface waters will presumably affect the depth of convection. If (in some large scale mean sense) the circulation in the Greenland Sea is cyclonic, then the amount of AIW in the gyre center will be related to the strength of the cyclonic circulation. Although

we have no direct measure of this strength, *if* one assumes that wind stress forcing is important in determining the gyre circulation, then the cessation of bottom water renewal could be linked to weaker winds. Indeed, figure 8-1c (adapted from *Meincke et al.* [1992]) shows that wind stress curl was much weaker during the 1980s then in the previous several decades. However, the understanding of this link is still at a very early stage and requires further work.

8.3 Convective Processes

As discussed in chapter 7, the tomographic results are consistent with deep mixing in a chimney occurring in a number of plumes in which dense water sinks downwards, rather than a wind-driven entrainment or a simple convective adjustment resulting in a well mixed mixed layer. However, there still remain some unknowns - in particular, the reason for the "spikiness" in the both the tomographic and thermistor temperature record (figures 7-10 and 7-11). These issues can probably be best addressed using numerical models, such as those of *Brugge et al.* [1991], in which transient forcing is applied over a stratified ocean. Observation of plumes in the ocean will be difficult using standard means, although new instruments (such as the subsurface autonomous torpedoes) may be useful in measuring the spatial parameters in a plume field. The necessity for thermobaric effects in the convection process has not yet been demonstrated, although an attempt to model tomographic observations (in particular the depth of convection) using the observed fluxes might help resolve this issue.

In 1988-89, the convective region, in which surface temperatures were about 0.5°C above freezing, was marked by a permanent "hole" in the surface ice cover, implying that brine rejection was not important in driving the deep convection itself (it is important only during the preconditioning). Although analyses of surface ice based on satellite measurements have been made since the early 1970s, they are generally in the form of monthly means in which these small scale details will be smoothed out. Re-analysis of this large data base to look for this signature of deep convection may be useful.

8.4 Acoustic Tomography

We conclude this thesis by discussing some technical aspects of the Greenland Sea Tomography Experiment. Perhaps most importantly, tomographic methods were successfully used to determine the evolution of ocean structure. Inverse estimates, consistent with the available CTD profiles and thermistor series, provided a time series of temperature profiles averaged over various regions that was not possible otherwise. Areal averages seemed to be particularly useful in reducing the effect of variations on small spatial scales, allowing a useful comparison with the spatially smooth surface heat fluxes.

However, as a workable technique tomography still has some shortcomings - in particular the low-power clocks need to be improved. Several instrument failures occurred. Although this did not seem to materially affect the analysis of the thermal evolution, it did adversely highlight the geometrical dependence of the number of paths on the number of instruments.

For the available power, the array was close to its optimal size. Signal-to-noise ratios on the longest paths in particular were low enough that array gains from beamforming and time averaging were necessary, and unfortunately this meant that a getting robust results with a rapid sampling time was not possible. The two day gaps in records from moorings 4 and 5 were a greater problem in analyzing the data since the actual convective events are very rapid, lasting a few days at most. Future tomographic experiments observing deep convection would find rapid sampling during the convective period to be useful. On the other hand, during the late summer and fall (i.e. June-December) changes to the thermal structure are quite steady and, unless one is interested in the details of the mixed-layer, sampling can be much more sparse. The biggest acoustic problems occurred during December-January, when near-surface propagation is greatly affected by the shallow cold mixed layer, although the deeper rays are largely unaffected. There seems to be no solution to this problem using standard tomographic methods which depend on a frequency-independent response over the signal bandwidth - broadband or full-wave methods must be used. For these purposes a more extensive vertical array may be useful.

Only range-average inverses were computed here. This is fairly simple to do in theory (although even this simplicity requires some effort to produce useful results), and this is helpful in testing the parameter space and analyzing the solutions, but has the drawback that range-dependence can sometimes obscure the details of the evolution - note that much

of this analysis relies on the results along *one* path. Although other paths were not all in interesting areas, the area-spanning nature of the tomographic array was useful since it allowed examination of the deep convection no matter where it occurred. The fully 3D inverse being constructed by W. Morawitz (SIO) could allow better determination of the size and evolution of the convective chimney.

Although not discussed in this thesis, reciprocal transmissions allow determination of along-track currents and vorticity. Analysis of this data might prove useful in identifying the source of the 50 day fluctuations in temperature profiles seen along the 1-5 path.

There are still some acoustical issues to be addressed. In particular the change in amplitude associated with the spring transition is rather interesting, since it appears linked to a change in the sign of surface fluxes. Further work should be done in order to determine whether this can be adequately explained by increased coupling losses from the base of the mixed-layer. Preliminary results seem encouraging.

Appendix A

Clock errors and their correction

Useful tomographic observations require estimates of travel-time accurate to within a few ms (the usual rule of thumb being a clock accuracy of about 1 ms). This requires extremely accurate clocks for long-term deployments - 1 ms in 1 year is an accuracy of 3 parts in 10^{11}. Clock time in currently used clocks is measured by counting vibrations of an oscillating crystal. The crystal nominally oscillates at some frequency f_o, but in reality oscillates at some $f = f_o + f_e$, with $f_e/f_o \sim 10^{-6} - 10^{-9}$ being the usual accuracy. Conceptually, we can can consider the "free-running" clock time $t_c(t)$ to be computed according to:

$$t_c = \int_0^t f/f_o dt \tag{A.1}$$

Thus clock time will drift away from the actual time. f_e can vary with ambient temperature in a non-trivial way, but will also change over time even at constant temperature ("ageing"). Ambient temperatures change on oceanic time scales, modified by the thermal inertia of the clock hardware. Little is usually known about the ageing characteristics of these clocks.

To generate sufficiently accurate times, some method of compensating for the error f_e must be used. In general there exists a tradeoff between accuracy and power consumption, which is dealt with in different ways in the two receiver designs used. The SIO receivers make periodic estimates $\hat{f}_e$ of the error by comparing f with a rubidium standard which is turned on only for short periods of time to save power (i.e. they actually compute f_e at time intervals which are small compared to the time scales on which f_e is presumed to change).

Then the actual time is computed according to:

$$t_c = \int_0^t f/f_o - \hat{f}_e/f_o dt \tag{A.2}$$

Although in practise there are some difficulties associated with the length of time between estimates $\hat{f}_e$, it will be assumed that these clocks keep "perfect" time in the following discussion.

However, the rubidium standards still require a lot of power even when run only periodically. The Webb receivers attempt to *infer* the error f_e by assuming it to be entirely temperature-dependent. Thus measurements of ambient temperature $H(t)$ are used in conjunction with a pre-deployment temperature/frequency calibration curve g to estimate f_e/f_o and perform corrections "on the fly". Conceptually we have

$$t_c = \int_0^t f/f_o + g(H)dt \tag{A.3}$$

(in practise the correction terms are computed at 10 second intervals rather than continuously). This strategy is used to build clocks with far lower power consumption. Clocks are embedded in a thermal mass with a time constant of 14 hours to reduce the effect of sudden temperature changes, which can cause a skew error in the corrections. In this experiment, the skew error due to the "thermal shock" of deployment was minimized by keeping the clocks on deck so that they had already adjusted to the near-freezing ambient temperatures before being synchronized (S. Liberatore, pers. comm. 1991), and is estimated at 0.05ms. Although the actual oscillator time constant was about 20 ± 4 minutes greater than that of the thermistor due to the packaging, it is estimated that this difference would cause an additional skew error of less than 0.03ms at all times during this deployment. Thus skew errors will be ignored. Any frequency bias remaining then appears (in theory) as a small linear drift in clock time, easily correctable using pre- and post- deployment synchronizations. It had been estimated before the experiment that a linear drift of about 100ms would occur.

In practise, a number of problems arose. On recovery of the instruments, it was discovered that the mooring 5 clock had drifted about 1.2s, an error of at least one order of magnitude greater than that expected. After examination of the acoustic data and a recalibration, it was found that the error was strongly temperature dependent - the result of a

problem in the original calibration which did not go to low enough temperatures and some unusually unsmooth temperature/frequency characteristics for this particular oscillator at low temperatures. The original and recalibration data are shown in figure A-1. Luckily, engineering measurements of clock parameters (including the thermistor readings $H(t)$) were stored at 12 hour intervals for the duration of the experiment. Using the recalibration and these stored engineering measurements, a "blind" clock correction was computed that accounted for almost 1s of the 1.2s drift.

The remaining errors in the mooring 5 clock and the errors in the mooring 4 clock were then examined using the travel-time *difference* series which are roughly proportional to along-track velocity and are sensitive to clock errors but quite insensitive to mooring motion errors. The travel-time differences can be bounded using *a priori* knowledge of the current magnitudes in the array region, from, e.g. the numerical model of *Legutke* [1991], and from the observations of *Schott et al.* [1993]. A simple linear drift correction to both clocks resulted in quite unbelievably large currents at some times during the year. The qualitative appearance of the difference series from all paths for which reciprocal time series were available suggested that superimposed on a frequency offset error (linear clock drift) was a small frequency variation due possibly to ageing of the oscillator crystals. Unfortunately almost nothing is known about the ageing characteristics of these clocks, although it is presumed to be "smooth".

Thus in order to compute a clock correction which would result in believable currents, it was necessary to assume some kind of "smooth" correction specified parametrically, and then use the travel-time difference series to estimate the unknown parameters in a fitting procedure. Since we do not know what the actual travel-time differences should be, there is a degree of arbitrariness to the computed corrections. Luckily we do have some current meter records at various locations, and these velocities (suitably resolved in the along-track direction) should have some resemblance to the travel-time difference series. The ageing error was parametrized as a low-order polynomial in time $A(t)$ and/or ambient temperature $T(H)$. It is *assumed* that these errors are additive, so that the remaining clock error can be written as:

$$c_e = A(t) + \int_0^t T(H)dt \tag{A.4}$$

with $c_e = 0$ at the pre-deployment synchronization. Unfortunately it was not possible

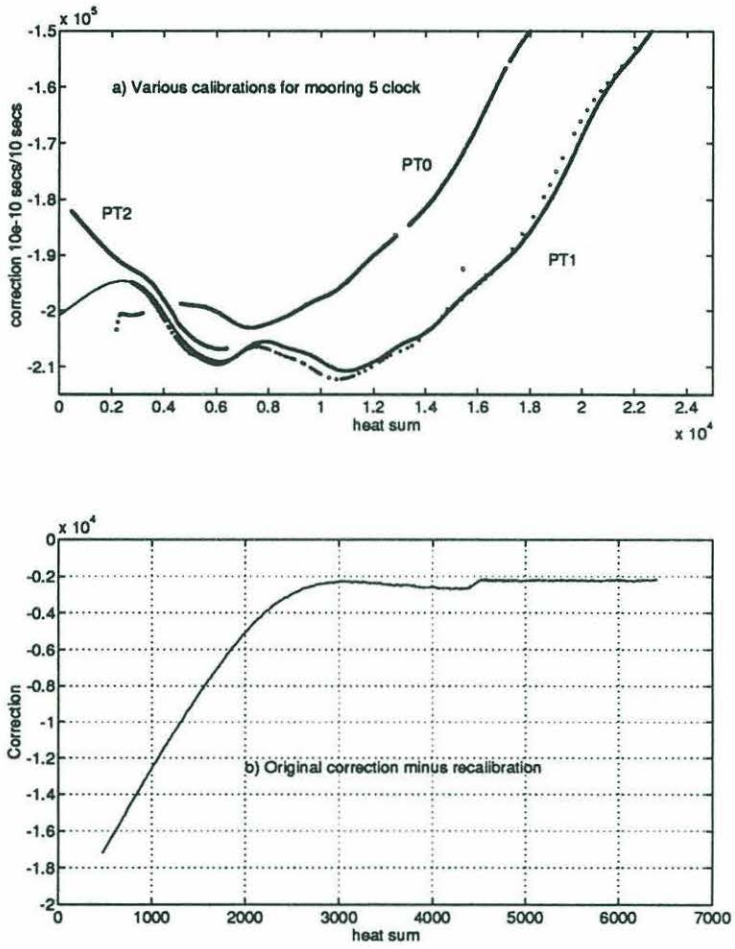

Figure A-1: Clock calibration data for mooring 5 clock. a) Clock correction in units of 10^{-10}secs/10secs as a function of "heat sum" (internal temperature units) measured during calibrations in May/87 (PT0), May/88 (PT1), and (at low temperatures only) May/91 (PT2). Note the similarity in shape of the curves. Changes in time are due to ageing. The predeployment calibration PT1 did not go to low enough temperatures, so the correction used (thin line) is extrapolated inappropriately b) Difference between the clock correction curve used in the mooring 5 clock and that found in PT1. The constant offset for heat sums greater than 4500 is due to ageing, the large errors for smaller heat sums are due to the bad original calibration

to use the post-deployment synchronization data as another constraint because $H(t)$ was not recorded for the last month of the experiment. For the mooring 5 clock, the temperature dependence was assumed to have been removed completely by the recalibration (note the constant differences in the curves at the right hand side of figure A.1b), so that the error was time dependent only. For the mooring 4 clock, it was not clear which error would be more important, thus corrections were computed with either time-dependence or temperature-dependence (but not both). Roughly speaking, the "smoothness" of the correction is inversely proportional to the number of unknown parameters being estimated, i.e. the polynomial order. As the polynomial order increases, the correction time series become wigglier, and it is more likely that variability in the travel-time series due to ocean processes is being ascribed to clock error. Thus one would prefer to use the lowest order correction that gives "reasonable" results (in terms of similarity between current meter records and travel-time differences).

Polynomial orders of 2, 3 and 4 were used. To determine the polynomial coefficients, a least-squares fit was performed by minimizing the variance of all of the resulting travel-time difference series about some unknown mean (i.e. modelling the velocities as a "mean plus white noise"), assuming that the clocks on moorings 1 and 6 were "perfect". Five reciprocal paths were used in the correction. As polynomial orders increased, the variance decreases since more of the "data" is classified as clock error. Figure A-2 shows the resulting corrections for all cases. The m5 corrections are all fairly similar and are somewhat parabolic in time implying a linear in time frequency drift (an attempt to model the remaining m5 error as a function of temperature resulted in abysmal results). Choosing the most correct form for the m4 errors was not as easy, but judging by qualitative agreement with current meter data using a 4th order $T(H)$ correction gave best results.

Errors in this correction are estimated by looking at the spread for all the possible corrections in figure A-2. The resulting correction is believed to be accurate within $\pm$1ms for scales of less than 1 week, and accurate to within $\pm$2ms for time scales of about 100 days.

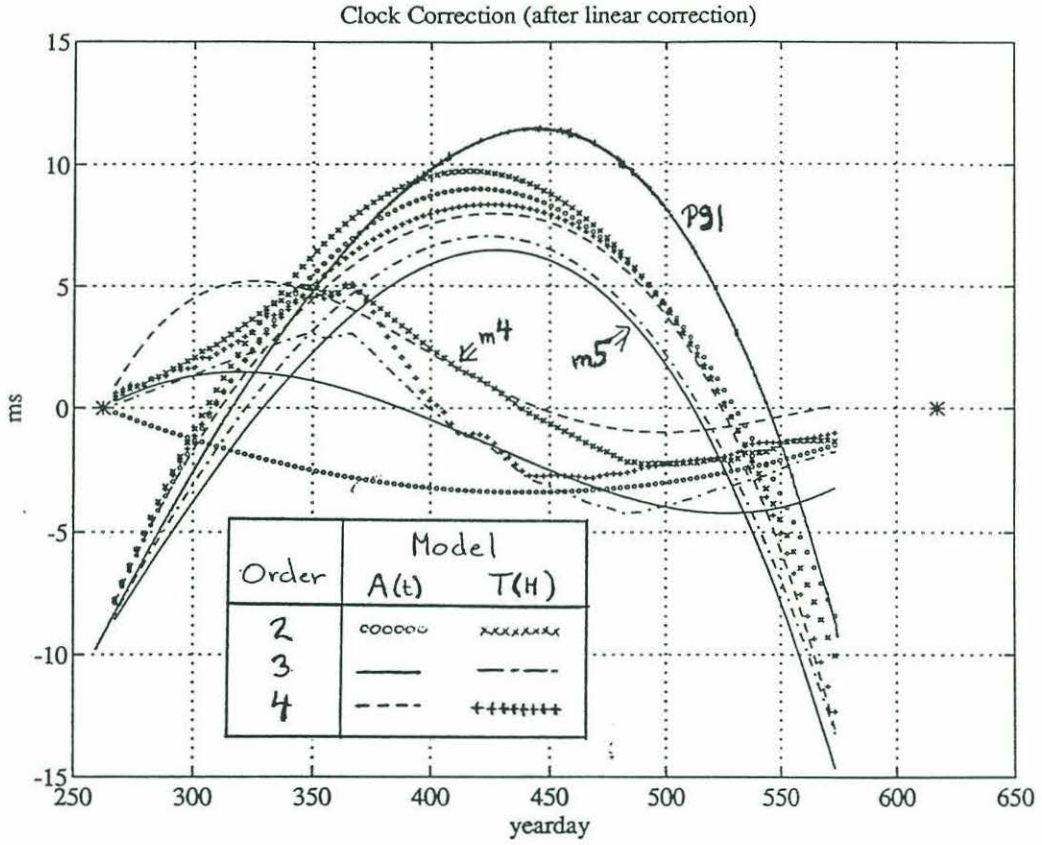

Figure A-2: A straight line drift of 98.56ms has been removed from the m4 corrections, and a drift of 312ms (with an offset of 10ms) was removed from the m5 correction. All m5 corrections are roughly parabolic, but the m4 corrections have a more complicated shape. The P91 curve represents an early attempt to correct the m5 clock using travel-time information from only the 4-5 path. Asterisks mark the deployment and recovery times.

Appendix B

Estimating currents using navigated moorings

The taut moorings used in the Greenland Sea Tomography Experiment were navigated using 3 or 4 element bottom transponder arrays. Rotary spectra of mooring motion exhibited peaks at the expected tidal frequencies, but the amplitudes of these peaks were inconsistent with predicted values for either velocities or displacements.

Here we develop a simple method by which currents can be estimated using the observations of mooring position relative to the anchor location. The response of the mooring to the current field is to lean in the direction of the current at low frequencies and to move with the water column at high frequencies. At tidal and inertial frequencies the response is a combination of the two effects, leading to the observed diagreement.

B.1 Theory

The mooring dynamics and notation are based on the simplified model of *Howe and Munk* [1988]. Since the drag elements on the taut moorings used for tomography are concentrated near the upper float, we assume a point drag element at the end of a straight mooring cable of length L anchored at the origin (with z positive upwards). Then there is a balance between the vertical buoyancy B and horizontal drag force $\mathbf{F}$:

$$B\mathbf{x} = \mathbf{F}z \tag{B.1}$$

where $\mathbf{x} = (x, y)$ is the horizontal displacement, and $x^2 + y^2 + z^2 = L^2$. Since $|\mathbf{x}| \ll L$, we have $z \approx L$. The depth below the surface to the drag elements, h_M, is also constant, and in this case is $\approx$ 75m. We use a quadratic drag law to model interactions with the ambient horizontal velocity field $\mathbf{u}$:

$$\mathbf{F} = k \cdot (\mathbf{u} - \dot{\mathbf{x}})|\mathbf{u} - \dot{\mathbf{x}}|, \quad \dot{\mathbf{x}} = \mathrm{d}\mathbf{x}/\mathrm{d}t \tag{B.2}$$

where k is a (dimensioned) drag coefficient. Now, we solve for $\mathbf{u}$ as a function of $\mathbf{x}$ by substituting (B.2) into (B.1) and recognizing that

$$|\mathbf{x}| = (kL/B)|\mathbf{u} - \dot{\mathbf{x}}|^2 \tag{B.3}$$

to find

$$\mathbf{u} = \frac{\mathbf{x}(B/kL)^{1/2}}{|\mathbf{x}|^{1/2}} + \dot{\mathbf{x}} \tag{B.4}$$

Mooring response will be determined by the partition between the displacement and velocity terms. Increasing the buoyancy or decreasing the drag and/or mooring length will "stiffen" the mooring and cause it to respond more by leaning in the direction of the currents than by moving with them. For the moorings considered here we use $kL/B = 7 \times 10^4 \mathrm{s}^2\mathrm{m}^{-1}$.

B.2 Mooring Response

Using (B.4) we compute the velocity at $h_M \approx$ 75m. The time derivative of mooring position was computed using Fourier transforms rather than centered differences. Using centered differences to estimate derivatives filtered frequencies greater than about 5 cpd quite severely.

Figure B-1 shows spectra of predicted velocity $\mathbf{u}$ and mooring velocity $\dot{\mathbf{x}}$ for one particular mooring. Also shown are the frequencies and amplitudes of predicted tidal velocities at this mooring (B. Gjevik, pers. comm.). The agreement between the computed and actual tidal velocities is quite good, keeping in mind that a tomographic determination of tidal velocities found that K1 tides were about 50% larger than predicted [*Worcester et al.*, 1993]. By far the dominant characteristic is the peak at inertial frequencies, which hides the nearby tidal components, but one can also see a smaller peak near the first harmonic. There also seems to be more energy at negative frequencies in general than at positive ones, although the reverse is true at the identifiable tidal frequencies.

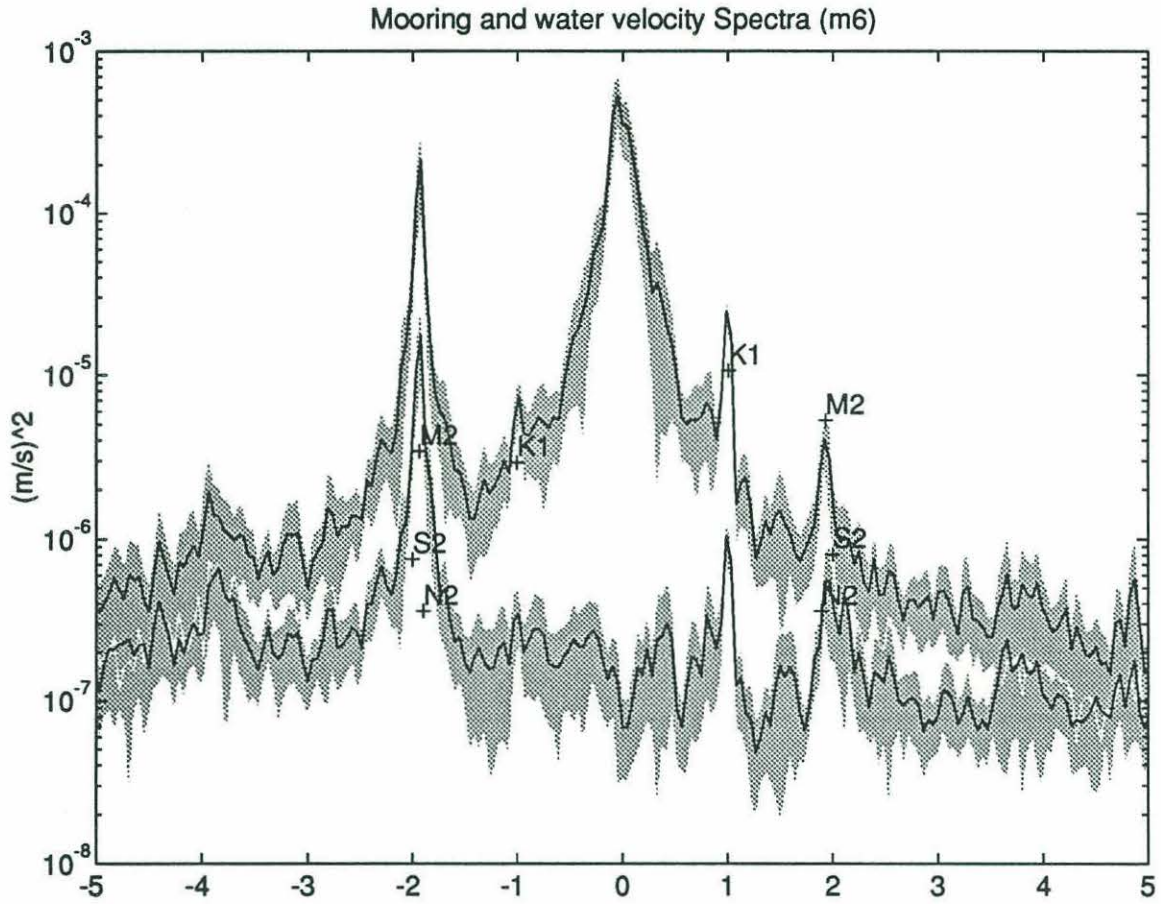

Figure B-1: Rotary spectrum of mooring 6 velocity computed from hourly observations (lower curve), and of water velocity (upper curve) computed from the mooring positions (see text). Shaded regions represent 95% confidence intervals for the spectral estimates. Normalization will show true amplitudes of tidal lines. Predictions of various tidal amplitudes are indicated by labelled crosses. $K1$ tides are about double the expected amplitude, while $M2$ peaks are approximately correct. The inertial peak near -1.93 cpd is a dominating feature of the spectra.

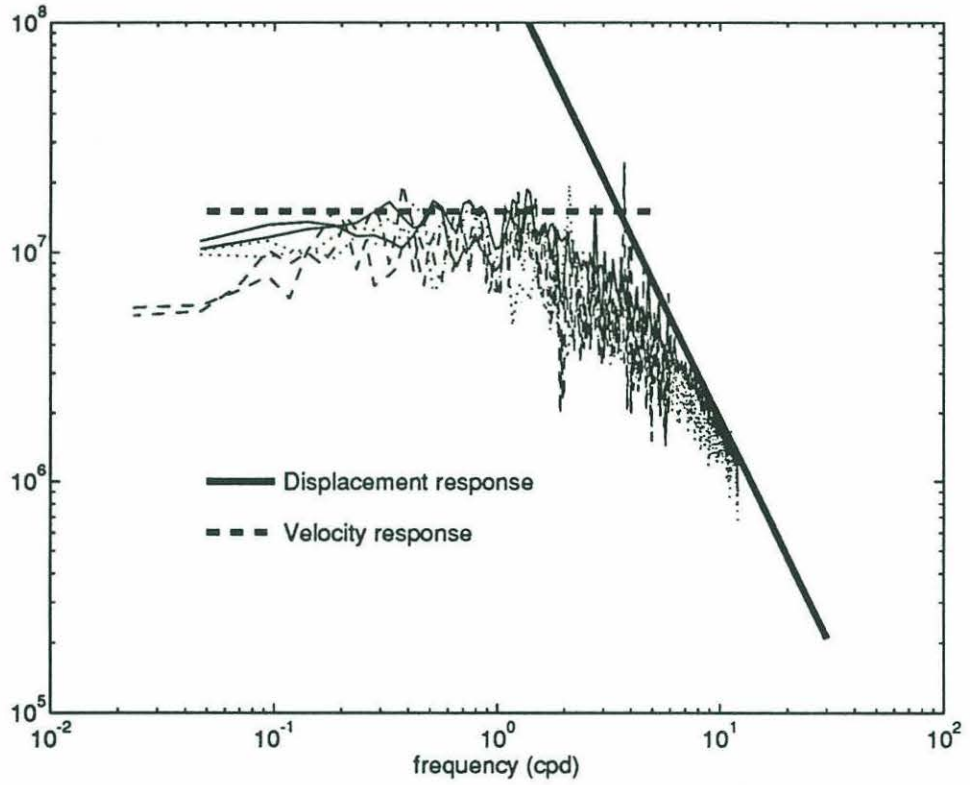

Figure B-2: Ratio of the mooring and water velocity power spectra for several moorings. The limiting cases of velocity and displacement responses are shown by the thick lines. Moorings respond primarily by leaning in the direction of the prevailing current at frequencies less than about 1.5 cpd, but move with the flow at frequencies greater than about 10 cpd. In the range of tidal and inertial frequencies, both factors are important.

The dominant response of the mooring to the observed spectrum of ocean currents can be investigated using the ratio of mooring position and water velocity power spectra. There are two limiting cases:

$$\text{displacement response} : \frac{|X(\omega)|}{|U(\omega)|} \sim \omega^{-1} \tag{B.5}$$

in which the mooring moves with the water particles, and

$$\text{velocity response} : \frac{|X(\omega)|}{|U(\omega)|} \sim C_o \tag{B.6}$$

in which the mooring leans in the direction of the currents. Figure B-2 shows this ratio for several different moorings from the Greenland Sea Tomography Experiment. For frequencies lower than about 1.5 cpd the mooring displacement is proportional to the water velocity, while for frequencies greater about 10 cycles per day the mooring displacement is proportional to water displacement. Near the tidal and inertial frequencies, the response is a mixture of the two. This implies that current meters will not sense the true currents at frequencies greater than about 1.5 cpd.

Appendix C

Glossary

ADCP	Acoustic Doppler Current Profiler
AIW	Arctic Intermediate Water
AODW	Arctic Ocean Deep Water
AW	Atlantic Water
CBDW	Canadian Basin Deep Water
CEAREX	Coordinated Eastern Arctic Experiment
DMSP	Defense Meteorological Satellite Program
DWF	Deep Water Formation
EBDW	Eurasian Basin Deep Water
EGC	East Greenland Current
GSA	"Great Salinity Anomaly"
GSDW	Greenland Sea Deep Water
IGY	International Geophysical Year
MIZ	Marginal Ice Zone
MLM	Mixed layer model
NADW	North Atlantic Deep Water
NSDW	Norwegian Sea Deep Water
OWS	Ocean Weather Station
SDB	Severely Damaged Brain
SIZEX	Seasonal Ice Zone Experiment
SSM/I	Special Sensor Microwave Imager
SST	Sea Surface Temperature
UKMO	United Kingdom Meteorological Office

Bibliography

Aagaard, K., Temperature Variations in the Greenland Sea deep-water, *Deep Sea Res., 15*, 281–296, 1968.

Aagaard, K., Wind-driven transports in the Greenland and Norwegian Seas, *Deep Sea Res., 17*, 281–291, 1970.

Aagaard, K. and E. C. Carmack, The Role of Sea ice and Other Fresh Water in the Arctic Circulation, *J. Geophys. Res., 94*, 14485–14498, 1989.

Aagaard, K., L. K. Coachman, and E. Carmack, On the halocline of the Arctic Ocean, *Deep Sea Res., 28*, 529–545, 1981.

Aagaard, K., J. H. Swift, and E. C. Carmack, Thermohaline Circulation in the Arctic Mediterranean Seas, *J. Geophys. Res., 90*, 4833–4846, 1985.

Alves, J. O. S., An Assessment of the surface fluxes from the Meteorological Office numerical weather prediction models. Part II: Heat and fresh water, *Meteorol. Mag., 121*, 59–83, 1992.

Anderson, D. L. T. and P. D. Killworth, Spin-up of a stratified ocean, with topography, *Deep Sea Res., 24*, 709–732, 1977.

Anderson, R. J., Wind Stress Measurements Over Rough Ice During the 1984 Marginal Ice Zone Experiment, *J. Geophys. Res., 92*, 6933–6941, 1987.

Bader, C. M., B. M. Howe, J. A. Mercer, P. F. Worcester, B. D. Cornuelle, and J. Lynch, CTD, XBT and XSV Data from the Greenland Sea: R/V *Knorr* Cruise 8809 (6 September - 4 October 1988) and R/V *Endeavor* Cruise EN200 (3 August - 10 September 1989), Technical Report APL-UW TM3–91, Applied Physics Laboratory, University of Washington, 1991.

Barnier, B., M. Crépon, and C. Le Provost, Horizontal Ocean Circulation Forced by Deep-Water Formation. Part II: A Quasi-geostrophic Simulation, *J. Phys. Oceanogr., 19*, 1794–1808, 1989.

Bell, R. S. and A. Dickinson, The Meteorological Office Operational Numerical Weather Prediction System, Scientific Paper 41, Her Majesty's Stationary Office, 1987.

Boubnov, B. M. and G. S. Golitsyn, Experimental study of convective structures in rotating fluids, *J. Fluid. Mech., 167*, 503–531, 1986.

Bourke, R. H., R. G. Paquette, and R. F. Blythe, The Jan Mayen Current of the Greenland Sea, *J. Geophys. Res., 97*, 7241–7250, 1992.

Bourke, R. H., R. G. Paquette, R. F. Blythe, and M. D. Stone, On the Deep and Bottom Waters of the Greenland Sea From Summer 1989 and 1990 Data, *J. Geophys. Res., 98*, 4629–4638, 1993.

Brekhovskikh, L. M. and Y. P. Lysanov, *Fundamentals of Ocean Acoustics* (2nd ed.). Springer-Verlag, Berlin, 1991.

Broecker, W. S., The Great Ocean Conveyor, *Oceanog., 4*, 79–89, 1991.

Brugge, R., H. L. Jones, and J. C. Marshall, Non-hydrostatic Ocean Modelling for Studies of Open-Ocean Convection, In *Deep Convection and Deep Water Formation in the Oceans*, edited by P. Chu and J. C. Gascard, pp. 325–340. Elsevier, Amsterdam, 1991.

Budéus, G., A. Maul, and G. Krause, Variability in the Greenland Sea as Revealed by a Repeated High Spatial Resolution Conductivity-Temperature-Depth Survey, *J. Geophys. Res., 98*, 9985–10,000, 1993.

Bullister, J. and R. Weiss, Anthropogenic Chlorofluoromethans in the Greenland and Norwegian Seas, *Science, 221*, 265–268, 1983.

Carmack, E. C. and K. Aagaard, On the Deep Water of the Greenland Sea, *Deep Sea Res., 20*, 687–715, 1973.

Casso, S. A. and H. D. Livingston, Radiocesium and Other Nuclides in the Norwegian-Greenland Seas 1981-1982, Technical Report Tech. Rep. WHOI-84-40, Woods Hole Oceanogr. Inst., Woods Hole, Mass., 1984.

Cavalieri, D. J., J. P. Crawford, M. R. Drinkwater, D. T. Eppler, L. D. Farmer, R. R. Jentz, and C. C. Wackermann, Aircraft Active and Passive Microwave Validation of Sea Ice Concentration From the Defense Meterological Satellite Program Special Sensor Microwave Imager, *J. Geophys. Res., 96*, 21,989–22,008, 1991.

Cavalieri, D. J., P. Gloersen, and W. J. Campbell, Determination of sea ice parameters with Nimbus-7 SMMR, *J. Geophys. Res., 89*, 5355–5369, 1984.

Chiu, C. S., J. F. Lynch, and O. M. Johannessen, Tomographic Resolution of Mesoscale Eddies in the Marginal Ice Zone: A Preliminary Study, *J. Geophys. Res., 92*, 6886–6902, 1987.

Clarke, R. A., J. H. Swift, J. L. Reid, and K. P. Koltermann, The Formation of Greenland Sea Deep Water: double diffusion or deep convection?, *Deep Sea Res., 37*, 1385–1424, 1990.

Clay, C. S. and H. Medwin, *Acoustical Oceanography.* John Wiley and Sons, N.Y., 1977.

Coachman, L. K. and K. Aagaard, Physical Oceanography of the Arctic and Subarctic Seas, In *Marine Geology and Oceanography of the Arctic Seas*, edited by Y. Herman, Chapter 1, pp. 1–72. Springer-Verlag, New York, 1974.

Comiso, J. C., Characteristics of Arctic winter sea ice from satellite multispectral microwave observations, *J. Geophys. Res., 91*, 975–994, 1986.

Comiso, J. C., S. F. Ackly, and A. L. Gordon, Antarctic sea ice microwave signatures and their correlation with in-situ ice observations, *J. Geophys. Res., 89*, 662–672, 1989.

Comiso, J. C. and C. W. Sullivan, Satellite microwave and in-situ observations of the Weddell Sea ice cover and its marginal ice zone, *J. Geophys. Res., 91*, 9663–9681, 1986.

Cornuelle, B. D., Simulations of acoustic tomography array performance with untracked or drifting sources and receivers, *J. Geophys. Res., 90*, 9079–9088, 1985.

Crépon, M., M. Boukthir, B. Barnier, and F. Aikmann, Horizontal Ocean Circulation Forced by Deep-Water Formation. Part I: An Analytical Study, *J. Phys. Oceanogr., 19*, 1781–1792, 1989.

Del Grosso, A New Equation for the speed of sound in Natural Waters, *J. Acoust. Soc. Am., 56*, 1084–1091, 1974.

Dickson, R. R., J. Meinke, S. Malmberg, and A. Lee, The "Great Salinity Anomaly" in the northern North Atlantic, 1968-1982, *Prog. Oceanogr., 20*, 103–151, 1988.

Dietrich, G., *Atlas of the Hydrography of the Northern North Atlantic Ocean.* International Council for the Exploration of the Seas, Copenhagen, 1969.

Dooley, H. D., J. H. A. Martin, and D. J. Ellett, Abnormal hydrographic conditions in the north-east Atlantic during the nineteen-seventies, *Rapp. Proc. Verb. Reun. Cons. Perm. Int. Explor. Mer, 185*, 179–187, 1984.

Esbensen, S. K. and Y. Kushnir, The heat budget of the global oceans: An atlas based on estimates from surface marine observations, Technical Report Report No. 29, Climate Research Institute, Oregon State University, 1981.

Fairall, C. W. and R. Markson, Mesoscale Variations in Surface Stress, Heat Fluxes, and Drag Coefficient in the Marginal Ice Zone During the 1983 Marginal Ice Zone Experiment, *J. Geophys. Res., 92*, 6921–6932, 1987.

Foldvik, A., K. Aagaard, and T. Tørresen, On the velocity field of the East Greenland Front, *Deep Sea Res., 35*, 1335–1354, 1988.

Garwood, R. A., Enhancements to Depp Turbulent Entrainment, In *Deep Convection and Deep Water Formation in the Oceans*, edited by P. Chu and J. C. Gascard, pp. 197–213. Elsevier, Amsterdam, 1991.

Gill, A. E., J. M. Smith, R. P. Cleaver, R. Hide, and P. R. Jonas, The Vortex Created by Mass Transfer Between Layers of a Rotating Fluid, *Geophys. and Astrophys. Fluid. Dyn., 12*, 195–220, 1979.

Gloersen, P. and D. J. Cavalieri, Reduction of Weather Effects in the Calculation of Sea Ice Concentration from Microwave Radiances, *J. Geophys. Res., 91*, 3913–3919, 1986.

Goncharov, V. V. and A. G. Voronovich, An experiment on matched-field acoustic tomography with continuous wave signals in the Norway Sea, *J. Acoust. Soc. Am., 93*, 1873–1881, 1993.

Gorshkov, S. G. (Ed.), *Arctic Ocean*, Volume 3 of *World Ocean Atlas.* Pergammon Press, New York, 1983.

Gow, A. J. and W. B. Tucker, Sea Ice in the Polar Regions, In *Polar Oceanography Part A: Physical Science*, edited by W. O. Smith, Chapter 2, pp. 47–122. Academic Press, San Diego, 1990.

Grenfell, T. C., D. J. Cavalieri, J. C. Comiso, M. R. Drinkwater, R. G. Onstott, I. Rubenstein, K. Steffen, and D. P. Winebrenner, Considerations for Microwave Remote Sensing of Thin Sea Ice, In *Microwave Remote Sensing of Sea Ice*, edited by F. D. Carsey, Volume 68 of *Geophysical Monograph*, Chapter 14, pp. 291–301. American Geophysical Union, Washington, 1992.

GSP Group, Greenland Sea project: A Venture Toward Improved Understanding of the Oceans' Role in Climate, *Eos, 71*, 750–751, 754–755, 1990.

Guest, P. S. and K. L. Davidson, The Effect of Observed Ice Conditions on the Drag Coefficient in the Summer East Greenland Sea Marginal Ice Zone, *J. Geophys. Res.*, *92*, 6943–6954, 1987.

Guest, P. S. and K. L. Davidson, Meterological Triggers for Deep Convection in the Greenland Sea, In *Deep Convection and Deep Water Formation in the Oceans*, edited by P. Chu and J. C. Gascard, pp. 369–376. Elsevier, Amsterdam, 1991.

Guthrie, K. M. and C. T. Tindle, Ray Effects in the Normal Mode Approach to Underwater Acoustics, *J. Sound Vib.*, *76*, 403–413, 1976.

Häkkinen, S. and D. Cavalieri, A Study of Oceanic Surface Heat Fluxes in the Greenland, Norwegian, and Barents Seas, *J. Geophys. Res.*, *94*, 6145–6157, 1989.

Häkkinen, S., G. L. Mellor, and L. H. Kantha, Modelling Deep Convection in the Greenland Sea, *J. Geophys. Res.*, *97*, 5389–5408, 1992.

Hermann, A. J. and W. B. Owens, Modelling the Geostropic Adjustment and Spreading of Waters Formed by Deep Convection, In *Deep Convection and Deep Water Formation in the Oceans*, edited by P. Chu and J. C. Gascard, pp. 283–308. Elsevier, Amsterdam, 1991.

Hogg, N. G. and H. M. Stommel, Hetonic Explosions: The Breakup and Spread of Warm Pools as Explained by Baroclinic Point Vortices, *J. Atmos. Sci.*, *42*, 1465–1476, 1985.

Hopkins, T. S., The GIN Sea — A Synthesis of its physical oceanography and literature review 1972–1985, *Earth-Sci. Rev.*, *30*, 175–318, 1991.

Howe, B. M. and W. M. Munk, Deep-sea moorings in a tidal current, *Deep Sea Res.*, *35*, 111–119, 1988.

Howe, B. M., P. F. Worcester, and R. C. Spindel, Ocean Acoustic Tomography: Mesoscale Velocity, *J. Geophys. Res.*, *92*, 3785–3805, 1987.

Hurdle, B. G. (Ed.), *The Nordic Seas*. Springer-Verlag, New York, 1986.

Jin, G., J. F. Lynch, R. Pawlowicz, and P. Wadhams, Effects of Sea Ice Cover on Acoustic Ray Travel Times, With Applications to the Greenland Sea Tomography Experiment, *J. Acoust. Soc. Am.*, *94*, 1044–1057, 1993.

Jin, G., J. F. Lynch, R. Pawlowicz, and P. Worcester, Acoustic Scattering Losses in the Greenland Sea Marginal Ice Zone during the 1988-1989 Tomography Experiment, *J. Acoust. Soc. Am.*, (submitted), 1994.

Johannessen, O., Brief Overview of the Physical Oceanography, In *The Nordic Seas*, edited by B. G. Hurdle, Chapter 3, pp. 103–127. Springer-Verlag, New York, 1986.

Johannessen, O. M., S. Sandven, and J. A. Johannessen, Eddy-Related Winter Convection in the Boreas Basin, In *Deep Convection and Deep Water Formation in the Oceans*, edited by P. Chu and J. C. Gascard, pp. 87–106. Elsevier, Amsterdam, 1991.

Jones, H. and J. Marshall, Convection with Rotation in a Neutral Ocean: A Study of Open-Ocean Deep Convection, *J. Phys. Oceanogr.*, *23*, 1009–1039, 1993.

Jónsson, S., Seasonal and Interannual Variability of Wind Stress Curl over the Nordic Seas, *J. Geophys. Res.*, *96*, 2649–2659, 1991.

Kent, E. C., B. S. Truscott, P. K. Taylor, and J. S. Hopkins, The Accuracy of Ship's Meteorological Observations: Results of the VSOP-NA, Marine Meteorology and Re-

lated Oceanographic Activities Report No. 26 WMO/TD-No.–455, World Met. Org., 1991.

Killworth, P., On "Chimney" Formations in the Ocean, *J. Phys. Oceanogr., 9*, 531–554, 1979.

Kleiner, B. and T. E. Graedel, Exploratory Data Analysis in the Geophysical Sciences, *Rev. Geophys. and Space Phys., 18*, 699–717, 1980.

Klinger, B. A. and J. Marshall, Regimes and Scaling Laws for Rotating Deep Convection in the Ocean, pp. (in preparation), 1993.

Lazier, J. R. N., Oceanographic Conditions at Ocean Weather Station *Bravo*, 1964–1974, *Atmosphere-Ocean, 18*, 227–238, 1980.

Legg, S. and J. Marshall, A Heton Model of the Spreading of Open-Ocean Deep Convection, *J. Phys. Oceanogr., 23*, 1040–1056, 1993.

Legutke, S., A Numerical Investigation of the Circulation of the Greenland and Norwegian Seas, *J. Phys. Oceanogr., 21*, 118–148, 1991.

Livingston, H. D., J. H. Swift, and H. G. Ostlund, Artificial Radionuclide Tracer Supply to the Denmark Strait Overflow Between 1972 and 1981, *J. Geophys. Res., 90*, 6971–6982, 1985.

Lynch, J. F., H. X. Wu, R. Pawlowicz, P. F. Worcester, R. E. Keenan, H. C. Graber, O. M. Johannessen, P. Wadhams, and R. A. Shuchmann, Ambient Noise Measurements in the 200-300 Hz band From the Greenland Sea Tomography Experiment, *J. Acoust. Soc. Am., 94*, 1015–1033, 1993.

Malmberg, S.-A., Hydrographic Investigations in the Iceland and Greenland Seas of late Winter 1971 - "Deep Water Project", *Jökull, 33*, 133–140, 1983.

Marsden, R. F., L. A. Mysak, and R. A. Myers, Evidence for Stability Enhancement of Sea Ice in the Greenland and Labrador Seas, *J. Geophys. Res., 96*, 4783–4789, 1991.

McDonald, N. R., Flows caused by mass forcing in a stratified ocean, *Deep Sea Res., 39*, 1767–1790, 1992.

McDougall, T. J., Greenland Sea Bottom Water Formation: A Balance Between Advection and Double Diffusion, *Deep Sea Res., 30*, 1109–1117, 1983.

McPhee, M. G., Small-Scale Processes, In *Polar Oceanography Part A: Physical Science*, edited by W. O. Smith, Chapter 6, pp. 287–334. Academic Press, San Diego, 1990.

MEDOC Group, Observations of formation of deep water in the Mediterranean Sea, *Nature, 227*, 1037–1040, 1970.

Meincke, J., S. Jónnson, and J. H. Swift, Variability of convective conditions in the Greenland Sea, *ICES mar. Sci. Symp., 195*, 32–39, 1992.

Mercer, J. A. and J. R. Booker, Long-Range Propagation of Sound Through Oceanic Mesoscale Structures, *J. Geophys. Res., 88*, 689–699, 1983.

Metcalf, W. G., On the Formation of Bottom Water in the Norwegian Basin, *Trans. Amer. Geophys. Union, 36*, 596–600, 1955.

Millero, F. J., C. Chen, A. Bradshaw, and K. Schleicher, A new high-pressure equation of state for seawater, *Deep Sea Res., 27*, 255–264, 1980.

Munk, W. and C. Wunsch, Ocean acoustic tomography: a scheme for large scale monitoring, *Deep Sea Res., 26A*, 123–161, 1979.

Munk, W. and C. Wunsch, Ocean Acoustic Tomography: Rays and Modes, *Rev. Geophys. and Space Phys., 21*, 777–793, 1983.

Munk, W. and C. Wunsch, Biases and Caustics in long-range acoustic tomography, *Deep Sea Res., 32*, 1317–1346, 1985.

Munk, W. and C. Wunsch, Bias in Acoustic Travel-Time Through an Ocean with Adiabatic Range-Dependence, *Geophys. and Astrophys. Fluid. Dyn., 39*, 1–24, 1987.

Mysak, L. A., D. K. Manak, and R. F. Marsden, Sea-Ice Anomalies observed in the Greenland and Labrador Seas during 1901-1984 and their relation to an interdecadal Arctic climate cycle, *Clim. Dyn, (5)*, 111–133, 1990.

Nagurny, A. P. and A. V. Popov, Intensive upwelling of Deep and Bottom Waters and Their Formation at the Surface in the Region of the Greenland Hollow, *Meteorologia i Gidrologia, (7)*, 70–75, 1985.

Pedlosky, J., The Instability of Continuous Heton Clouds, *J. Atmos. Sci., 42*, 1477–1486, 1985.

Pedlosky, J., *Geophysical Fluid Dynamics* (2nd ed.). Springer-Verlag, 1987.

Peterson, W. H. and C. G. H. Rooth, Formation and exchange of deep water in the Greenland and Norwegian Seas, *Deep Sea Res., 23*, 273–283, 1976.

Price, J. F., On the scaling of stress-driven entrainment experiments, *J. Fluid. Mech., 90*, 509–529, 1979.

Price, J. F., R. A. Weller, and R. Pinkel, Diurnal Cycling: Observations and Models of the Upper Ocean Response to Diurnal Heating, Cooling, and Wind Mixing, *J. Geophys. Res., 91*, 8411–8427, 1986.

Rhein, M., Ventilation Rates of the Greenland and Norwegian Seas derived from distributions of the chlorofluoromethanes F11 and F12, *Deep Sea Res., 38*, 485–503, 1991.

Roach, A. T., K. Aagaard, and F. Carsey, Coupled Ice-Ocean Variability in the Greenland Sea, *Atmosphere-Ocean, 31*, 319–337, 1993.

Rudels, B., Haline Convection in the Greenland Sea, *Deep Sea Res., 37*, 1491–1511, 1990.

Sanger, C. W., Environmental Factors affecting 17th-19th century whaling in the Greenland Sea, *Polar Record, 27*, 77–86, 1991.

Schlosser, P., G. Bonisch, M. Rhein, and R. Bayer, Reduction of Deepwater Formation in the Greenland Sea During the 1980s: Evidence from Tracer Data, *Science, 251*, 1054–1056, 1991.

Schott, F. and K. D. Leaman, Observations with Moored Acoustic Doppler Current Profilers in the Convection Regime in the Golfe du Lion, *J. Phys. Oceanogr., 21*, 558–574, 1991.

Schott, F., M. Visbeck, and J. Fischer, Observations of Vertical Currents and Convection in the Central Greenland Sea During the Winter of 1988/89, *J. Geophys. Res., 98*, 14,401–14,421, 1993.

Schott, F., M. Visbeck, and U. Send, Open-Ocean Deep Convection, Mediterranean and Greenland Seas, pp. (submitted), 1993.

Schwerdtfeger, P., The Thermal Properties of Sea Ice, *J. Glaciology, 4*, 789–807, 1963.

SIZEX Group, SIZEX 89 Experiment Report, Technical Report The Nansen Remote Sensing Center Technical Report 23, The Nansen Remote Sensing Center, Bergen, Norway, 1989.

Smith, S. D. and F. W. Dobson, The Heat budget at Ocean Weather Station *Bravo*, *Atmosphere-Ocean, 22*, 1–22, 1984.

Spindel, R. C., Signal Processing in Ocean Tomography, In *Adaptive Methods in Underwater Acoustics*, edited by H. G. Urban, pp. 687–710. D. Reidel, Boston, 1985.

Steffen, K., J. Key, D. J. Cavalieri, J. C. Comiso, P. Gloersen, K. S. Germain, and I. Rubenstein, The Estimation of Geophysical Parameters using Passive Microwave Algorithms, In *Microwave Remote Sensing of Sea Ice*, edited by F. D. Carsey, Volume 68 of *Geophysical Monograph*, Chapter 10, pp. 201–231. American Geophysical Union, Washington, 1992.

Steffen, K. and A. Schweiger, NASA Team Algorithm for Sea Ice Concentration Retrieval from Defense Meterological Satellite Program Special Sensor Microwave Imager: Comparison with Landsat Satellite Imagery, *J. Geophys. Res., 96*, 21,971–21,987, 1991.

Sutton, P. J., W. Morawitz, B. D. Cornuelle, P. F. Worcester, and G. Masters, The Incorporation of Acoustic Normal Mode data into Tomographic Inversions in the Greenland Sea, *J. Geophys. Res.*, (accepted), 1993.

Sutton, P. J., P. F. Worcester, G. Masters, B. D. Cornuelle, and J. F. Lynch, Ocean Mixed layers and acoustic pulse propagation in the Greenland Sea, *J. Acoust. Soc. Am., 94*, 1517–1526, 1993.

Taylor, P. K. and E. C. Kent, Evaluation of Fluxes from Forecast Models using Voluntary Observing Ship Data, 1992. in Report on Joint meeting of the JSC/CCCO Working Group on Air Sea Fluxes and The WOCE Surface Layer Panel, ECMWF, Reading, 21-25 October 1991, WMO, Geneva.

Tolstoy, A., Linearization of the matched field processing approach to acoustic tomography, *J. Acoust. Soc. Am., 91*, 781–787, 1992.

Tolstoy, A. and O. Diachok, Acoustic Tomography via matched field processing, *J. Acoust. Soc. Am., 89*, 1119–1127, 1991.

Vinje, T. E., Sea Ice Conditions in the European Sector of the Marginal Seas of the Arctic, 1966–1975, *Norsk Polarinstitutt Årbok*, 163–174, 1977.

Wadhams, P., The Ice Cover, In *The Nordic Seas*, edited by B. G. Hurdle, Chapter 2, pp. 21–84. Springer-Verlag, New York, 1986.

Walsh, J. E. and C. M. Johnson, An Analysis of Arctic Sea Ice Fluctuations, *J. Phys. Oceanogr., 9*, 580–591, 1979.

Worcester, P., O. Peckham, K. Hardy, and F. Dormer, AVATAR: Second generation transceiver electronics for ocean acoustic tomography, In *Proceedings of Oceans 85*, 1985.

Worcester, P. F., J. F. Lynch, W. M. Morawitz, R. Pawlowicz, P. J. Sutton, B. D. Cornuelle, O. M. Johannessen, W. H. Munk, W. B. Owens, R. Shuchman, and R. C.

Spindel, Ocean acoustic tomography in the Greenland Sea, *Geophys. Res. Lett.*, *20*, 2211–2214, 1993.